



Delft University of Technology

Solar Drone

Bachelor Thesis Electrical Engineering
Supervised by Dr. P.J. van Duijsen

**D.C. de Best, M.S. Mollaie Daryani, J. Gelderblom,
V.C. Nguyen, J. van Roessel & D.D.D.T.D. Sitaldin**
[4462955][4410874][4441478][4452690][4387481][4429648]



Abstract

The main goal of this Electrical Engineering Bachelor project is to build a solar-power system for a quad-copter that will extend its battery life or rather its *flight time*. The complete system is comprised of a PV system (PV), a micro-controller (MC) and a DC/DC converter (DC) which was mounted onto the drone. On each subsystem, a separate thesis was written and this paper serves as a general yet complete overview of the design process, simulations and test results of a fully functioning solar drone with the theses attached as appendices for reference.

The original (optimistic) aim of an extension of at least 25% of the battery lifetime was set by our supervisors. For the PV part SunPower C60 IBC cells were used (no specific selection was done) together with a (borrowed) custom-built drone (not built by this team, it was borrowed from another research group) as a starting point. After analysing the limitations of the drone and the cells, multiple configurations were designed and a mathematical model that determines power usage, energy costs per solar cell and the optimum amount of cells was developed.

A SEPIC converter will extract solar energy from a PV-module in order to charge the battery of the drone. The converter will be controlled by the micro-controller subgroup using MPPT (Maximum Power Point Tracker) algorithm and this will be done by supplying a PWM signal to the converter.

Since the drone was not specifically designed for the project (thus not optimised when it comes to lift capacity and room for cell placement), the efficiency of the solar cells was not sufficient to extend the flight time by 25% (**15.1% in summer, 5.6% in winter**). Since these bottlenecks can easily be eliminated by replacing the drone and the cells, these results serve as a proof of concept and are an excellent starting point for future research.

Acknowledgements

We would like to express our sincerest gratitude to Dr. Peter van Duijsen, our supervisor, for his guidance throughout the project and also to Dr. Olindo Isabella. You both have been a big help, we truly appreciated the time you spent on our work and your eagerness to help us out. We are also grateful to the staff and PhD students of the Tellegen Hall, DC Systems group and the PV Lab. A special thanks to Prof. Koen Langedoen and PhD student Sujay Narayana of the Embedded Systems group who were so kind to lend us one of their drones. Your support cannot be forgotten, without it we would not have had a suitable drone to mount our system on.

Lastly, we would like to thank our families, who have always supported us in our endeavours and have helped us become the scientists we are today.

*David de Best, Salar Mollaie Daryani, Joey Gelderblom,
Van Cong Nguyen, Joris van Roessel & Dewwret Sitaldin
Delft, 19th of June 2019*

Contents

Abstract	i
Acknowledgements	iii
Contents	v
1 Introduction	1
1.1 Problem Definition	1
1.2 State-of-the-Art Analysis	2
1.3 Thesis Outline	2
2 System Overview	5
2.1 Photovoltaic System & Power Management	5
2.2 Microcontroller	6
2.3 DC/DC converter	6
2.4 Full System	6
3 Test Results	9
3.1 PV System & Power Management	9
3.2 Microcontroller	10
3.3 DC/DC Converter	11
3.4 Overall System: Can it fly?	12
4 Conclusion & Discussion	13
Appendices	15
A Thesis I: PV System & Power Management David de Best & Dewwret Sitaldin	17
B Thesis II: Microcontroller Salar Mollaie Daryani & Van Cong Nguyen	73
C Thesis III: DC/DC Converter Joey Gelderblom & Joris van Roessel	141
Bibliography	201

CHAPTER 1

Introduction

In the past decade drones have become increasingly popular as they are agile, stable and relatively small in size. Because of their versatility, they have been deployed for all sorts of purposes, including warfare, video recording and, to a lesser extent, even transport.

The increasing demand and deployment of these devices raise not only concerns over safety and privacy but also energy technologies, since short flight time or short battery life has from the start been a major shortcoming. For military applications, the solution has always been easy as military drones are mainly powered by fossil fuels. In the consumer market, longer battery life is desirable but not of utmost importance as these drones are mostly used for leisure only. The industrial sector is the one that will benefit the most from an alternative, low-cost and superior fuel technology since there are plenty of commercial applications for which longer flight time directly impacts the end result (e.g. transport).

The main problem with an alternative technology is the higher cost that comes with it. An innovative system that uses a sustainable energy source that is economical and easy to implement will solve many of the issues at hand and truly is a big step in making the world a greener place.

1.1 Problem Definition

The main goal of this Electrical Engineering Bachelor project is to build a solar-power system for a quad-copter that will extend its battery life or rather its *flight time*. The system is comprised of a PV system, a micro-controller and a DC/DC converter which will be mounted onto the drone. This had to be done by a group of 6 students who were split into 3 subgroups of 2 students and each team tackled 1 subsystem, see [Chapter 2](#) for a system overview. All 3 subgroups have written a thesis on their respective subsystem which have been included as a reference in [Appendix A](#), [Appendix B](#) and [Appendix C](#).

Cooled Package Delivery

The popularity of drones has skyrocketed, but not longer than 15 years ago no one had ever heard of drones before, let alone its potential applications like quick transport. 20 years ago, most packages were delivered by bike, scooter, vans and trucks.

Even now this has not changed much, because most of our mail is still delivered by bike or van. When time is of the essence, these methods of transport are far from ideal, especially when one is dealing with poor infrastructure.

In many situations, this is exactly the case. Take for instance Africa, where infrastructure is almost non-existing, resources are scarce and hospitals are often unreachable for the locals. In case of a health related emergency, those people will never reach the hospital on time, if at all.



Figure 1.1: Medical Delivery Drone

By deploying a solar-powered drone delivery network, medicine, vaccines and other types of aid can be delivered to even the most remote and isolated villages. Many of the medicines will not withstand the heat and get spoilt so installing cooled container/refrigerator onto the drone will keep the goods from spoiling.

To power the fridge and extend the battery life of the drone, (a more advanced version of) the PV system can be used.

1.2 State-of-the-Art Analysis

Drone-based projects are booming due to the aforementioned popularity increase, but only a few groups however have combined the concept of solar energy and drones into one project. Until now one research group, students from the National University of Singapore, has managed to develop a fully solar powered quad-copter. Very impressive, a great proof-of-concept and a true inspiration for our project (*Asia's first fully solar-powered quadcopter n.d.*). Our research started with determining the best possible solar cell technology for this project, but as time progressed it was clear that the selection of the best possible cell technology will not contribute to this project as cells can easily be swapped for better ones. Also, superior cell technologies like multi-junction cells are very costly and nowhere near market-ready yet. Instead one should focus on the optimisation processes of the system itself.

In all of research that the team has encountered so far, most of the groups spent a considerable amount of time on the specifics of the cell rather than on the system as a whole. In our case, with non-ideal components (a non-ideal drone, cells that are lacking in efficiency and unfavourable irradiance), optimisation is crucial. In all three theses, optimisation of the main components of this drone (like optimum amount of cells for this specific drone, or optimum drone size for this specific setup) and scalability has been covered such that this research can be used for generations to come.

1.3 Thesis Outline

The rest of the text is organised as follows:

Chapter 2 This chapter comprises the system overview of the solar drone and provides a comprehensible description of each of the three subsystems.

Chapter 3 This 3 focuses on the test set-up and results of the final product. Test results and simulations of the subsystems and thoroughly discussed in their respective theses (see appendices).

Chapter 4 The electrical interconnection of the solar cells is thoroughly discussed in chapter 5. An analysis of the major schemes (Series-Parallel, Bridge Link, and Total-Cross-Tied) will be done and the various trade-off will be discussed. Based on this analysis a interconnection scheme will be picked.

Appendix A Full thesis on the photovoltaic and power management subsystem.

Appendix B Full thesis on the microcontroller subsystem.

Appendix C Full thesis on the DC/DC converter subsystem.

CHAPTER 2

System Overview

Since the goal of the goal of this project is to extend the flight time of a drone by designing the best possible solar module configuration, the drone and the solar cells itself will not designed and/or developed (however, they are carefully chosen). That is why the drones and solar cells were used as a starting point upon which a realistic design of the solar cell *configuration*, the micro-controller and the DC/DC converter was based.

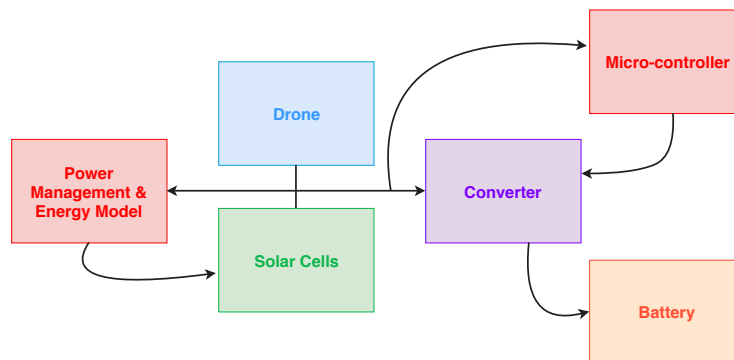


Figure 2.1: Full (simplified) system overview

Figure 2.1 depicts the connections between the subsystems. One starts with the 2 basic components, the drone and the solar cells. Once there's a proper understanding of the solar cell, the drone dimensions and the limitations, power consumption and optimisation can be modelled (power management). The micro-controller determines the duty cycle for the DC/DC converter, thus they are closely connected. A very in-depth overview that touches on input and output signals is depicted in figure 5 (thesis II), for now a simplified is presented in Figure 2.1.

The Sunpower Maxeon C60 (IBC) solar cells were used ($\eta \approx 22\%$), the component specifications of the full system are given in section 1.4 of thesis I. See section for a report on all limitations and trade-offs of the overall system.

2.1 Photovoltaic System & Power Management

Once there's a proper understanding of solar cell, the drone dimensions and their limitations, the cell placement can be discussed and multiple configurations can be designed.

Since the PV group is also responsible for the overall power management (see Chapter 3), the drone specifications especially played a crucial role in the general progress of the project and determination of the boundary conditions/limitations.

2. System Overview

After analysing the limitations of the drone and the cells, multiple configurations were designed (see section 3.2 of thesis I) and a mathematical model that determines power usage, energy costs per solar cell and the optimum amount of cells was developed. This model was based on the aerodynamics of the drone and can be found in section 3.3 (thesis I). After running the model and validating the results, multiple interconnection schemes were considered (SP, BL, TCT) and the system was mounted.

See [Appendix A](#) for a full report on power management, the energy model and the trade-offs that were made.

2.2 Microcontroller

The microcontroller forces the solar module to generate electricity as efficiently as possible. It senses the voltage and current of the solar module and provides a proper PWM signal for the converter (see [Figure 2.2](#)). The duty cycle of this PWM signal can be adjusted in order to ensure extract the most energy from the solar module.

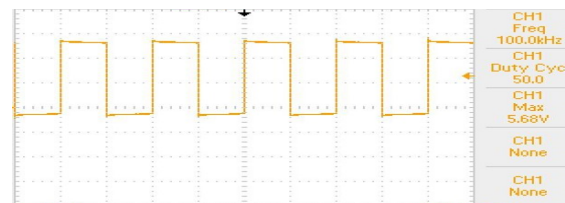


Figure 2.2: The PWM signal generated by the microcontroller

The provided duty cycle is on the base of different algorithms which have been implemented on the microcontroller. One of them is the Improved Differential Evolution(IDE). The microcontroller can find the maximum power point (MPP) of the solar module in less than 2 seconds for different environments and under different circumstances. The average efficiency of the microcontroller together with its algorithms and sensors is **91%**. The microcontroller is able to be up to date with the new and more efficient algorithms. See [Appendix B](#) for a full report.

2.3 DC/DC converter

In order to extract energy from a solar module a DC/DC converter is needed. This converter extracts the energy and converts it so it can charge the lithium-ion battery of the drone.

The topology used for this project is the SEPIC (Single-Ended Primary-Inductor Converter). A MOSFET will be used at the place of the Switch (S). At the gate of this MOSFET the PWM signal coming from the microcontroller will be supplied. The duty cycle of this signal controls at which point on the PV-curve the converter will be operating. The main priority of designing this converter is that it should have a low mass in order to reduce energy consumption of the drone. The second objective is achieving a high power efficiency operating at MPP. This resulted in the SEPIC shown in [Figure 2.3](#) with a overall power efficiency of **83%** operating at MPP. See [Appendix C](#) for a full report.

2.4 Full System

After the subsystems were designed and tested rigorously they were integrated and mounted onto the drone. The solar cells were laminated to and then cut into modules of 3 cells and the power electronics were mounted at the bottom of the drone. [Figure 2.4](#) depicts the integration of both the micro-controller and the DC/DC converter while [Figure 2.5](#) shows the fully custom-built system, ready for take-off.

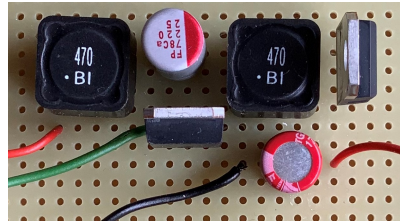


Figure 2.3: SEPIC converter

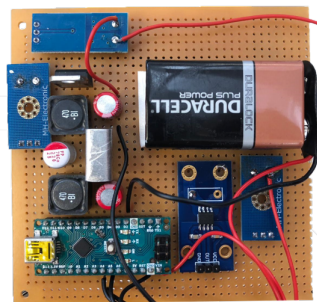


Figure 2.4: All the electronics of the solar system combined on one board.



Figure 2.5: Full system

CHAPTER 3

Test Results

3.1 PV System & Power Management

Energy Costs & Cell Configuration

It seems logical to add as many as solar cells as possible in order to gain more energy. However, in the case of the solar drone, adding solar cells also means adding extra weight which has to be lift (and therefore requires more power). Since the relation between the addition of solar cells and the extra required power to lift its weight is non-linear, a linear approximation has been made. Per kilogram, 129.5 W is required to lift the extra weight. Per solar cell, 0.9756 W is required. From that, the optimal amount of solar cells was calculated for different irradiance levels. With this in mind a top-mounted configuration was chosen.

Optimum number of solar cells

For an irradiance of 300 W/m², placing 28 solar cells gives the highest possible output power (*for this specific drone*). Furthermore, the most suitable electrical interconnection configuration had to be chosen. With thorough research and taking the limitations of the drone into account, a series connection has been chosen above a total-cross-tied and bridge-linked configuration. Since no partial shading is assumed in mid-air, no bypass diodes and/or micro-inverters should be added, since they add weight and complexity. More on the optimisation, the model and maximum weight can be found in section 3.3 of thesis I (see [Appendix A](#)).

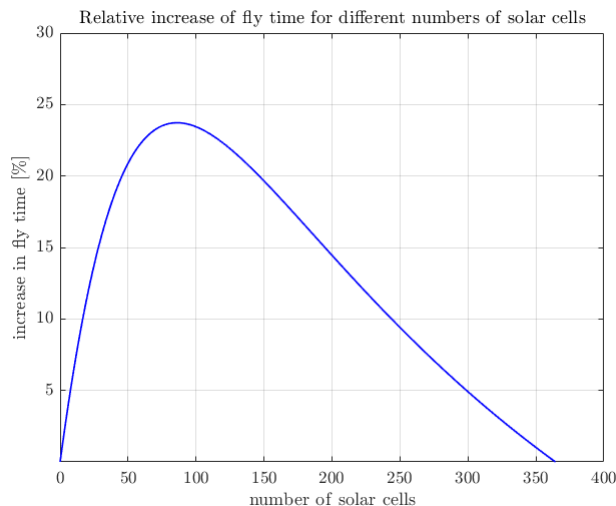


Figure 3.1: The maximum output power achievable for different numbers of solar cells in case of an irradiance of 500 W/m²

3. Test Results

3.2 Microcontroller

The algorithms used for this subsystem are validated with two setups: The Solar Trainer module (a solar cell simulator) and the actual solar cells that have been mounted onto the drone (12 in series). The average efficiency will be taken from 10 samples.

Solar Trainer

To validate the algorithm the Solar Trainer IV and PV curve have to be known, this can be done by connecting a variable load to the Solar Trainer and measuring the voltage and current with the multimeter. The Solar Trainer has three different irradiances level by changing the short circuit current (0.4, 0.8 and 1.2 [A]). In Figure 3.2 the IV and PV curves for the three different irradiances level are plotted.

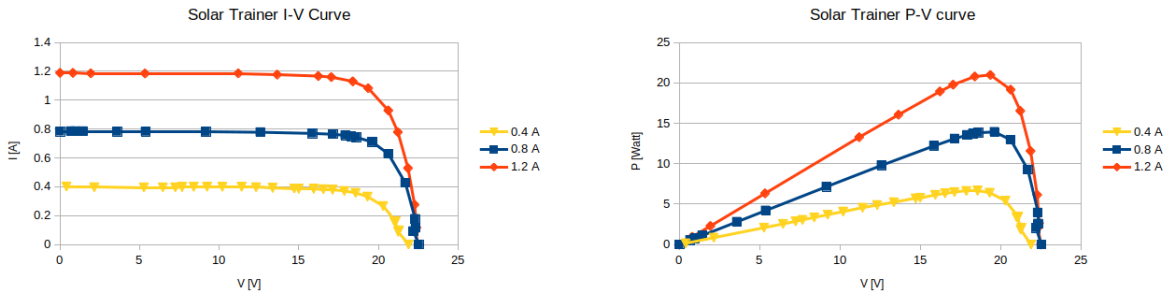


Figure 3.2: The I-V and P-V Curve of the Solar Trainer

The implemented algorithms together with the converter have been connected to the setups and the microcontroller forces the solar simulators to generate electricity in their maximum power point. From the measurements it was clear that the IC algorithm has a lower efficiency than P&O but it does not oscillate as much as the P&O does.

12 Cell Set-up

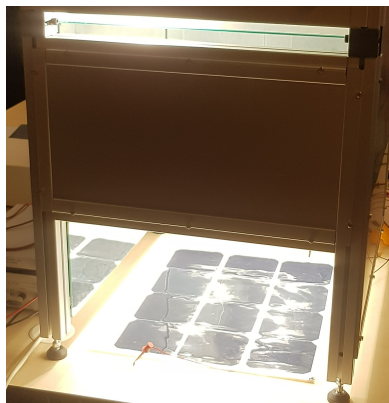


Figure 3.3: 12 cell set-up in the PV lab

For this set-up both the P&O and the IC algorithm performed very well. The drawback of the P&O method is that the power oscillates around the MPP while IC locks on a power. The tricky part of the IC method is to find the right error value. If the error value is too high it will lock on the wrong power and if the error value is too low it keeps searching for the MPP. And for every

PV system the error value is different so it has to be modified.

The complete test results with the SEPIC converter of the $P\&O$ and IC algorithm can be found in Chapter 6 of thesis II (see [Appendix B](#)).

3.3 DC/DC Converter

Multiple designs and configurations were made and tested. With the third SEPIC design shown in [Figure 2.3](#) the measurements were executed. An input capacitor was added to the design in order to stabilise the power extracted from the PV-array and increase the overall extracted power, see chapter 6 of thesis III ([Appendix C](#) of the general report). For the measurements the SEPIC was connected to a 12-series PV-array and a pulse generator.

Measurements were done for three different solar irradiances that are exposed to the PV-array. This was done using a solar box available in the Solar Lab in the Tellegen Hall of TU Delft. In appendix H of thesis III, the solar box with PV-array is shown and the solar irradiance meter that was used. For both a resistive load of $20\ \Omega$ and a lithium-ion battery as load measurements are done. Results are shown in H.1 and H.2 respectively.

The measurements done with the resistive load, did give an indication of what the maximum output power could be for different solar irradiances. Because, as was already stated in subsection 6.2.2 (thesis III), the maximum charge current of the battery 2A. Greater current could damage the battery severely.

From figure 35 (appendix H.1 thesis III) it can be concluded that the power extracted from the PV-array at a solar irradiance of $535\ W/m^2$ is at MPP 7.5W. Therefore a lithium-ion battery with a rated voltage of 7.4V can never receive a charge current greater than 2A from the PV-array at this solar irradiance.

The most interesting measurements is the one with the lithium-ion battery as load. In appendix H.2 of thesis II, the power efficiency of the converter is shown for different solar irradiances. From the simulation power efficiency plot in appendix C.5 (of thesis III) it was concluded that for greater solar irradiances, the power efficiency of SEPIC decreased. This is also reflected in the practical measurements.

In appendix H.1 the MPP per solar irradiance is indicated with a '+'. These show that for a greater solar irradiance the power efficiency of the SEPIC decreased operating at MPP.

Furthermore it can be concluded that the average power efficiency of the SEPIC operating at MPP for solar irradiance between 280 and $535\ W/m^2$ is 82.9%. The MPP power efficiency values of table 25, table 26 and table 27 are shown in [Table 3.1](#). These values are quite similar to those of the simulations in table 6 (see section 6.3.2 of thesis III).

From the same measurements can concluded that the maximum charge rating of the battery is not exceeded. The maximum current measured flowing into the battery is 0.846A for a solar irradiance of $535\ W/m^2$ and the maximum charge rating of the battery is 2A. Thus even for double the solar irradiance the maximum charge rating of the battery will not be exceeded because the efficiency will also decrease for increasing solar irradiance.

Power efficiency [%]	280 [W/m^2]	430 [W/m^2]	535 [W/m^2]	Average [%]
12-series PV-cell configuration	85.641	81.831	81.202	82.9

Table 3.1: Power efficiency per solar irradiance of the practical SEPIC using a lithium-ion battery as load.

3.4 Overall System: Can it fly?

After the integration of all subsystems, multiple flight tests were done and it is fair to say that the drone is fully functional. The system was able to charge the battery while still maintaining a stable flight.

Due to the absence of the technical assistant who was responsible for the drone, no proper calibration could have been done so there were some issues, therefore the drone was not allowed to fly on high altitudes and had to be tested within the lab itself.

With a more light-weight drone, superior solar cells and better control calibration, the quadcopter could have flown further and much higher. All in all, very desirable results were obtained and a new proof of concept has been established,

CHAPTER 4

Conclusion & Discussion

The full system is able to charge the battery while maintaining a stable flight and small form factor.

With the mathematical model, it was shown that any extension in the flight-time of the drone depends on the general specifications of the solar cells (the weights and efficiency). More solar cells will not per se result in longer flight-time. With this trade-off in mind, the situation was modelled and an optimum was found.

The generated electrical power by the solar cells should charge the battery of the drone as efficiently as possible. To achieve this target, the charge controller consisting the micro-controller and the DC/DC converter have been designed and implemented. The micro-controller searches and find the Maximum Power Point (MPP) of the mounted solar module on the drone, and provides a PWM signal to run the MOSFET of the converter. The micro-controller can successfully find the MPP of the solar cells with an average efficiency of 91%.

The SEPIC DC/DC converter charges the battery of the drone with an average efficiency of 83%. All the mentioned sub-components can charge the battery of the drone up to 2A. The power consumption of the final product is only 0.1W and it weighs 130g in an area of 10cm x 10cm (see [Figure 2.4](#)).

The achieved results can be improved by improving the following:

- Efficiency and weight of the solar cells.
- Lift capacity of the drone.
- ADC resolution for the micro-controller to measure the voltage and current of the solar cells more accurate.
- Efficiency of the MPPT algorithm on the micro-controller (meaning that a more complex and thus more efficient algorithm should be used).
- Efficiency of the design for the DC/DC converter.

Although the results do not show a considerable change in the flight-time of the drone, it can charge the battery of the drone and consequently increases the lifetime of the battery. The drone design was the main bottleneck that impacted the flight-time. Had a custom-built drone, that was specifically designed for this project, been used the results could be much better since there would be an increased amount of lift power, room for the solar cells and an overall higher efficiency. However, the design of a drone is out of scope of this Electrical Engineering Bachelor Project.

Appendices

APPENDIX A

Thesis I: PV System & Power Management

David de Best & Dewwret Sitaldin



Delft University of Technology

Solar Drone

Photovoltaic System & Power Management

Bachelor Thesis Electrical Engineering

Supervised by Dr. P.J. van Duijsen

D.C. de Best & D.D.D.T.D. Sitaldin

[4462955][4429648]



Abstract

In this paper the design and implementation of a photovoltaic (PV) system of a solar drone is thoroughly discussed. The main goal of this Electrical Engineering Bachelor project is to build a solar-power system for a quad-copter that will extend its battery life time or rather its *flight time*. The complete system is comprised of a PV system, a micro-controller (MC) and a power converter (PC) which will be mounted onto the drone, but this paper focuses solely the PV part.

The original aim was an extension of at least 25% of the battery lifetime. SunPower C60 IBC cells were used (no specific selection was done) together with a (borrowed) custom built drone (not built by us and intended for another project) as a starting point. After analysing the limitations of the drone and the cells, multiple configurations were designed (see Section 3.2) and an energy model that determines power usage, energy costs per solar cell and the optimum amount of cells was developed. This model was based on the aerodynamics of the drone and can be found in Section 3.3. After running the model and validating the results, multiple interconnection schemes were considered (SP, BL, TCT) and the system was mounted. Unfortunately the gain was lower than desired, with a 5.6% increase in winter and 15.1% increase in summer, because of lacking efficiency of the panels and non-ideal angles of incidence (see Section 3.3). Despite the fact that the target efficiency was not achieved, the results are still of great value as all of the developed models are universal and do tell when and for which hardware specifications/irradiances it will yield the desired results.

Acknowledgements

We would like to express our sincerest gratitude to Dr. Peter van Duijsen, our supervisor, for his guidance throughout the project and also to Dr. Olindo Isabella. You both have been a big help, we truly appreciated the time you spent on our work and your eagerness to help us out. A special thanks to Prof. Koen Langedoen and Mr. Sujay Narayana of the Embedded Systems group who were so kind to lend us one of their drones. Your support cannot be forgotten, without it we would not have had a suitable drone to mount our system on.

Also a big thanks to thank our colleagues and friends Salar Mollaie Daryani, Van Cong Nguyen, Joey Gelderblom and Joris van Roessel. It has been a pleasure working with you, you were the best.

Finally, we would like to thank our families for their love and support, we are where we are today thanks to you.

*David de Best & Dewwret Sitaldin
Delft, 19th of June 2019*

Contents

Abstract	i
Acknowledgements	iii
Contents	v
1 Introduction	1
1.1 Problem Definition	1
1.2 State-of-the-Art Analysis	2
1.3 PV System Overview	3
1.4 Component Specifications	3
1.5 Thesis Outline	4
2 Programme of Requirements	5
2.1 Market Assumptions	5
2.2 Goals & Limitations	5
2.3 Mandatory Requirements	6
2.4 Trade-off Requirements	6
3 Power Management	7
3.1 Limitations & Trade-offs	7
3.2 Configuration Designs	9
3.3 Modelling Energy Consumption	10
3.4 Irradiance	14
3.5 Configuration Selection	16
4 Electrical Configuration	19
4.1 Mismatch Losses	19
4.2 Interconnection Schemes	20
4.3 Different configuration for different shading situations	20
4.4 Bypass diodes	21
4.5 Conclusion on electrical configuration	23
5 Solar Drone Performance	25
6 Conclusion & Discussion	27
6.1 Future Research	28
Appendices	29
A Studies, Figures and Derivations	31
A.1 Hovering Power	31

Contents

A.2	Optimal number of solar cells	32
A.3	Irradiance: Optimal Tilt Angle	34
A.4	Magic Square	35
A.5	Bypass diode configuration	36
A.6	Simulation of configurations for different shading situations	39
B	Computer Code	41
	Bibliography	45

CHAPTER 1

Introduction

In the past decade drones have become increasingly popular as they are agile, stable and relatively small in size. Because of their versatility, they have been deployed for all sorts of purposes, including warfare, video recording and, to a lesser extent, even transport.

The increasing demand and deployment of these devices raise not only concerns over safety and privacy but also energy technologies, since short flight time or short battery life has from the start been a major shortcoming. For military applications, the solution has always been easy as military drones are mainly powered by fossil fuels. In the consumer market, longer battery life is desirable but not of utmost importance as these drones are mostly used for leisure only. The industrial sector is the one that will benefit the most from an alternative, low-cost and superior fuel technology since there are plenty of commercial applications for which longer flight time directly impacts the end result (e.g. transport).

The main problem with an alternative technology is the higher cost that comes with it. An innovative system that uses a sustainable energy source that is economical and easy to implement will solve many of the issues at hand and is a truly big step in making the world greener.

1.1 Problem Definition

The main goal of this Electrical Engineering Bachelor project is to build a solar-power system for a quad-copter that will extend its battery life or rather its *flight time*. The system is comprised of a PV system, a micro-controller (MC) and a power converter (PC) and will be mounted onto the drone. This had to be done by a group of 6 students who were split into 3 subgroups of 2 students and each team tackled 1 subsystem..

Cooled Package Delivery

The popularity of drones has skyrocketed, but not longer than 15 years ago no one had ever heard of drones before, let alone its potential applications like quick transport. 20 years ago, most packages were delivered by bike, scooter, vans and trucks.

Even now this has not changed much, because most of our mail is still delivered by bike or van. When time is of the essence, these methods of transport are far from ideal, especially when one is dealing with poor infrastructure.

In many situations, this is exactly the case. Take for instance Africa, where infrastructure is almost non-existing, resources are scarce and hospitals are often unreachable for the locals. In case of a health related emergency, those people will never reach the hospital on time, if at all.

By deploying a solar-powered drone delivery network, medicine, vaccines and other types of aid can be delivered to even the most remote and isolated villages. Many of the medicines will not withstand the heat and get spoilt so installing cooled container/refrigerator onto the drone will keep the goods from spoiling.

1. Introduction

To power the fridge and extend the battery life of the drone, (a more advanced version of) the PV system can be used.

Scoping & Bounding Analysis

There are many complications with this unprecedented idea/product. Since it has never been done before there are no clear regulations on the matter yet if there are at all. It is fair to say that there is a great need for this project since (re)building African(like) countries will take notably longer and cost substantially more. This project is definitely riskier but could potentially save many lives in the mean time.

One of the major constraints of this application are safety and regulations.

- Once it arrives at the village, who takes care of business?
- Who sends it back, does it fly back by itself?
- Once a drone departs, what happens when it crashes on its way?

This will be thoroughly discussed during the Business Plan presentation.

1.2 State-of-the-Art Analysis

Drone-based projects are booming due to the aforementioned popularity increase, but only a few groups however have combined the concept of solar energy and drones into one project. Until now one research group, students from the National University of Singapore, has managed to develop a fully solar powered quad-copter. Very impressive, a great proof-of-concept and a true inspiration for our project (*Asia's first fully solar-powered quadcopter* n.d.). Our research started with determining the best possible solar cell technology for this project, but as time progressed it was clear that the selection of the best possible cell technology will not contribute to this project as cells can easily be swapped for better ones. Also, superior cell technologies like multi-junction cells are very costly and nowhere near market-ready yet. Instead one should focus on the optimisation processes of the system itself.

In all of research that the team has encountered so far, most of the groups spent a considerable amount of time on the specifics of the cell rather than on the system as a whole. In our case, with nonideal components (a nonideal drone, cells that are lacking in efficiency and unfavourable irradiance), optimisation is crucial. For this to happen a clear and solid model is necessary that determines optimal situations of the system (like optimum amount of cells for this specific drone, optimum drone size for this specific setup). Scalability such that this very research can be used for generations to come.

1.3 PV System Overview

As explained in Section 1.1, the PV system is one of the 3 main parts of the solar drone, with the others being the micro-controller and the power converter. Since the PV group is also responsible for the overall power management (see Chapter 3), the drone specifications especially played a crucial role in the general progress of the project and determination of the boundary conditions/limitations.

Figure 1.1 depicts the connections between the subsystems. One starts with the 2 basic components, the drone and the solar cells. Once there's a proper understanding of the solar cell, the drone dimensions and the limitations, the cell placement can be discussed and multiple configurations can be designed (see Section 3.2).

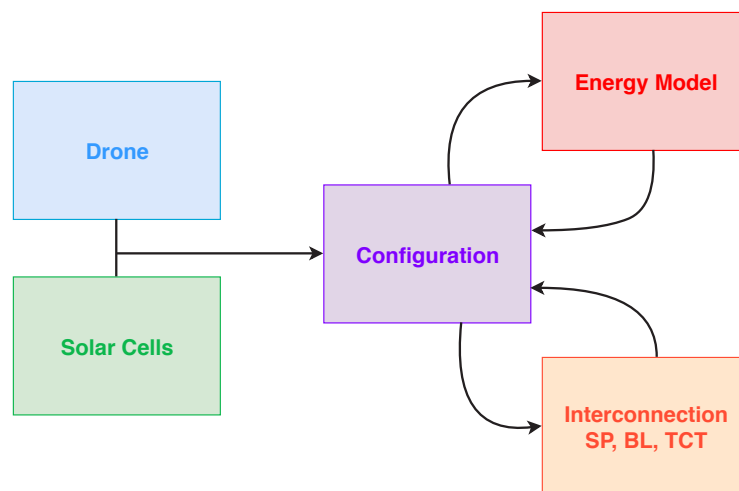


Figure 1.1: Connection between all components

An energy model that determines power usage, energy costs per solar cell and an optimal amount of cells require the specifications of the drone, cells and configuration as input. This model was based on the aerodynamics of the drone and can be found in Section 3.3. After running the model and validating the results, the interconnection schemes will be considered (Chapter 6) to make sure there is no 'unwanted' mismatch and therefore to pick the ideal configuration.

1.4 Component Specifications

Notes on solar cell selection

The cell that was provided to this PV group is the SunPower C60 Interdigitated Back Contact (IBC) cell (Corporation, 2010). At the start of the project thorough research was started on various cell technologies, multi-junction cells etc. but this was also quickly halted after realising that it would not benefit this specific project at all. In order to achieve a long extension of the battery life, one's time and resources should be spent on optimisation processes (see Section 3.3) instead of cell technology, since cells can easily be swapped for newer and superior ones.

Notes on lift capacity

Since the drone is only rated for a lift capacity of 500 g, a very limited amount of $500 - (75 + 75) = 305$ g (see Table 1.1) can be reserved for the *complete* PV system (also including wires and construction).



Figure 1.2: Solar Cell and Drone used in the project

Table 1.1: Drone and battery specifics

Parameter	Value
Solar cell efficiency	$\eta \approx 22\%$
Solar cell dimensions	0.125x 0.125 [m]
Solar cell weight	7.5 [g]
Drone weight	680 [g]
Drone lift capacity	500 [g]
Drone weight	680 [g]
Propeller radius	0.13 [m]
Li-Po battery weight	249.9 [g]
Li-Po battery capacity	4000 [mAh]
Micro-controller system	~ 75 [g]
Power Converter system	~ 75 [g]

1.5 Thesis Outline

The rest of the text is organised as follows:

Chapter 2 This chapter comprises the description of the features of the product to be developed, namely: its key performance indicators (KPI) and the conditions applying to its development, production/implementation, exploitation and discarding.

Chapter 3 This chapter focuses on the expected power usage of the drone and the possible gain of the system. Based on the aerodynamics of the drone, energy consumption will be modelled and irradiance and angles of incidence will be taken into account to determine the placement of the solar cells on the system (top-mounted, side-mounted, top-side mounted). At the end of this chapter it will be clear whether the PV system is even worth adding and if it is, its significance will be discussed.

Chapter 4 The electrical interconnection of the solar cells is thoroughly discussed in chapter 5. An analysis of the major schemes (Series-Parallel, Bridge Link, and Total-Cross-Tied) will be done and the various trade-off will be discussed. Based on this analysis a interconnection scheme will be picked.

Chapter 5 This chapter demonstrates the performance of the final PV system that is mounted onto the drone.

Chapter 6 Finally, conclusions and recommendations are given in this chapter.

Appendix A This first appendix contains a substantial amount of research that would not fit in the main part of this text. Please take a look at this section since much of what is discussed throughout the text is explained in great detail in appendix A. For this reason, it is referred to extensively throughout the thesis.

Appendix B MATLAB code of the model that is discussed in [Chapter 3](#).

CHAPTER 2

Programme of Requirements

As discussed in [Chapter 1](#), the main goal of this project is to develop a solar energy system that will extend the battery life or rather flight time of a drone. Since drones are in high demand in both the consumer, industrial and military sector the possibilities with such a system are endless and its contribution will be substantial.

2.1 Market Assumptions

The military does not necessarily need an alternative energy source to deploy their drones and because of the lacking efficiency of today's solar cells a project like this will not be implemented by them in the near future. Also the consumer market is not ideal for this product as 'toy drones' are mostly used for leisure only, consumers will not be willing to pay extra for this alternative energy source when they have enough spare batteries and can easily swap them whenever they want. The industrial sector is the most suitable sector for an alternative, low-cost and superior fuel technology since there are plenty of commercial applications and business processes that are relatively long and cannot be interrupted which will directly benefit from (or even be possible at all thanks to) longer flight time (e.g. transport).

2.2 Goals & Limitations

During the first meetings with the supervisors a *realistic* system that fully powers the drone with solely solar energy was considered but quickly dismissed. In [Chapter 3](#) and [Chapter 4](#), it is clear that with the current solar cell technology and the drone that was provided, a fully solar powered drone is not possible. With the lacking efficiency of the cells, a great amount of cells would be necessary which the drone that was used cannot carry. Even if it could, with that many cells the product would become too large in size, making it ill-suited for commercial and industrial purposes.

Flight Extension

According to our supervisors, who are deeply involved with sustainable (solar) energy, a 25% increase in flight time is already a remarkable achievement.

Modelling

To design a working product, first its viability has to be proven by simulations. As a matter of fact, since part of this assignment has to do with the power management of the complete drone, a model will have to be developed from scratch. This, despite being theoretical, is also part of the final product and can (thanks to its universality and scalability) be used for large-scale future projects.

2. Programme of Requirements

Final Product

Since a considerable amount of time will be spent on modelling and hardware development usually happens in multiple iterations, it will not be realistic to demand a neat, fully working product. The primary accomplishment should be the model and configuration design (cell placement) which will be used to build a prototype. After all of the prototype's major problems are determined, they should be documented and even be researched so that there clear roadmap for the start of a possible next iteration even after the BAP project.

With these goals and limitations in mind, the following requirements have been set.

2.3 Mandatory Requirements

These are criteria that the system should always comply with and can be subdivided into functional and non-functional requirements. Functional requirements being requirements of what the system must *do*, and non-functional requirements being *attributes* that the system must have (such as performance, security, usability, maintainability, etc.).

Functional requirements

[1.1] At all times, the solar system should not cost more energy than it delivers. Equation 3.12 shows that each cell including wiring costs approximately 0.98 W, therefore $P_{system} \geq 0.98$ W.

This is without external effects like lower irradiance and wind.

[1.2] With the PV system mounted onto the drone, stable flight must be maintained.

[1.3] The PV system must be compatible with the other two subsystems (MC and PC).

Non-Functional requirements

[2.2] The model must be universal so it can be used for large-scale projects.

[2.3] The placement of the cells should not interfere with the aerodynamics of the drone.

[2.4] The system weight should not exceed 500 g, since that is the maximum lift capacity of the drone.

[2.5] The PV system must be compatible with the other two subsystems (MC and PC).

[2.6] The solar drone should withstand temperatures between -10 and 60 degrees centigrade.

2.4 Trade-off Requirements

[3.1] Reach a flight time extension of at least 25%.

[3.2] Use top-mounted cells instead of side-mounted cells (for most practical purposes, especially for cases with a high irradiance angle, top-mounted outperforms side-mounted).

CHAPTER 3

Power Management

In this Chapter the limitations of the system will be discussed and multiple design configurations based on these will be made. With a fairly simple theoretical model of the rotor, an estimate on energy consumption can be made. These theoretical results will be implemented into a model that determines how much weight each additional gram costs and calculates the optimum drone size for each situation. After considering these results and applying them to realistic situations (with their respective solar irradiances), a conclusion for the best design configuration will be made.

3.1 Limitations & Trade-offs

Since the goal of the goal of this project is to extend the flight time of a drone by designing the best possible solar module configuration, the drone and the solar cells itself will not designed and/or developed (however, they are carefully chosen). Below, the relevant limitations on this project relating to the drone and the solar cells are listed and will be taken into account if possible:

- Limitations on the drone:
 - aerodynamics
 - geometry
 - maximum lift power
 - energy needed to stay in the air for a certain time (with and without this project's additions)
 - motor efficiency
- Limitations on the solar cells:
 - efficiency
 - shape

Since the goal is to extend the battery life time *relatively*, the battery itself gives no limitations. Obviously, when battery A is assumed to have a n times larger capacity than battery B, the flight time of a drone with battery A can assumed to be n times larger. Since the flight time is n times larger, the time the solar modules are converting solar energy into electrical energy is also n times larger so that the extension of the battery life time scales linearly with the battery's capacity. Therefore, the relative extension remains constant for different battery capacities (assuming there are no negative effects on the flight time due to the increasing weight of the battery).

3. Power Management

Drone Limitations

The quad-copter that is used was not specifically designed for this particular project, it does not have any mounts or sufficient space to fit all the cells. To mount all the cells, significant structural and aesthetic additions will be made to support the PV-system which will definitely impact the aerodynamics of the quad-copter.

Aerodynamics

Since modelling the aerodynamics and design of the drone is beyond the scope of this project (it is in fact a project of its own), the focus will not be placed on that. As long as the original uniform square-shape of the drone is maintained the possible extra effects on the aerodynamics due to the systems will be diminished, that is, if they are there at all. Section 3.2 deals with the structural design of the system.

Geometry

The geometry (c.q. shape) of the drone depends in combination with the aerodynamics how the solar cells can be placed, which will have influence on the amount of power converted. Moreover, the geometry of the drone will have influence on the shading of the cells. Again, since the drone is not designed for this particular project the geometry will not be ideal and therefore limits the potential extension of the fly time. Section 4.2 deals with (partial) shading and discusses why it will be ignored in this project.

Lift Power

Since the PV system adds quite a lot of weight to the drone, the addition of the PV system affects the lift power the most. The drone is rated for 0.5 kg lift capacity, so from the start it is known that the system should not weigh more than 0.5 kg (for this specific drone, motor and propeller size).

Solar Cell Limitations

Efficiency & Temperature Performance

The efficiency of solar cells is known as the modern day bottleneck for projects based on solar energy. The IBC cells have a limited efficiency of 22% and according to the manufacturer superior temperature performance. Even though these bottlenecks are very real it was not necessary to spend time on temperature analysis and efficiency improvements since the cells can easily be swapped for cells with superior performance in future projects.

3.2 Configuration Designs

Taking into account the limitations mentioned in Section 3.1, three configurations are designed and discussed throughout Chapter 3:

Top mounted

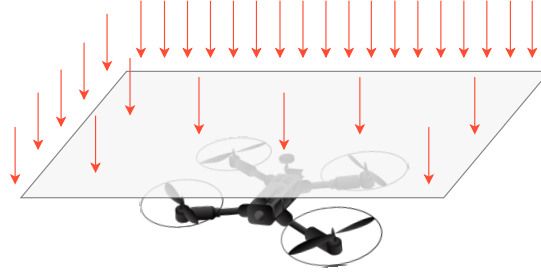


Figure 3.1: Only top-mounted cells.

Top-Side mounted

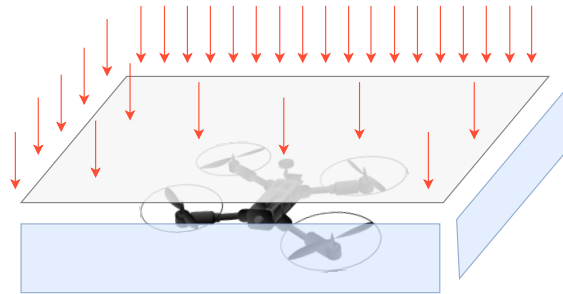


Figure 3.2: Top-mounted and side-mounted cells.

Top-Bottom mounted

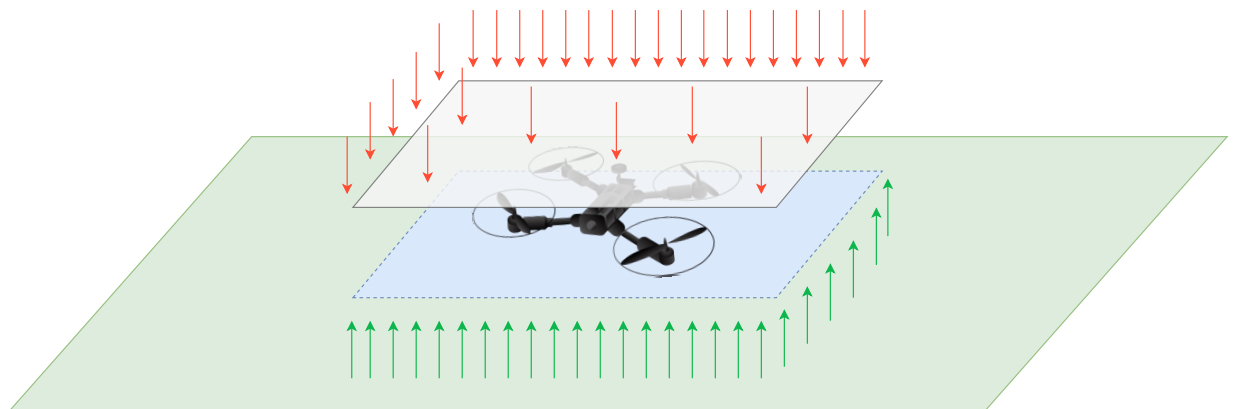


Figure 3.3: Both top-mounted and bottom-mounted cells.

3.3 Modelling Energy Consumption

To be able to know what net power the solar cells deliver, the extra power required to lift the weight of the solar system has to be calculated. If carrying the solar system requires more power than it will convert, obviously it does not make sense to add the solar system at all.

Roughly speaking, there are three different fly modi: taking off, hovering and landing. For the calculation of the required power to lift the extra weight, only hovering is considered. Calculating the power needed for taking off and landing is much more complex than hovering, and it can be justified that only taking into account the hovering modus is sufficient to make an estimation of the average power needed during a flight. Taking off requires more power than hovering, due to the potential energy which is added to the drone. The difference between the required power for hovering and landing is again the potential energy (which was added during taking off), so that the average power for taking off and landing will be the required power for hovering (neglecting the energy loss due to friction). In Equation (3.1) and (3.2) this is captured symbolically.

$$E_{takingoff} = E_{hovering} + E_{potential} \quad (3.1)$$

$$E_{landing} = E_{hovering} - E_{potential} \quad (3.2)$$

To estimate the power required for hovering, multiple aspects need to be taken into account. Equation (3.3) is used to calculate the total power required (see [Appendix A.1](#)):

$$P_{hovering} = K_1 \cdot \frac{F_n^{3/2}}{r} \cdot n \cdot \eta \quad (3.3)$$

where K is an air density coefficient [$\text{m}\sqrt{\frac{\text{m}}{\text{kg}}}$], F_n is the force [N] that needs to be exerted per propeller to hover, r is the radius [m] of the propellers, n the number of propellers and η the total efficiency of the DC motors. The radius of the used propellers is 0.13 m. The air density coefficient can be calculated as follows:

$$K_1 = \sqrt{\frac{1}{2\pi\rho_{air}}} \quad (3.4)$$

Assuming a temperature of $T = 288$ K, $\rho_{air} = 1.225$ kg/m³ and therefore $K = 0.360$ $\text{m}\sqrt{\frac{\text{m}}{\text{kg}}}$. The density of air is assumed to be constant, therefore the difference in required power lies in the difference of the gravitation of the system (for different weights). The gravitational force is divided over the total amount of propellers n .

$$F_n = \frac{m \cdot g}{n} \quad (3.5)$$

$$m = m_{drone} + m_{battery} + m_{solar} \quad (3.6)$$

The conventional standard value of gravitational acceleration is 9.81 m/s². The mass of the drone $m_{drone} = 0.680$ kg (including the additional surface to place the solar cells on) and the mass of the battery $m_{battery} = 0.2499$ kg. To illustrate the relation between the extra required power and the mass, Equation (3.3) is re-written:

$$P_{hovering} = K'_1 \cdot K'_2 \cdot m^{3/2} \quad (3.7)$$

where K'_1 is a coefficient based on the geographical variables and K'_2 based on the specific drone specifications:

$$K'_1 = g \cdot \sqrt{\frac{g}{2\pi\rho_{air}}} \wedge K'_2 = \sqrt{\frac{1}{n\eta^{2n}r^2}} \quad (3.8)$$

with η the efficiency the specific brushless DC motor. This is typically 85 – 90% (worst case scenario of 85% is assumed).

Since the relation between mass of the solar system m_{solar} and the required power $P_{hovering}$ is non-linear (see Equation (3.7)), every addition of a solar cell requires a different amount of power: adding a 81st solar cell requires more power than adding a 1st solar cell. Therefore, a linear approximation has to be done in order to be able to calculate the extra average power needed for lifting a solar cell. To calculate the additional required power per cell, first the power $P_{without}$ without the solar cells is calculated (only the drone and its battery). After that, the power P_{with} which includes the solar cells, is calculated. To determine the extra power P_{solar} required to add the solar system, $P_{without}$ is subtracted from P_{with} .

$$P_{solar} = P_{with} - P_{without} \quad (3.9)$$

The extra power P_{solar} is calculated for different numbers n of solar cells. To calculate the total mass of the solar cells, the wiring is included. 10 cm of wiring is assumed to be needed ($l_{wire} = 10$ cm) for each solar cell to connect to the other one (this is determined by a qualitative measurement). Since the density ρ_{wire} of the copper wires is 2.9 g/m, the following formula for calculating the mass m_{solar} of each solar cell can be used:

$$m_{solar} = n \cdot (m_{cell} + l_{wire} \cdot \rho_{wire}) = n \cdot 7.79 \cdot 10^{-3} \quad (3.10)$$

With Equation (3.3) to (3.10), the graph in Figure 3.4 is plotted. As can be seen in Equation (3.3), there is no linear relation between the extra required power and the number of solar cells added. Nevertheless, a linear approximation can be made for the total mass between $m = 1.0$ kg and $m = 1.5$ kg (see Figure 3.4), using MATLAB's Curve Fitting Tool (MATLAB, 2015).

Using this tool, the required power can be approximated as:

$$P_{solar} = 129.5 \cdot m \quad (3.11)$$

where the 95 % confidence bounds of the coefficient are [1.014, 1.023]. From this, it can be determined that adding 1,0 g of additional weight requires 0.1295 W of extra power. Since the weight of a solar cell (including its wiring) is known, a linear relation between P_{solar} and the number of solar cells n can be approximated:

$$P_{solar} = 0.9756 \cdot n \quad (3.12)$$

where the 95 % confidence bounds of the coefficient are [0.9710, 0.9801]. With this, it can be concluded that a solar cell which does not convert more than 0.9756 W will not positively contribute to the fly-time and should therefore not be added.

*Note that this (approximated) linear relation changes for a different drone weight, battery weight, propeller size and number, fly modus and temperature and it implies the **minimal** extra power required, since friction and power losses due to the other components (micro-controller and converter) was neglected.*

3. Power Management

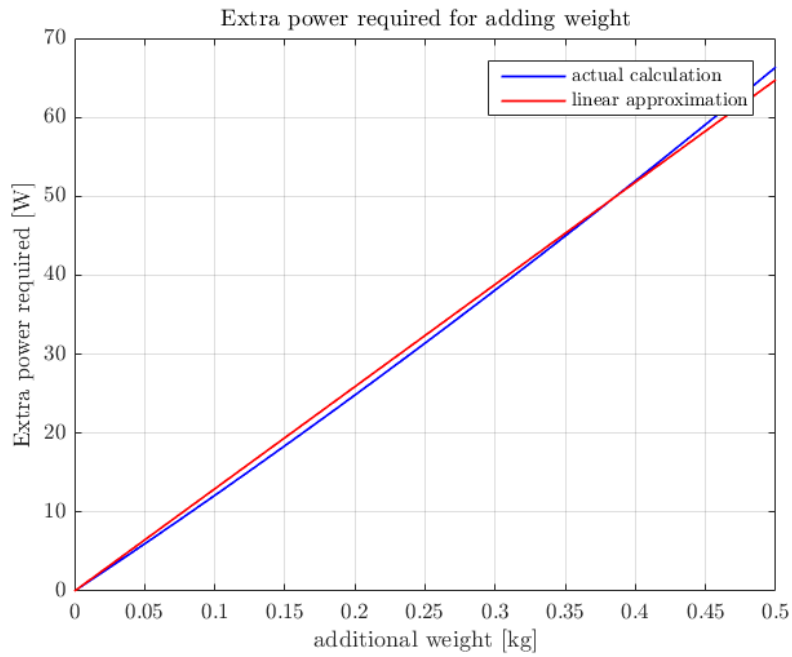


Figure 3.4: In this Figure, the extra required power per mass unit is shown. It is assumed that the total system does already weigh 0.9299 kg, which is the weight of the drone plus the weight of the battery. Both the actual calculation and the linear approximation can be seen.

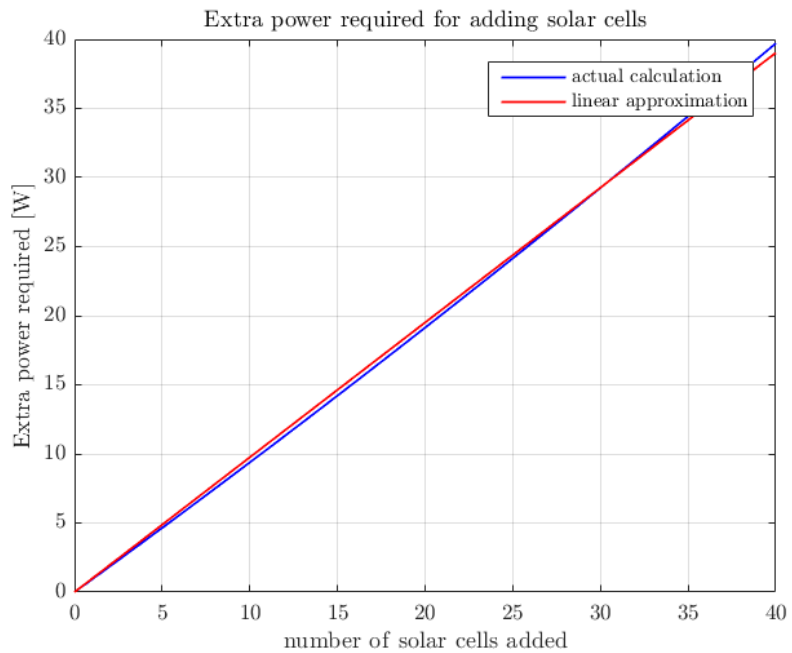


Figure 3.5: In this Figure, the extra requires power for different numbers of added solar cells is shown. It is assumed that the total system does already weigh 0.9299 kg, which is the weight of the drone plus the weight of the battery. Both the actual calculation and the linear approximation can be seen.

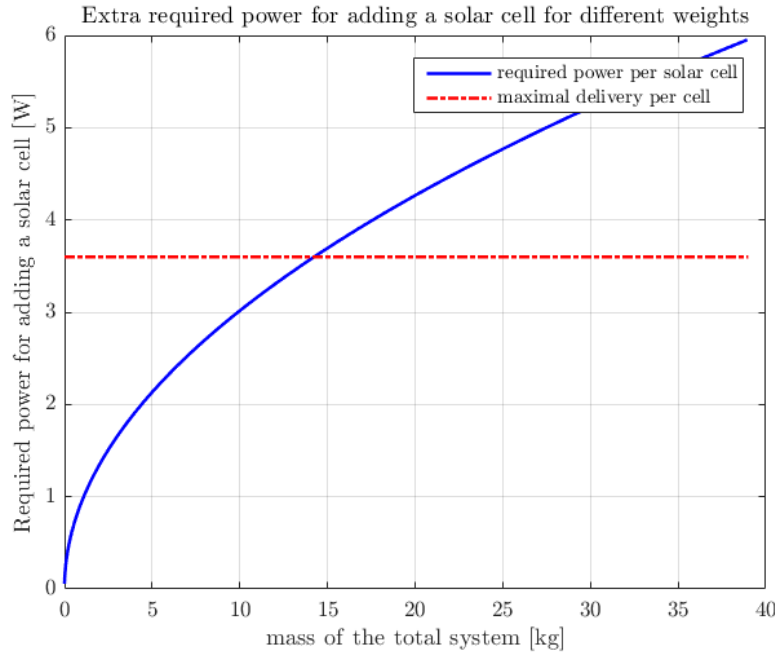


Figure 3.6: The extra required power per solar cell addition is plotted versus the total weight of the system.

Maximum weight of the total system

As stated earlier, the extra required power per solar cell increases with the weight of the total system. Although the weight of the drone and battery is constant for this application, for an increasing m_{drone} and $m_{battery}$ there will be a maximum weight where the IBC solar cells cannot convert enough solar power to compensate for the required extra power to lift its weight.

To calculate the maximum weight of the total system, for which the solar system requires more power than it delivers, the derivative of Equation (3.7) with respect to the number of solar cells n is calculated. The derivative is plotted as a function of the mass of the total system, as can be seen in Figure 3.6.

For a total mass of 14.24 kg, the additional power required after adding a solar cell (including the wiring) is more than 3.6 W, which the IBC solar cell maximally can convert (see Section 3.4). Therefore, it can be concluded that the mass of the drone, including the solar system cannot exert 14.24 kg. Otherwise, it will lower the total fly-time. Although this will not have limitations on this project, it limits the amount of (potential) applications of quad-copters with a solar system, since for example transporting humans or other heavy objects will not be possible.

Note that this maximum weight changes for a different propeller size and number, fly modus, temperature and type of solar cells. This weight implies the weight for which the solar system would definitely not be beneficial anymore (converting less power than extra required to lift), since friction and power losses due to the other components (micro-controller and converter) was neglected.

Optimal number of solar cells

In Appendix A.2, it can be seen that for an irradiance of 300 W/m^2 , the optimal number of cells for relative and absolute increase of fly-time is respectively 36 and 28 cells. These number increases with an increasing irradiance.

Since the geometry of this specific quad-copter does not allow placing 28 or 36 solar cells, or even

3. Power Management

more for higher irradiance, as many solar cells as possible should be placed on the quad-copter to come close to this optimum. In case of a quad-copter with a higher area, these optima should be taken into account.

Qualitative validation of energy model

To qualitatively validate the energy model discussed in Section 3.3, two simple measurements are done. With these two measurements, the quad-copter flies with a fully charged battery with different weights. The fly-time for these different cases are measured. With Equation (3.13), the average energy consumption P_{av} can be calculated and compared with the average energy consumption as estimated according to the energy model.

$$P_{av} = \frac{C_{battery} \cdot V_{oc}}{t_{fly}} \quad (3.13)$$

where $C_{battery} = 4000$ mAh and $V_{oc} = 12$ V.

In the first measurement, the fly-time of the quad-copter with total weight 929,9 g is measured to be 20 min and 2 s. In the second measurement, the fly-time of the quad-copter was measured to be 16 min and 10 s with a total weight of 1220,2 g. In Table 3.1, the measured and modelled average energy consumption are calculated for each case, with Equations (3.13) and (3.11).

Table 3.1: Measured values vs energy model

Total weight [g]	Measured P_{av} [W]	Modelled P_{av} [W]
929,9	143,8	120,4
1220,2	178,1	158,0

Since no friction and losses in other components are considered in the energy model, there are differences between the modelled and measured values. Although the measured values of P_{av} differ with respectively 16,3 % and 11,3 % from the values according to the energy model, the model can be validated as a useful model to estimate the minimal solar energy which additional weight should convert.

The extra weight which is added in the second case lead to an increase of 23.9 % power required. In the energy model, this increase is 31.2 %.

3.4 Irradiance

The average (yearly) amount of solar power received at Earth's atmosphere is around 342 W/m², of which ca. 30 % is scattered or reflected back to space, so that 239 W/m² is available for capturing and converting into electrical energy. The annual effective solar irradiance varies worldwide from 60 to 250 W/m². The annual average of solar irradiance in the Netherlands is between 100 and 125 W/m².

The chosen PV cells have an area of 0.015625 m². With the average efficiency η of 23% (see Section 1.4) taken into account and ignoring potential shading, the average power a solar cell can produce is

$$P = Ir \times A \times \eta \quad (3.14)$$

where P is the produced power [W], Ir is the solar irradiance [W/m²], A is the effective area of the solar cell [m²] and η is the efficiency [%]. According to Equation (3.14), the maximum power (with an irradiance of 1000 W/m²) that can be converted by the IBC solar cells is 3.6 W.

Latitude	Yearly mean of irradiance (W/m ²)
-90°	121
-65°	151
-45°	216
-25°	267
0°	292
25°	267
45°	216
66°	151
90°	121

Table 3.2: The yearly mean of the solar irradiance at various latitudes (Wald, 2018)

For the solar system to be beneficial, a solar cell has to convert at least 0.9756 W (see Equation (3.12)). With the specific effective area and efficiency as mentioned, the solar irradiance should at least be 271 W/m². Based on this equation (3.14) and assuming no shading effects, the average power an IBC solar cell can produce in the Netherlands is 0.3125 W, which is less than the minimal power of 0.9756 W. On a yearly basis, the solar system will therefore only decrease the fly-time of the quad-copter. However, if the solar drone will not be used during the evening and/or night it can be beneficial provided that the solar irradiance is at least 271 W/m². In Figure 3.7, the average solar power in Europe can be seen for different times of the average day in January and July. In January and July, the average irradiance during daytime (9:00 till 16:00 GMT) is respectively 595 and 890 W/m². However, with these values the angle of incidence is not taken into account. Therefore, the actual power received at Earth's surface in Europe is 382.5 W/m² and 572.1 W/m² during daytime on a typical winter and summer day respectively (see Appendix A.3). Both values are greater than the minimal of 271 W/m², from which it can be concluded that the solar system would theoretically increase the fly-time if it will only be used during daylight.

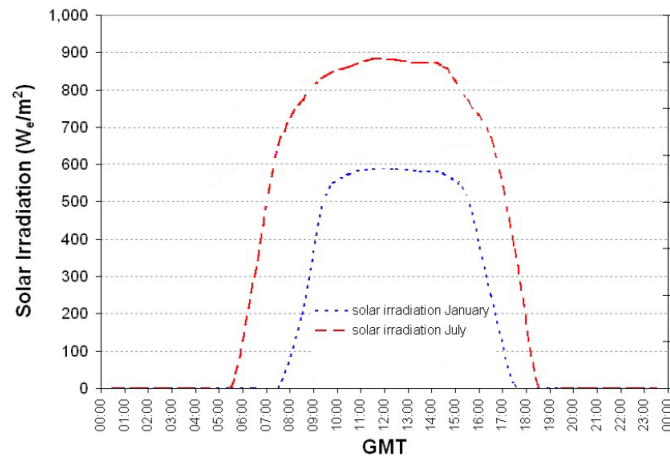


Figure 3.7: Typical winter and summer day solar irradiance. Note that this graph is plotted without taking the angle of the sunlight on Earth's surface into account (Summerer et al., 2003)

To make the solar system beneficial on a yearly basis (average of night and day), the quad-copter should only fly in an area close to the 0° latitude, see Table 3.2.

Surface reflection and gain per bottom cell

In case of solar cells pointed at the earth, no direct solar irradiance assumed. However, solar radiation can be reflected by the surface beneath the cells so that they are irradiated either way.

3. Power Management

Material	Albedo
Highly reflective roof	0.60 - 0.70
White paint	0.50 - 0.90
Grass	0.25 - 0.30
Brick and stone	0.20 - 0.40
Trees	0.15 - 0.18
Red or brown tile	0.10 - 0.13
Concrete	0.10 - 0.35
Corrugated roof	0.10 - 0.16
Tar and gravel	0.08 - 0.20
Asphalt	0.05 - 0.20

Table 3.3: Typical albedo of urban surfaces (Li, 2016)

The amount of solar irradiance which is being reflected depends on the material (and the shape) of the surface. The rate of irradiance being reflected is called the solar reflectance or albedo. In Table 3.3, typical albedo of urban surfaces are listed.

The reflected solar radiation per unit area can be calculated using the albedo of the material:

$$I_{reflected} = r \cdot I_{solar} \quad (3.15)$$

where r is the albedo of the material (Li, 2016).

With Equation (3.12), the minimal power that a cell has to convert to be beneficial is determined to be 0.9756 W. For a typical winter day in Europe, the average solar irradiance during daytime (9:00 till 16:00 GMT) is 382.6 W/m². Then, with Equation (3.15), the bottom cells are only beneficial for albedo > 0.71. From Table 3.3, it can be seen that this is only the case white paint. Since it cannot be assumed that albedo > 0.71, no bottom cells are placed.

3.5 Configuration Selection

Based on Section 3.4, no bottom cells are placed on the quad-copter since the amount of solar energy they can convert is smaller than the amount of energy which is needed to carry the extra weight. Therefore, only cells are placed on top or on the side of the quad-copter.

As discussed in Section 3.3, the optimal number of solar cells with respect to the absolute increase of the fly-time is 28 for an irradiance of 300 W/m². For higher irradiances, this optimum lies at a higher amount of cells. Since the geometry of this specific quad-copter does not allow to place 28 cells, as much as possible should be placed (since this the amount of solar cells will not exceed the optimal number). The total amount of solar cells that can be placed on top of the quad-copter is 20 (see Chapter 5).

Since only 20 cells can be placed on top of the drone, to reach the optimal number of cells, 8 more cells should be placed. As already mentioned, the top-bottom mounted configuration will give a lower performance than the top mounted configuration. To determine which of the two remaining configurations, top or top-side mounted, gives the best performance, the differences in irradiation for top and side mounted cells should be considered. Side mounted cells can only convert more power than top mounted cells if $\alpha_s < 45^\circ$, which is not the case in Europe (see Appendix A.3).

Also, the electrical interconnection of the solar cells should be considered. The greatest difference between top and top-side mounted is that in case of a top-side mounted configuration, the different solar cells will be shaded differently. Since a SP interconnection (see Chapter 4) will be chosen, it is important that there is no partial shading to achieve the best performance. Furthermore,

since the top mounted cells are all assumed to be shaded equally, two strings should be made (top and side mounted cells) for the top-side mounted configuration, which would require an extra micro-controller and converter in comparison with the top mounted configuration. This extra weight and the partial shading problem leads to the conclusion that a top mounted configuration will give the best results for this application.

To conclude, assuming a constant α_s , top *or* side mounted configuration is the most ideal configuration. Due to the partial shading, top-side configuration is non-ideal: there is no trade-off in this. Since it cannot be stated that $\alpha_s < 45^\circ$ in Europe, top mounted configuration has to be chosen to get the highest performance.

CHAPTER 4

Electrical Configuration

After picking the most optimal solar cells and their configuration, these cells have to be interconnected in the most efficient way. In the following section, multiple (theoretical) configurations are compared. After choosing the most efficient configuration for our application, in [Chapter 5](#) the practical configuration (considering the amount of solar cells and the electrical configuration used) is explained in more detail.

4.1 Mismatch Losses

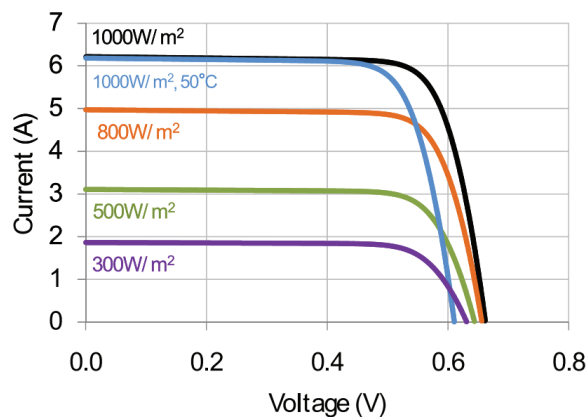


Figure 4.1: ($I - V$) curves of identical IBC Sunpower cells for different irradiance and temperature (Corporation, 2010)

Photo-Voltaic (PV) arrays are usually composed of large numbers of solar cells. These individual cells can have different current-voltage ($I - V$) characteristics, even though the cells may be identical. These differences can occur due to shading effects and are called $I - V$ mismatch. $I - V$ mismatches are undesired since they cause power losses in the array, via the following four mechanisms (Shams El-Dein et al., 2013):

1. The maximum power point of the total array is not coherent with the individual modules, which causes power losses if the modules are not operating at their own MPPs.
2. The maximum power point tracker (micro-controller) is misled by the existence of multiple power maximums.
3. Bypass diodes (if used, see Section 4.4) are turned ON. PV modules with bypass diodes across them will not produce any useful power when these diodes are ON. Moreover, these diodes create additional power loss due to their on-resistance.

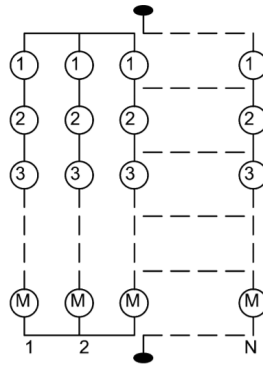


Figure 4.2: A series-parallel (SP) array with size $(M \times N)$ (Gautam and Kaushika, 2002)

4. Some parallel connected PV modules can suffer from reverse currents due to $I - V$ mismatch. This reverse current causes modules to absorb power, instead of producing.

4.2 Interconnection Schemes

The three most important PV module configurations are Series Parallel (SP), Bridge Linked (BL), and Total Cross Tied (TCT). In SP (see Figure 4.2), cells are connected in a series to form a string and then the strings are connected in parallel to increase the total current of the PV array. It is simple, economical and there is no redundancy in connections.

In TCT configuration (see Figure 4.3), the cells are connected in parallel and hence the cell voltages are the same, each cell current is summed up and connected in series with another set of PV cells. TCT has more parallel circuits, thereby minimizing the number of bypass diodes used (see Section 4.4). Moreover, TCT reduces the overall effect of mismatch losses. A disadvantage of the TCT configuration is that more wires are needed to connect the solar cells.

A BL configuration (see Figure 4.4) is derived from the connections in a bridge rectifier and it has a lower number of redundant connections compared to TCT, but it has a lower performance compared to the series-parallel configuration. In comparison with TCT, a BL configuration needs less wiring.

Theoretical studies on reliability of PV arrays show that TCT interconnection is more reliable than SP and is capable of doubling the operational life time of the array (since TCT has more parallel circuits than SP) (Samikannu et al., 2016).

Partial shading affects the modules' short circuit currents thus affecting the modules' output currents at their MPPs. This leads to a lack of coherence between modules' MPPs and array's MPP. In case of SP, this issue is more severe than that in case of TCT (Bingöl and Özkaya, 2018).

4.3 Different configuration for different shading situations

If no shading is assumed, the three configurations discussed in Section 4.2 have the same output power. Differences in performance occur if the PV array is (partial) shaded.

Considering a 6×6 array, the maximum power for different shading situations is simulated per configuration. In total there are 6 different shading cases simulated, with each a combination of the three different solar irradiation values: 300 W/m^2 , 600 W/m^2 and 1000 W/m^2 . All shading cases are carried out at $25 \text{ }^\circ\text{C}$. The 6 different cases are illustrated in Figure A.11 (Bingöl and Özkaya, 2018).

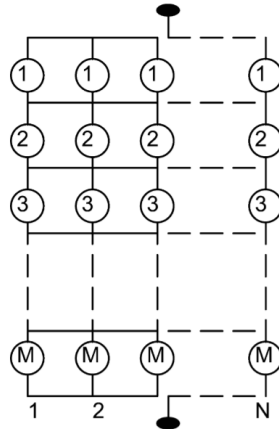


Figure 4.3: A total cross tied (TCT) array with size $(M \times N)$ (Gautam and Kaushika, 2002)

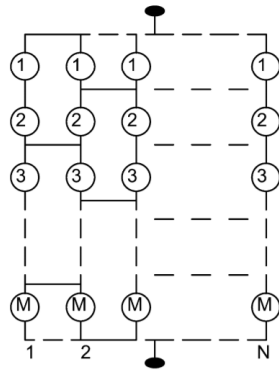


Figure 4.4: A bridge-linked (BL) array with size $(M \times N)$ (Gautam and Kaushika, 2002)

The results of the simulation can be seen in [Appendix A.6](#). For all the different cases, the TCT configuration gives the highest power output. Only for case 1, in which the individual cells of three strings are equally shaded, the output power of SP, TCT and BL are the same.

To have even better results for shading patterns as illustrated in cases 1 to 5 (non-random), the physical location of the modules in a TCT connected array can be arranged based on the magic square pattern. With this pattern the shading effect is distributed over the entire array, without altering the electrical connection of the modules in the array (Bingöl and Özkaya, 2018). This can be seen in [Appendix A.4](#). A disadvantage of this magic square pattern is that more wiring per solar cell is needed, so that more power is needed to be able to fly (see Equation 3.11).

4.4 Bypass diodes

Typically, PV arrays are not only composed of PV cells, but also of bypass diodes. These diodes are mainly intended to prevent the PV cells from power consumption when shaded or damaged. In case of a SP configuration, the need and use of bypass diodes become most clear. One cell can potentially prevent the total current of a string to flow (if shaded or damaged), and therefore minimize the total output power. Furthermore, they prevent the cells from working near the avalanche zone (Diaz-Dorado et al., 2010).

Nevertheless, the use of bypass diodes also has some side-effects. If the PV array is partially shaded, the bypass diodes change the $I - V$ characteristics (and therefore also the $P - V$ characteristics) as can be seen in [Figure 4.5](#). Without the use of diodes, the global maximum power point (GMPP)

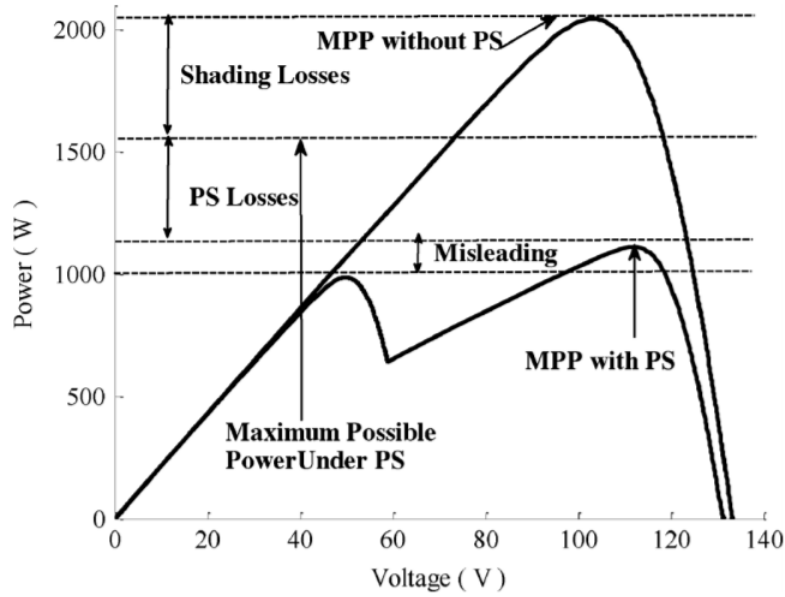


Figure 4.5: Shading, partial shading and potential misleading losses (El-Dein et al., 2012).

will be lower, since the shaded cells will lower the total (string) current. This is the reason that in many application bypass diodes are used. But besides increasing the GMPP, the diodes also affect the $I - V$ characteristics in another way: an extra local maximum power point is created. Although this does not necessarily have to be a disadvantage, in this application it potentially is. With an extra maximum power point, the software of the micro-controller has to be more complex to find the GMPP. If this software does not succeed in finding the GMPP (if it is misled), the first local MPP can be considered to be the point for which the output power is maximal. The difference between the output power of the local and global maximum power point is then called the misleading power loss, which can also be seen in Figure 4.5.

Furthermore, with the use of bypass diodes the total weight of the system increases, depending on the diode configuration (see Section 4.4). This weight implies that more power will be needed to carry the weight in-air, see Equation (3.11).

In Appendix A.5, the importance of different diode characteristics for this application is explained so that the most ideal type of bypass diodes can be bought (or designed).

Configuration

The configuration of the PV array and the way the bypass diodes are connected determine the total energy production. There are two main bypass diode configurations (Díaz-Dorado et al., 2017), see Figure 4.6:

1. overlapped bypass; configurations in which one or more cells are covered by more than one bypass diode are considered overlapped
2. no-overlapped bypass; every cell is covered by at most one bypass diode

In Appendix A.5 it can be seen that for most applications, the no-overlapped diodes give the best results. There is a trade-off between cost (no-overlapped requires more diodes) and performance. It is commonly believed that a greater quantity of bypass diodes leads to a better performance (for both the overlapped and no-overlapped configuration) in (partial) shading conditions. However,

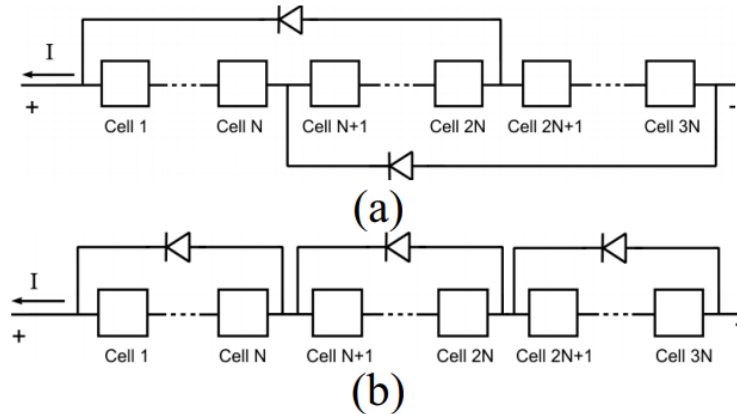


Figure 4.6: Bypass diodes (a) overlapped (b) no-overlapped (Díaz-Dorado et al., 2017)

under some conditions less bypass diodes lead to a better performance: hence, a greater quantity does not necessarily guarantee better performance. This can be seen in [Appendix A.5](#).

Micro-inverters

If you are using multiple strings into an MPPT controller, then even with bypass diodes, one string with one shaded panel and a bypass diode will not contribute anything to the input to the MPPT inverter, since the MPP will be above the new voltage of that string. The net effect then will be no better than the same string without bypass diodes.

So if you have shading which affects different series strings differently, and the two strings would end up combined into one DC input, you will be better off with micro-inverters. With the micro-inverters, the output of each string will be independent and may even produce partial power from a partially shaded array, depending on the input voltage range the micro-inverter can handle. In comparison, micro-inverters are more complex than bypass diodes.

4.5 Conclusion on electrical configuration

Based on the previous Sections, there are some trade-offs which have to be discussed to come to the most ideal electrical configuration for this application. In this Section, a choice will be made for which configuration to choose (SP, BL or TCT), whether to add bypass diodes (and which configuration) and or to add micro-inverters.

SP vs TCT vs BL

The advantages and disadvantages per configuration (discussed in Section 4.2) is summarized in Table 4.1.

With the 6 different criteria, both the SP, BL and TCT have the same score. Nevertheless, some criteria have a higher priority.

For the statically flying quad-copter application, the following assumption can be made:

$$A_{solar} \ll A_{cloud} \quad (4.1)$$

Having this in mind, it can be assumed that the solar system will not be partially shaded by a cloud. If the PV array is shaded, every cell will have the same shading condition. Since the

4. Electrical Configuration

	SP	BL	TCT
Complexity	+	+/-	-
Weight	+	+/-	-
Performance*	-	+/-	+
Number of bypass diodes	-	+/-	+
Redundancy in connections	+	+/-	-
Operational life time	-	+/-	+

Table 4.1: SP vs TCT vs BL

* = assuming partial shading

quad-copter will be used for an application in which it flies statically, no other shading than cloud shading is assumed. Therefore, the performance (see Table 4.1) will have a low priority, since it considers the performance under partial shading conditions.

In Section 4.5 there will be stated that no bypass diodes will be used. Therefore, the number of bypass diodes (see Table 4.1) also has a low priority.

The remaining criteria are the complexity, weight, redundancy and operational life time. Considering only the complexity, weight and redundancy, the SP configuration is the best choice. Before being able to make a choice between SP and TCT, the priority of weight has to be determined using Equation (3.11) and (3.10). With a TCT configuration, the total length of wiring needed per cell is assumed to be twice the length of wiring needed for a SP configuration. Therefore, the extra weight per cell is 0.29 g (for TCT against SP). This means that the extra power needed per cell will be at least 0.038 W. Considering Equation (3.12), this is an increase of 3.8%. Since this is a relatively small percentage, also the weight has a low priority.

To conclude, generally the greatest advantage of TCT is the performance. Since this does not apply to this application, no bypass diodes are used and since a greater operational life time does not outweigh the complexity and redundancy in connections, the SP configuration is the best configuration for this application.

Bypass diodes and micro-inverter

In Section 4.4, the advantages and disadvantages of the use of bypass diodes are discussed. The biggest advantage of using bypass diodes is a better performance considering partial shading of the PV array. The disadvantages of the bypass diodes are the extra weight, cost and the extra local maximum power point which can lead to power losses.

Since no partial shading is assumed (see Equation (4.1)), the biggest advantage will not apply. Therefore, there is not a trade-off in using bypass diodes: the consequences of adding bypass diodes will mainly be the above described disadvantages. In consequence, no bypass diodes will be added to the configuration.

For the same reason, no micro-inverters are added.

CHAPTER 5

Solar Drone Performance

In the design of the solar system, multiple trade-offs are made. The first trade-off which had to be made was which configuration to choose of the solar cells on the quad-copter. In Section 3.5 can be read that the top mounted configuration gives the best performance for this application. Besides the configuration of the solar cells, the best electrical configuration had to be designed. In Section 4.5 it can be seen that a SP configuration, without the use of bypass diodes and/or micro-inverters, would suit best for this application.

As stated in Section 3.5, the optimal number of solar cells placing on the quad-copter is 28. Since this number cannot be reached with this specific drone, as many solar cells as possible are placed (provided that it will not influence the aerodynamics of the quad-copter). The final practical configuration can be seen in Figure 5.1.

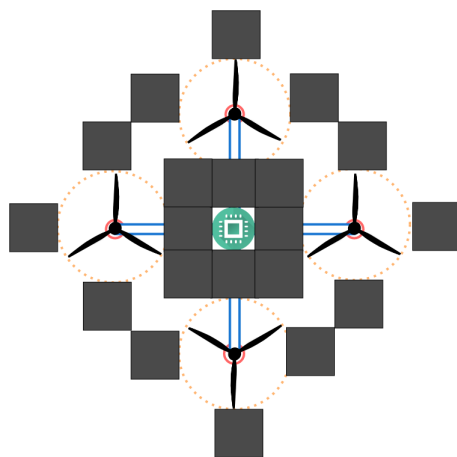


Figure 5.1: Practical design of the solar system on the quad-copter

In total, 20 solar cells are placed. With Equation (3.12), it can be calculated that the extra weight of these cells (including its wiring) require 19.5 W to lift. The total power which can be converted by the 20 cells on a typical winter and summer day in Europe can be calculated with Equation (3.14) and Figure 3.7. On a typical winter day, the total solar power converted by the solar system is on average 27.5 W. On a summer day, 41.2 W is converted during day time (9:00 till 16:00 GMT).

The total net power and the relative increase of fly-time can be seen in Table 5.1. A power requirement of 143.8 W is assumed for a quad-copter without extra weight of the solar system to calculate the increase in fly-time (see Table 3.1).

Note: the increase in fly-time is a maximal increase, assuming no partial shading and no losses in the other components of the quad-copter. Furthermore, the required power for the extra weight is

5. Solar Drone Performance

Table 5.1: Measured values vs energy model

	$P_{required}$ [W]	P_{solar} [W]	$P_{net,solar}$ [W]	Increase fly-time
Typical winter day	19.5	27.5	8.0	5.6 %
Typical summer day	19.5	41.2	21.7	15.1 %

according to the energy model described in Section 3.3 the minimal required power. Therefore, the actual increases can potentially come close to these theoretical maximums, but will not actually reach this values when using the same components (on average during summer or winter).

CHAPTER 6

Conclusion & Discussion

The original aim was an extension of at least 25% of the battery life. After analysing the limitations of the drone and the cells, multiple configurations were designed and an energy model that determines power usage, energy costs per solar cell and the optimum amount of cells was developed. After running the model, validating the results, multiple interconnection schemes were considered (SP, BL, TCT) and the system was mounted. Unfortunately the extension of the battery life was lower than was hoped, with a 5.6% increase in winter and 15.1% increase in summer because of lacking efficiency of the panels and nonideal angles of incidence (see Section 3.3). Despite the fact that the target efficiency was not achieved, the results are still of great value as all of the developed models are universal and show when and for which efficiency/irradiance it will yield the desired results.

The process of choosing and obtaining the best quad-copter as possible (lowest weight, highest area available for placing solar cells) turned out to be very time consuming. The most feasible and ideal quad-copter, that has been used for this project, is not available on the market and therefore has very complex software to fly the quad-copter. For safety reasons, it was not possible to fly the quad-copter and perform measurements on the performance.

The energy model discussed in Section 3.3 forms an important part of this thesis. However, by creating this energy model multiple assumption are made so that the required power per mass is a minimal amount of power. As can be seen in Table 3.1, the only validation on this model is done by two simple measurements. The result of these measurements showed that the energy model can be used to estimate the minimal required power for this application, however it turned out that this model is not very accurate (differences of 16.3 and 11.3 % for measured and calculated power requirements). For future research, by doing at least 10 measurements for different masses, the model can be modified based on this actual results which leads to more accurate estimations.

While choosing the optimal solar cell configuration, the assumption is made that the top mounted configuration gives better results than a top-side mounted configuration, since an extra string and therefore an extra converter and micro-controller is required for top-side configuration (which means extra weight). Although with the energy model (Equation (3.11)) the extra required power can be estimated, with this model the solar energy which can be converted by the side mounted cells cannot be calculated accurately because partial shading then plays a role. A simple measurement would have given a solid answer on the question whether side mounted cells can convert more energy than is needed to lift these cells (including the extra converter and micro-controller), but due to a limiting amount of time and the aforementioned safety reasons, this measurement could not be done. This is a measurement which has to be done for future research if this specific quad-copter will be used (see Section 6.1). However, for a self-designed quad-copter, this would not be an issue since there would be enough space on top of the quad-copter to reach the optimal number of solar cells so that it would not be beneficial at all to place more cells.

6.1 Future Research

In future research, the focus should lay on the following subjects:

- self designing a quad-copter
- obtain a more accurate energy model
- research on solar cells
- obtaining highest efficiency while combining all the subcomponents

A limiting factor in this specific project has been the geometry and weight of the quad-copter. In future work, a quad-copter should be designed to achieve a higher increase of fly-time. A greater area to place the solar cells on without influencing the aerodynamics, a lower weight, internal wiring, big propellers and highly efficient brushless motors increase the fly-time. Furthermore, a more accurate energy model should be obtained. As mentioned in [Chapter 6](#), few measurements are performed to validate the model. In future research, more measurements should be performed so that eventually a more accurate model can be achieved.

Besides, one of the biggest limitations has been the efficiency of the solar cells which are currently available on the market. In future research, a more efficient (and lightweighted, if possible) solar cell should be designed to achieve significant increases in the fly-time. Finally, the focus should lay on the efficient combination of all the subcomponents. For example, what is the optimal weight of the converter if it means that a heavier converter can potentially have a greater efficiency? Also, the optimal weight of the battery (which is assumed to increase for increasing capacity) should be determined.

Appendices

APPENDIX A

Studies, Figures and Derivations

A.1 Hovering Power

Assuming drone A and B with respectively high and low fly times. Suppose that both drones have identical batteries, drone A will be able to stay in the air for a longer time since it takes less energy for drone A. Therefore, the energy needed to stay in the air (which is a drone characteristic) determines the potential battery lifetime extension, since drone B will not convert as much energy as drone A. Although this is not the focus of this project, it has to be taken into account for the aforementioned reasons.

$$A_{cylinder} = \pi r^2 \quad (A.1)$$

$$V_{air} = A_{cylinder} \cdot h_{cylinder} = A_{cylinder} \cdot (v \cdot t) \quad (A.2)$$

$$m_{air} = Q_{air} \cdot V_{air} = Q_{air} \cdot A_{cylinder} \cdot (v \cdot t) \quad (A.3)$$

$$F = \frac{m_{air} \cdot v_{final}}{t} = \frac{m_{air} \cdot 2v}{t} \quad (A.4)$$

$$F = \frac{[Q_{air} \cdot A_{cylinder} \cdot (v \cdot t)] \cdot 2v}{t} = 2Q_{air} \cdot A_{cylinder} \cdot v^2 \quad (A.5)$$

$$v_{rotor} = \sqrt{\frac{F}{2Q_{air} \cdot A_{cylinder}}} \quad (A.6)$$

Note that the power is equal to the rate at which work is done or in other words rate at which energy is consumed. Work is given by $W = F \cdot s$ where s denotes displacement in a straight line in the direction of the force, thus power is

$$P = W/t = F \cdot s/t = F \cdot v \quad (A.7)$$

$$P_{hover} = K \cdot \frac{F^{3/2}}{r} \quad (A.8)$$

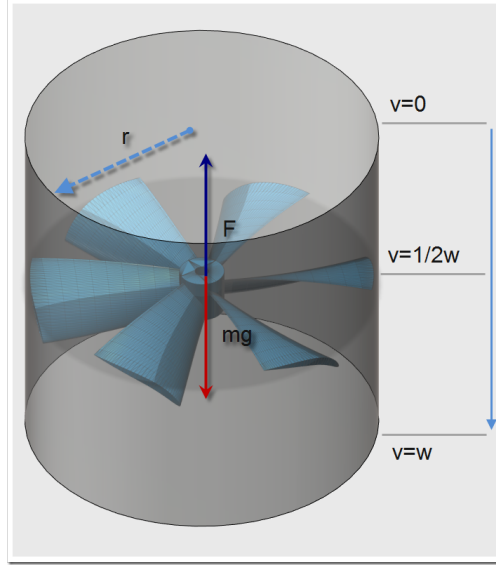


Figure A.1: Rotor Model

A.2 Optimal number of solar cells

To determine which configuration of cells gives the best results in terms of increasing the fly-time, the optimal number of solar cells has to be determined. Assume two cases: in case A, 1 solar cells is placed. In case B, 2 solar cells are placed. In case A, the energy converted per solar cell is higher than the energy converted per cell in case B. The reason for this is that in case B the total weight of the system increases so that it takes more power to lift the system (so that the fly-time would decrease). However, the *total* amount of power converted is for case B higher than for case A (since this increase in required power is significantly lower), which eventually will lead to an increase in fly-time. Since the required power for lifting and the weight of the system does not scale linearly (see Equation (3.3)), there will be an optimal amount of solar cells for which the fly-time is maximal. The relative and absolute increase of fly-time are calculated separately, since they will have different optima for the aforementioned reasons.

Assuming a fully loaded battery at $t = 0$, the amount of energy left in the battery while hovering (without the addition of solar energy) can be determined as follows:

$$E_{battery,without} = C_{battery} \cdot V_{oc} - t \cdot P_{hovering} \quad (\text{A.9})$$

where $P_{hovering}$ increases for a higher number of solar cells (see Equation (3.3)). The energy which is converted by the solar system can be determined as follows:

$$E_{gain} = t \cdot P_{solar} \quad (\text{A.10})$$

where P_{solar} increases for an increasing amount of solar cells (see Equation (3.9)). Adding these different energy levels, the total energy stored in the battery (assuming it will not overload) is

$$E_{battery,with} = C_{battery} \cdot V_{oc} + t(P_{solar} - P_{hovering}) \quad (\text{A.11})$$

provided that $P_{hovering} > P_{solar}$. Namely, if $P_{hovering} < P_{solar}$, the energy level of the battery will not increase with corresponds to an infinite fly-time.

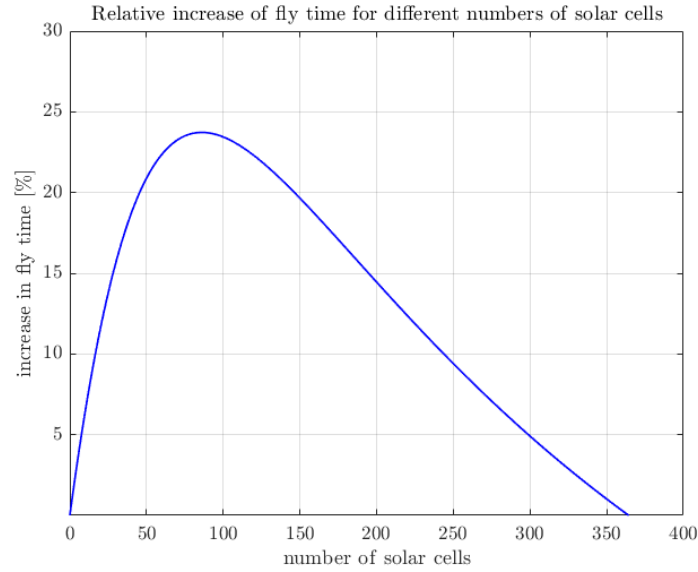


Figure A.2: The maximum output power achievable for different numbers of solar cells in case of an irradiance of 500 W/m^2

In Figure A.2, the relative increase of total fly-time for an irradiance of 400 W/m^2 of different amounts of solar cells can be seen. In Table A.1, the optimal amount of solar cells with respect to both the relative and absolute increase of fly-time can be seen for different irradiances. As can be seen, for an irradiance of 200 W/m^2 the optimal number of solar cells is 0, since it will require more power to lift solar cells than they can convert. For an irradiance of 800 W/m^2 or higher, there is a range of optimal amount of solar cells. For this range, the relative and absolute increase of the fly-time is namely infinite, which means the quad-copter can fly fully on solar energy.

Table A.1: Optimal number of solar cells with respect to the relative and absolute increase of the fly-time, based on the energy model discussed in Section 3.3

Solar irradiance [W/m^2]	$n_{optimal,relative}$	$n_{optimal,absolute}$
200	0	0
300	36	28
400	87	50
500	117	65
600	138	83
700	152	114
800	112 - 236	112 - 236
900	62 - 456	62-456
1000	47 - 664	47 - 664

A.3 Irradiance: Optimal Tilt Angle

The tilt angle of a solar energy system is one of the most important parameters as it directly impacts the power that can be harvested by the panels. Figure A.3 depicts a 3D overview of the irradiance beam and the panel placement.

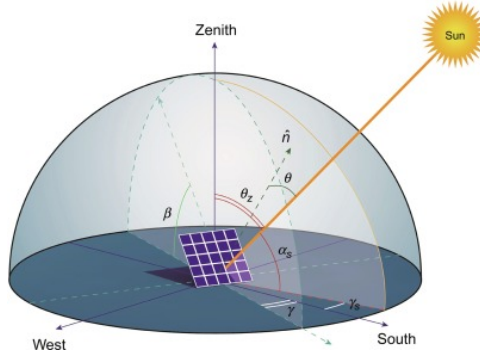


Figure A.3: 3D overview (Meyer et al., 2012)

The power that can be absorbed is dependent on the angle of incidence θ_i , which is the difference between the angle of irradiance α_s and the angle of the normal vector (90° or 0°). P_{direct} is the irradiance in W/m^2 and its angle α_s is depicted in orange in Figure A.4.

$$P_{panel} = P_{direct} \cdot \cos(\theta_i) \quad (\text{A.12})$$

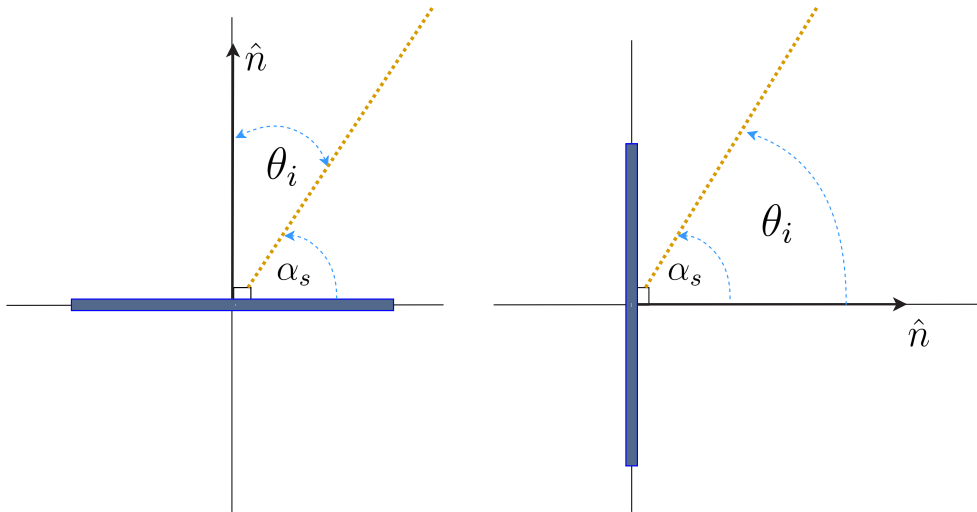


Figure A.4: Two configurations: Top-mounted (left) and side-mounted (right). Angle of incidence θ_i , solar panel in blue

To get an idea of the power that can be gained by switching configurations the optimum tilt angle has to be taken into account. This angle varies on a daily basis per region. Nevertheless, on a yearly basis, the optimal tilt angle can be determined which gives the best performance on average. Since the optimal tilt angle depends on the geological location of the PV modules, the optimal angle per region can be seen in Figure A.5. In Europe the optimal angle is $40 - 50^\circ$ (Breyer and Schmid, 2010).

A higher α_s leads to a lower tilt angle, likewise a lower α_s leads to higher tilt angle. Therefore, in the northern hemisphere, where the sun is lower, tilt angles are higher.

Considering this optimum tilt, one can choose the most suitable configuration to optimise θ_i . With this and equation A.12 in mind, it is clear that the side-mounted configuration is only useful in areas with a very low angle of irradiance (northern hemisphere). For $\alpha_s > 45^\circ$, top mounted cells can convert more power. For $\alpha_s < 45^\circ$, side mounted cells give better performance.

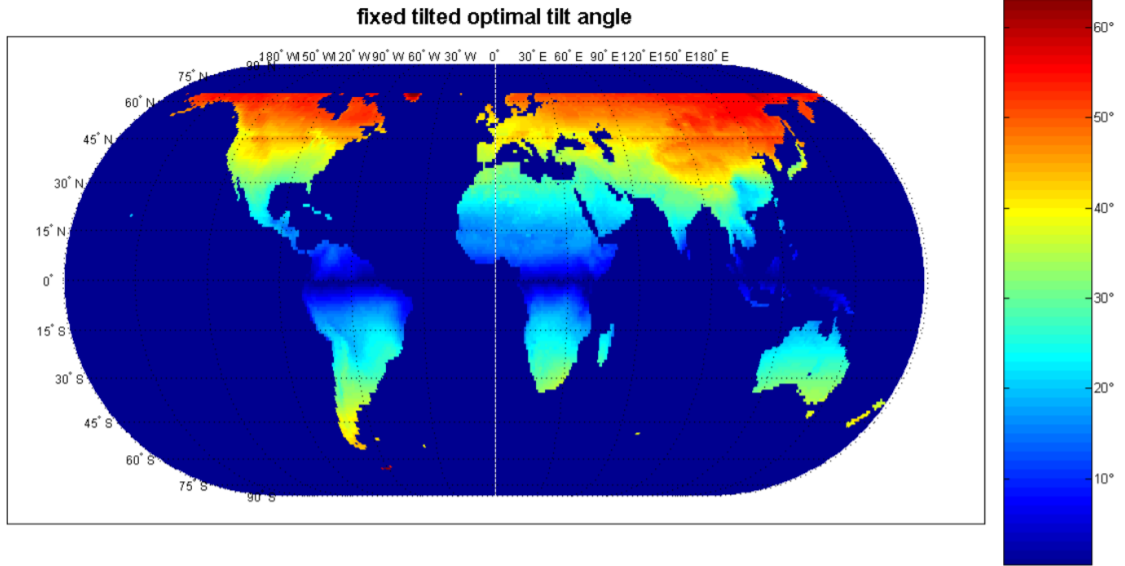


Figure A.5: Optimal tilt angles for fixed tilted PV systems for optimised irradiation on module surface (Breyer and Schmid, 2010)

A.4 Magic Square

A magic square is an array of numbers consisting of distinct integers $1, 2, 3, \dots, n^2$, with n the number of columns and rows (assuming an $n \times n$ matrix). The sum of all the numbers of each row, each column and of the main and secondary diagonal is the same value: the magic constant or the magic sum M . The constant M can be calculated by the rule

$$M = \frac{[n(n^2 + 1)]}{2} \quad (\text{A.13})$$

The method can also be applied for non-square matrix of size $m \times n$. Similarly, for an $m \times n$ matrix with integers $1, 2, 3, \dots, nm$, each row adds to the same total M and each column to the same total N . These are respectively called the row magic constant and column magic constant, and can be calculated as follows:

$$N = \frac{[m(nm + 1)]}{2} \quad (\text{A.14})$$

$$N = \frac{[n(nm + 1)]}{2} \quad (\text{A.15})$$

As said, the electrical connections between the panels in the array remain unaltered. The voltage and current equations have no change or alteration in them as the electrical configuration remains the same. However, the same row of panels in TCT arrangement distributes the shading effect over

various rows in MS arrangement, thus maximizing the current entering the node. This eventually leads to increased power output.

The MS scheme evidently avoids the need for complex Maximum-Power-Point-Tracking algorithms, since the MS pattern only has one Global Maximum Power Point at the right most peak in the PV curve. For different shading patterns, measurements show that positioning the modules of the array according to MS pattern provides improved performance under partially shaded conditions (Samikannu et al., 2016).

A.5 Bypass diode configuration

In a simulation, 20 serial-connected PV modules with both overlapped and no-overlapped diodes are considered. The layout of the PV modules has 30 rows of PV cells. Thus, the two different bypass configurations have the same physical distribution of the PV cells. In the simulation, for 31 different shading cases the maximum MPPs of the PV arrays are calculated, see Figure A.6.

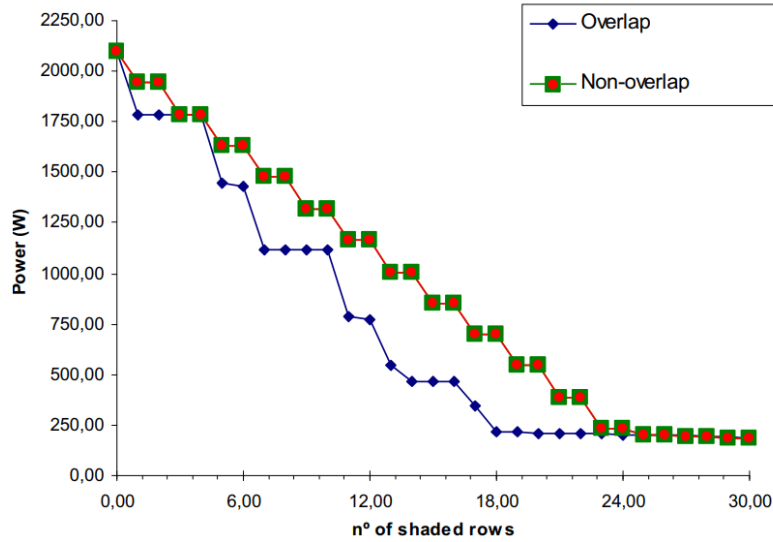


Figure A.6: Bypass diodes (a) overlapped (b) no-overlapped (Diaz-Dorado et al., 2010)

The power losses in PV modules with overlapped diodes can be a significant fraction of its peak power, because of the PV cells consuming power. In the PV modules with no-overlapped bypass diodes, the power losses are only produced by the power consumption of the diodes.

In general, the no-overlapped configuration has a better performance. The power losses of this configuration would only be noticeable if there were too many bypass diodes. Moreover, since more diodes will be needed for the no-overlapped configuration it is more expensive than the overlapped configuration (Diaz-Dorado et al., 2010).

Effect of the numbers of bypass diodes

It is commonly believed that a greater quantity of bypass diodes leads to a better performance in (partial) shading conditions. However, under some conditions less bypass diodes lead to a better performance (see Figure A.7). Hence, a greater quantity doesn't necessarily guarantee better performance.

In this Simulink simulation, 18 of the 36 series connected solar cells are considered as the shading group. The ratio of the irradiance of the shaded and unshaded group is called the shading factor (F_S). The temperature is considered constant during the simulation.

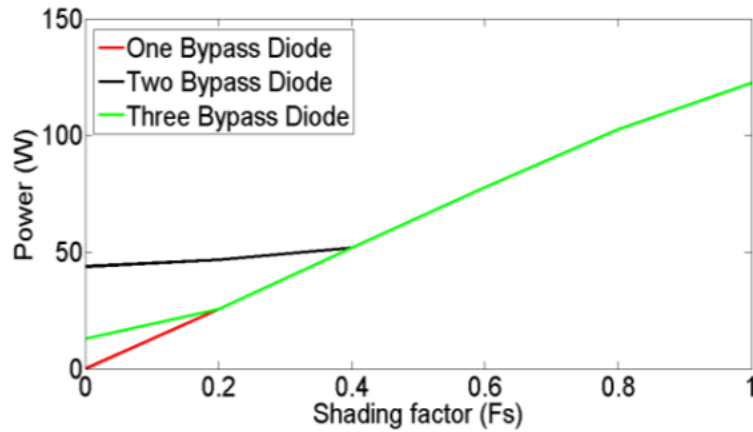


Figure A.7: Maximum power vs shading factor for a different quantity of bypass diodes in a no-overlapped configuration (Teo et al., 2017).

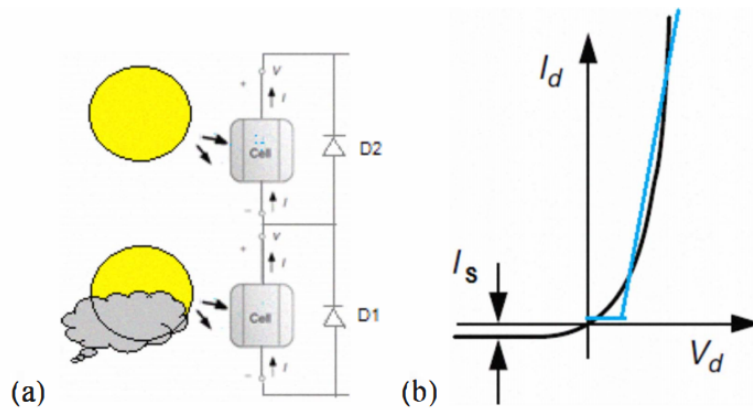


Figure A.8: (a) two cells connected in series (b) diode characteristics and linear approximation (Ziar et al., 2012)

Three cases are considered: one bypass diode, two no-overlapping bypass diodes and three no-overlapping diodes. From Figure A.7 can be seen that generally, three no-overlapping bypass diodes give the best performance, although mentioned earlier this is not always the case (for $0 \leq F_S < 0.4$).

From these results, it can be concluded that (as commonly believed) *in most cases* three diodes outperform one and two diodes. Hence, although it depends on the shading conditions, one should prefer a greater quantity of bypass diodes for conditions where the shading factor differs (Teo et al., 2017).

Characteristics bypass diode

In another simulation that is carried out, the importance of the bypass diode characteristics is analyzed. In this Simulink simulation, two solar cells which are connected in series and having no-overlapped diodes are studied (see Figure A.10).

From the linear approximation of the $I - V$ curve of a diode (direct bias) two characteristics should be highlighted, namely:

1. the on resistance; which can be determined from the slope of the line

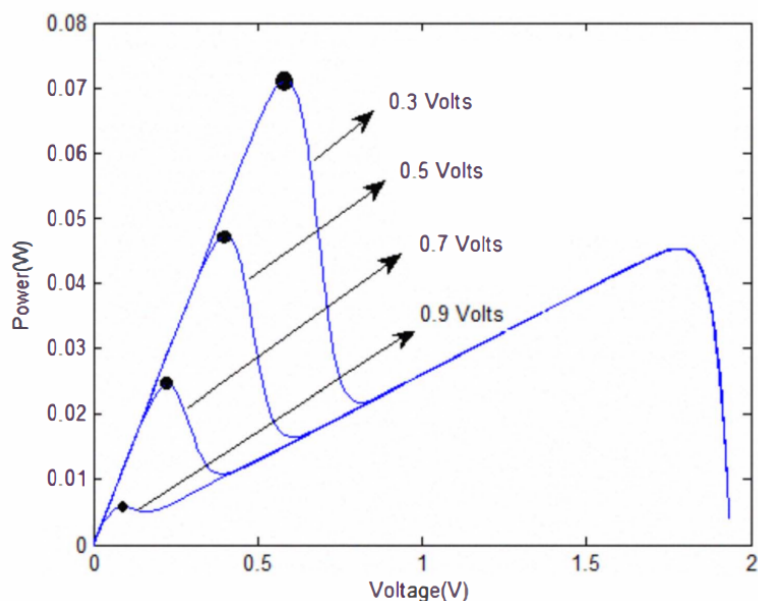


Figure A.9: Simulated P-V curve for different forward voltages (Ziar et al., 2012)

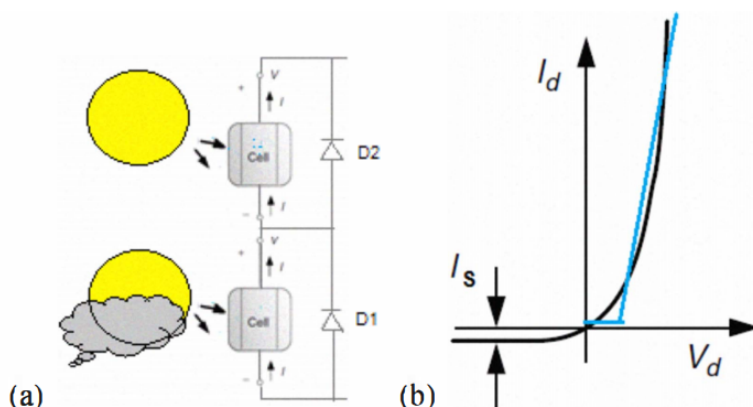


Figure A.10: (a) two cells connected in series (b) diode characteristics and linear approximation (Ziar et al., 2012)

2. the forward voltage; which can be determined from the distance between the origin and the point where the curve starts increasing

It is obvious that a low on resistance will lead to better performance: there will be less loss. The simulation therefore focuses only on the effect on the performance by changing the forward voltage. Assuming a shading condition where the upmost cell is fully irradiated by the sun - thus 1000 W/m^2 - and the lower cell is partially shaded so that the received radiation is 200 W/m^2 . Simulating this case for 4 different forward voltages of the bypass diodes (0.3 V, 0.5 V, 0.7 V and 0.9 V) gives the result which can be seen in Figure A.9.

In Figure A.9, two MPP can be seen. The first MPP varies for different forward voltages, the second MPP remains the same. For a forward voltage bigger than 0.7 V, the first MPP changes from the global MPP to a local MPP. To verify the simulation, an actual measurement has been done for the same case. The results of this experiment can be seen in Table A.2. In this table, the

A.6. Simulation of configurations for different shading situations

MPP	$V_{forward} = 0.21 \text{ V}$	$V_{forward} = 0.432 \text{ V}$	$V_{forward} = 0.627 \text{ V}$	$V_{forward} = 0.819 \text{ V}$
MPP 1	0.216 W	0.176 W	0.160 W	0.128 W
MPP 2	0.168 W	0.168 W	0.168 W	0.169 W

Table A.2: Measured Maximum Power Points for different values of bypass diode forward voltage (Ziar et al., 2012)

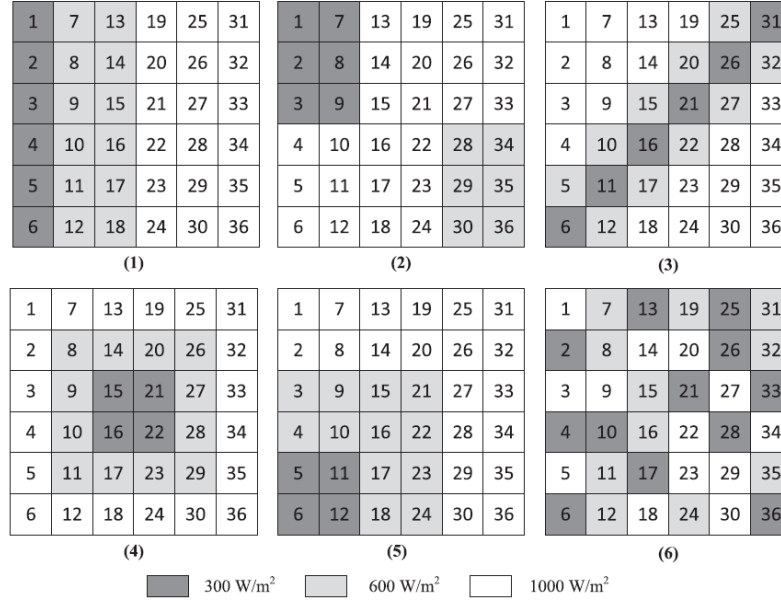


Figure A.11: Partial shading (1) Case 1, (2) Case 2, (3) Case 3, (4) Case 4, (5) Case 5, (6) Case 6 (Bingöl and Özkaya, 2018)

first MPP that occurs is called MPP 1, the second MPP 2 (just as in Figure A.9). The bold values show the global MPP.

As shown in Table A.2, MPP 1 changes by changing in diode forward voltage. This could also be seen in the simulation, where the first maximum decreased for an increasing forward voltage. In the experiment, for a voltage bigger or equal than 0.627 V, the first MPP changes from the global to a local MPP. This lead to lower output power. Thus, from both the simulation and the measurement it can be concluded that a lower forward voltage leads to a better performance.

Looking at the bypass diode characteristics, it can be concluded that both the turn on resistance and the forward voltage are important. Turn on resistance of diodes cause power loss. However, forward voltage has a higher rate of importance and should therefore be as small as possible (Ziar et al., 2012).

A.6 Simulation of configurations for different shading situations

	Configuration	P_{\max} (W)	V_{\max} (V)	I_{\max} (A)
Case 1	SP	1242	97.5	12.74
	TCT	1242	97.5	12.74
	BL	1242	97.5	12.74
Case 2	SP	1112.2	102.3	10.87
	TCT	1340.4	99.61	13.46
	BL	1176.8	106	11.09
Case 3	SP	725.748	87.75	8.271
	TCT	898.2565	100.3	8.954
	BL	734.5931	85.3	8.612
Case 4	SP	1103.4	104.6	10.55
	TCT	1163.2	104.3	11.15
	BL	1106.8	103.9	10.65
Case 5	SP	1096.2	103.7	10.57
	TCT	1159.3	104.3	11.12
	BL	1116.1	104.5	10.68
Case 6	SP	682.9867	48.96	13.95
	TCT	1002.2	101.3	9.885
	BL	732.2328	103.9	7.045

Table A.3: Simulation result of shading cases for different configurations (Bingöl and Özkaya, 2018)

APPENDIX B

Computer Code

The following MATLAB script contains the energy model explained in [Chapter 3](#):

```
% BAP Project 2018/2019
% Solar Drone - Group D
% PV System
% By: David de Best and Dewwret Sitaldin
% Last modified: 18-06-2019

% Relation between power and mass of the solar system

%  $P = (K/r) * (F/n)^{1.5} * n * \eta$ 

% Initializing values
% Assuming a temperature of 288 K and a propellor diameter of 82,5 cm

Q_air = 1.225; % kg/m^3
g = 9.81; % m/s^2
r = 0.26/2; % m
n = linspace(0,40,40); % number of solar cells (0 to 40)
eta = 0.85;

% mass of drone and battery = 0.9299 kg
% max lift weight is 0.5 kg
m_drone = 0.680; % kg
m_battery = 0.2499; %kg
m_converters = 0;
m_solar = (7.79 * n) / 1000; % mass of total solar cells
m = linspace(0,2,20); % mass of total system (0 to 2 kg)
n_prop = 4;
m_extra = linspace(0,0.5,20);

% NEW Formula
K1 = g * sqrt( g / (2 * pi * Q_air) );
K2 = sqrt(1 / (n_prop * eta^(2* n_prop) * r^2 ) );
P = K1 * K2 * (m_drone + m_battery + m_converters + m_solar).^(3/2);
P_without = K1 * K2 * (m_drone + m_battery + m_converters).^(3/2);
P_new = P - P_without;
P_m = K1 * K2 * m.^(3/2);

P_extra = (K1 * K2 * (m_drone + m_battery + m_converters + m_extra).^(3/2)) - P_without;

% Calculation of the theoretically maximum weight
n_max = linspace(0, 5000,5000);
m_max = (n_max * 7.79)/1000;
P_max = K1 * K2 * m_max.^(3/2);
P_max_per_cell = diff(P_max);
m_max_plot = m_max(1:4999);
n_max_plot = n_max(1:4999);

% Plotting
```

B. Computer Code

```
% This plot shows how much extra power is required to add a number of solar
% cells (the weight of a solar cell does not include the wiring)
x1 = linspace(0,40,40);
a1 = 0.9756; % 95% confidence = [0.9710, 0.9801]
y1 = a1*x1;

% plot(n, P_new, 'b', 'LineWidth', 1)
% xlabel ('$\mathrm{number\ of\ solar\ cells\ added}$', 'fontsize', 12, 'interpreter','latex','rot', 0)
% ylabel ('$\mathrm{Extra\ power\ required\ [W]}$$$', 'fontsize', 12, 'interpreter','latex','rot', 0)
% set(get(gca,'YLabel'),'Rotation',90, 'Fontname', 'Times')
% title ('$\mathrm{Extra\ power\ required\ for\ adding\ solar\ cells}$$$', 'fontsize', 12, 'interpreter','latex','rot', 0)
% set(groot, 'defaultAxesTickLabelInterpreter','latex'); set(groot, 'defaultLegendInterpreter','latex');
% grid on
% hold on
% plot(x1, y1, 'r', 'LineWidth', 1)
% legend ('actual calculation', 'linear approximation')

x2 = linspace(0,0.5,20);
a2 = 129.5; % 95% confidence = [128.1,130.8]
y2 = a2*x2;
%
% plot(m_extra, P_extra, 'b', 'LineWidth', 1)
% xlabel ('$\mathrm{additional\ weight\ [kg]}$', 'fontsize', 12, 'interpreter','latex','rot', 0)
% ylabel ('$\mathrm{Extra\ power\ required\ [W]}$$$', 'fontsize', 12, 'interpreter','latex','rot', 0)
% set(get(gca,'YLabel'),'Rotation',90, 'Fontname', 'Times')
% title ('$\mathrm{Extra\ power\ required\ for\ adding\ weight}$$$', 'fontsize', 12, 'interpreter','latex','rot', 0)
% set(groot, 'defaultAxesTickLabelInterpreter','latex'); set(groot, 'defaultLegendInterpreter','latex');
% grid on
% hold on
% plot(x2, y2, 'r', 'LineWidth', 1)
% legend ('actual calculation', 'linear approximation')

% This plot shows how much extra power is required to put 20 more solar
% cells on the drone, assuming that there are already 20 cells placed on
% it (again neglecting the extra weight of wiring and the weight of an
% extra controller).

% plot(m, P_m, 'b', 'Linewidth', 1.5)
% xlabel ('$\mathrm{mass\ of\ the\ total\ system\ [kg]}$', 'fontsize', 12, 'interpreter','latex','rot', 0)
% ylabel ('$\mathrm{required\ power\ for\ lifting\ the\ weight\ [W]}$', 'fontsize', 12, 'interpreter','latex','rot', 0)
% set(groot, 'defaultAxesTickLabelInterpreter','latex'); set(groot, 'defaultLegendInterpreter','latex');
% set(get(gca,'YLabel'),'Rotation',90, 'Fontname', 'Times')
% title ('$\mathrm{Required\ power\ for\ different\ weights}$$$', 'fontsize', 12, 'interpreter','latex','rot', 0)
% grid on
%
% plot(m_max_plot, P_max_per_cell, 'b', 'Linewidth',1.5)
% xlabel ('$\mathrm{mass\ of\ the\ total\ system\ [kg]}$', 'fontsize', 12, 'interpreter','latex','rot', 0)
% ylabel ('$\mathrm{Required\ power\ for\ adding\ a\ solar\ cell\ [W]}$', 'fontsize', 12, 'interpreter','latex','rot', 0)
% set(get(gca,'YLabel'),'Rotation',90, 'Fontname', 'Times')
% set(groot, 'defaultAxesTickLabelInterpreter','latex'); set(groot, 'defaultLegendInterpreter','latex');
% grid on
% title ('$\mathrm{Extra\ required\ power\ for\ adding\ a\ solar\ cell\ for\ different\ weights}$$$', 'fontsize', 12, 'interpreter','latex','rot', 0)
% hold on
% power_solar_cell = [3.6,3.6];
% n_power_solar_cell = [0,39];
% plot(n_power_solar_cell, power_solar_cell, 'r-.', 'LineWidth', 1.5)
% legend ('required power per solar cell', 'maximal delivery per cell')

% max weight = 14.24 kg

% -----

n_optimal = linspace(0,400,400); % number of solar cells (0 to 5000)
m_solar_opt = (7.79 * n_optimal) / 1000; % mass of total solar cells
ir = 500; %W/m^2
```

```

ir_opt = linspace(0,10,1000); %W/m^2
A = 0.015625;
eff_cell = 0.23;
n_ir = linspace(0,800,800);
m_solar_ir = (7.79 * n_ir) / 1000;

P_opt = K1 * K2 * (m_drone + m_battery + m_converters + m_solar_opt).^(3/2);
P_opt_ir = K1 * K2 * (m_drone + m_battery + m_converters + m_solar_ir).^(3/2);
P_without_opt = K1 * K2 * (m_drone + m_battery + m_converters).^(3/2);
P_new_opt = P_opt - P_without_opt;
P_new_opt_ir = P_opt_ir - P_without_opt;

P_gain_opt = ir * A * eff_cell * n_optimal;
P_gain_opt_ir = ir * A * eff_cell * n_ir;

P_net_opt = P_gain_opt - P_new_opt;
P_net_opt_ir = P_gain_opt_ir - P_new_opt_ir;
[optimal_P, optimal_n] = max(P_net_opt_ir);

% plot(n_ir, P_net_opt_ir, 'b', 'LineWidth', 1)
% xlabel ('$\mathrm{number}$ of solar cells added$', 'fontsize', 12, 'interpreter', 'latex', 'rot', 0)
% ylabel ('$\mathrm{Net}$ power gain of the solar system [W]$', 'fontsize', 12, 'interpreter', 'latex', 'rot', 0)
% set(get(gca, 'YLabel'), 'Rotation', 90, 'Fontname', 'Times')
% title ('$\mathrm{Net}$ power for different numbers of solar cells$', 'fontsize', 12, 'interpreter', 'latex', 'rot', 0)
% set(groot, 'defaultAxesTickLabelInterpreter', 'latex'); set(groot, 'defaultLegendInterpreter', 'latex');
% grid on
%
% plot(n_optimal, P_net_opt, 'b', 'LineWidth', 1)
% xlabel ('$\mathrm{number}$ of solar cells added$', 'fontsize', 12, 'interpreter', 'latex', 'rot', 0)
% ylabel ('$\mathrm{Net}$ power gain of the solar system [W]$', 'fontsize', 12, 'interpreter', 'latex', 'rot', 0)
% set(get(gca, 'YLabel'), 'Rotation', 90, 'Fontname', 'Times')
% title ('$\mathrm{Net}$ power for different numbers of solar cells$', 'fontsize', 12, 'interpreter', 'latex', 'rot', 0)
% set(groot, 'defaultAxesTickLabelInterpreter', 'latex'); set(groot, 'defaultLegendInterpreter', 'latex');
% grid on

% -----
% Optimum for fly time

C_battery = 4*3600; %As
V_oc = 12; %V
n_fly = 20; % number of solar cells (0 to 5000)
m_solar_fly = (7.79 * n_fly) / 1000; % mass of total solar cells
A = 0.015625;
eff_cell = 0.23;

% -----
ir_fly = 500; %W/m^2
%-----

P_fly_with_req = K1 * K2 * (m_drone + m_battery + m_converters + m_solar_fly).^(3/2);
P_fly_without_req = K1 * K2 * (m_drone + m_battery + m_converters).^(3/2);
P_fly_solar_req = P_fly_with_req - P_fly_without_req;
P_fly_solar_gain = A * eff_cell * ir_fly .* n_fly;

P_fly_net_gain = P_fly_solar_gain - P_fly_solar_req;

max_E = (P_fly_net_gain./P_fly_with_req) .* V_oc .* C_battery;
[gained_E, optimal_n_fly] = max(max_E)

E_0 = C_battery * V_oc;
% E_1 = E_0 - t*P_fly_with_req;
% E_2 = t * P_fly_solar_gain;
t_fly = E_0 ./ (P_fly_with_req - P_fly_net_gain);
t_fly_old = E_0 ./ P_fly_with_req;
abs_increase_t_fly = t_fly - t_fly_old;

```

B. Computer Code

```
increase_t_fly = ((abs_increase_t_fly) ./ t_fly_old) .* 100
% [max_increase, optimal_n_flytime] = max(increase_t_fly);
% [max_increase_abs, n_flytime_abs] = max(abs_increase_t_fly);
%
% n_rel_abs = [optimal_n_flytime, n_flytime_abs]
% gain_fly_rel_abs = [max_increase, max_increase_abs]

% plot(n_fly, max_E, 'b', 'LineWidth', 1)
% xlabel ('$\mathrm{energy}$ added to the battery [J]$', 'fontsize', 12, 'interpreter', 'latex', 'rot', 0)
% ylabel ('$\mathrm{number}$ of solar cells$', 'fontsize', 12, 'interpreter', 'latex', 'rot', 0)
% set(get(gca, 'YLabel'), 'Rotation', 90, 'Fontname', 'Times')
% title ('$\mathrm{Net}$ power for different numbers of solar cells$', 'fontsize', 12, 'interpreter', 'latex', 'rot', 0)
% set(groot, 'defaultAxesTickLabelInterpreter', 'latex'); set(groot, 'defaultLegendInterpreter', 'latex');
% grid on

plot(n_fly, increase_t_fly, 'b', 'LineWidth', 1)
ylabel ('$\mathrm{increase}$ in fly time [%]$', 'fontsize', 12, 'interpreter', 'latex', 'rot', 0)
xlabel ('$\mathrm{number}$ of solar cells$', 'fontsize', 12, 'interpreter', 'latex', 'rot', 0)
set(get(gca, 'YLabel'), 'Rotation', 90, 'Fontname', 'Times')
title ('$\mathrm{Relative}$ increase of fly time for different numbers of solar cells$', 'fontsize', 12, 'interpreter', 'latex', 'rot', 0)
set(groot, 'defaultAxesTickLabelInterpreter', 'latex'); set(groot, 'defaultLegendInterpreter', 'latex');
grid on
hold on
% plot(n_fly, abs_increase_t_fly)
% legend ('relative', 'absolute')
```

Bibliography

- Asia's first fully solar-powered quadcopter* (n.d.). <https://www.eng.nus.edu.sg/news/asias-first-fully-solar-powered-quadcopter/>. Accessed: 2019-06-12.
- Bingöl, O. and Özkaya, B. (2018). 'Analysis and comparison of different PV array configurations under partial shading conditions'. In: *Solar Energy* vol. 160, pp. 336–343.
- Breyer, C. and Schmid, J. (2010). 'Global Distribution of optimal Tilt Angles for fixed tilted PV Systems'. In: *horizon* vol. 2, no. 1.
- Corporation, S. (2010). *SUNPOWER, C60 Solar Cell Mono Crystalline Silicon*.
- El-Dein, M. S., Kazerani, M. and Salama, M. (2012). 'Optimal photovoltaic array reconfiguration to reduce partial shading losses'. In: *IEEE Transactions on Sustainable Energy* vol. 4, no. 1, pp. 145–153.
- Diaz-Dorado, E., Suarez-Garcia, A., Carrillo, C. and Cidras, J. (2010). 'Influence of the shadows in photovoltaic systems with different configurations of bypass diodes'. In: *SPEEDAM 2010*. IEEE, pp. 134–139.
- Diaz-Dorado, E., Cidrás, J. and Carrillo, C. (2017). 'Discretized model for partially shaded PV arrays composed of PV panels with overlapping bypass diodes'. In: *Solar Energy* vol. 157, pp. 103–115.
- Gautam, N. K. and Kaushika, N. (2002). 'An efficient algorithm to simulate the electrical performance of solar photovoltaic arrays'. In: *Energy* vol. 27, no. 4, pp. 347–361.
- Li, H. (2016). 'Chapter 11 - Pavement Thermal Modeling: Development and Validation'. In: *Pavement Materials for Heat Island Mitigation*. Ed. by Li, H. Boston: Butterworth-Heinemann, pp. 239–262.
- MATLAB (2015). *version 7.10.0 (R2015b)*. Natick, Massachusetts: The MathWorks Inc.
- Meyer, R., Schlecht, M. and Chhatbar, K. (2012). '3 - Solar resources for concentrating solar power (CSP) systems'. In: *Concentrating Solar Power Technology*. Ed. by Lovegrove, K. and Stein, W. Woodhead Publishing Series in Energy. Woodhead Publishing, 68–e2.
- Samikannu, S. M., Namani, R. and Subramaniam, S. K. (2016). 'Power enhancement of partially shaded PV arrays through shade dispersion using magic square configuration'. In: *Journal of Renewable and Sustainable Energy* vol. 8, no. 6, p. 063503.
- Shams El-Dein, M. Z., Kazerani, M. and Salama, M. M. A. (2013). 'An Optimal Total Cross Tied Interconnection for Reducing Mismatch Losses in Photovoltaic Arrays'. In: *IEEE Transactions on Sustainable Energy* vol. 4, no. 1, pp. 99–107.
- Summerer, L., Vasile, M., Biesbroek, R. and Ongaro, F. (2003). 'Space and Ground Based Large Scale Solar Power Plants - A European Perspective'. In:
- Teo, J., Tan, R. H., Mok, V., Ramachandaramurthy, V. K. and Tan, C. (2017). 'Effects of bypass diode configurations to the maximum power of photovoltaic module'. In: *Int. J. Smart Grids Energy* vol. 6, pp. 225–232.
- Wald, L. (2018). 'BASICS IN SOLAR RADIATION AT EARTH SURFACE'. working paper or preprint.

Bibliography

- Ziar, H., Mansourpour, S., Afjei, E. and Kazemi, M. (2012). 'Bypass diode characteristic effect on the behavior of solar PV array at shadow condition'. In: *2012 3rd Power Electronics and Drive Systems Technology (PEDSTC)*. IEEE, pp. 229–233.

APPENDIX B

Thesis II: Microcontroller

Salar Mollaie Daryani & Van Cong Nguyen

EE3L11 : Bachelor Thesis

Solar Drone: Maximum Power Point Tracker July, 2019

Group D: Micro controller

Authors:
Mohammad Salar Mollaie Daryani, 4410874
Van Cong Nguyen, 4452690

Supervisors :
Dr. P. van Duijsen
Dr. Olindo Isabella

Abstract

This thesis is written in context of the Bachelor Graduation Project. The objective of the project is to design a power system for the solar drone with a highest possible efficiency. The project is conducted in group of six Bachelors students (Electrical Engineering), divided into three subgroups: Solar cells, Micro controller and Converter. This thesis is from the subgroup micro controller and describes the research, design and prototyping of the maximum power point tracking algorithm on the micro controller.

The goal of this thesis is programming an efficient MPPT algorithm on the Arduino NANO based on the Atmega 380. The different algorithms will be discussed briefly in this thesis. The conceptual and schematic design of the solar drone can be found in this thesis. The Perturb & Observe and the Incremental Conductance algorithm are implemented and tested with the Solar Trainer module (a solar simulator) and twelve solar cells in series configuration under different irradiances. Both algorithms give a considerable good efficiency. The calibration of the sensors (current and voltage) with an error model is also discussed.

Preface

During the bachelor programme at the Technical University of Delft we have learned a lot as Electrical Engineering students. We were not alone over these years and we will never forget the technical and non-technical support of our professors. We would like to express our sincerest gratitude to *Dr. Peter van Duijsen*, our supervisor, for his guidance throughout the project and also to *Dr. Olindo Isabella*.

With special thanks to *Prof. Arno Smets* who has stimulated us to step in the solar energy field during his lectures.

We would also like to thank *Dr.ing. I.E. Lager* for the smooth organisation of the Bachelor graduation programme.

Furthermore, we would like to thank the assistants at the Solar Lab *Arturo Martinez Lopez* and *Juan Camilo Ortiz Lizcano* for their support.

Finally we would like to thank our colleagues: *Joey Gelderblom*, *Joris van Roessel*, *Dewwret Sitaldin* and *David de Best* for an enjoyable and productive collaboration.

Mohammad Salar Mollaie Daryani & Van Cong Nguyen
DELFT, June 2019

Contents

Abstract	i
Preface	ii
1 Introduction	1
2 Requirements	4
3 Design	5
4 Implementation and validation	8
4.1 Arduino NANO	8
4.2 Sensors	9
4.2.1 Voltage sensor	9
4.2.2 Current sensor	11
4.3 PWM Generator	11
4.4 Implementation of Algorithms	12
5 Calibration	14
5.1 Voltage sensor	14
5.2 Current sensor	19
6 Results	24
6.1 Solar Trainer	24
6.2 Twelve solar cells in series	26
7 Discussion and Conclusion	29
Bibliography	30
A Arduino NANO	32
B Solar simulators	33
B.1 SOLAR TRAINER	33
B.2 ST014 simulator	38
C Tables of the measurements	41
D Algorithm code	47

1 Introduction

Nowadays drones are very popular in many sectors. Think for example about Amazon that wants to use drones for delivering packages at your doorstep. The most important drawback is the limited flight time of the drone. This flight time can be extended with a solar module and to get the most power out of these systems, a maximum power point tracker is used. Below the different MPPT algorithms are discussed briefly.

State of the Art of MPPT algorithms

To get the most power out of the solar module, a solar charger tracker is used. More specifically the Maximum Power Point Tracking (MPPT). It monitors the I-V output of the solar module to obtain the maximum power point by controlling the duty cycle of the DC-DC converter.

There is a lot MPPT algorithms but the most popular are the hill Climbing algorithms, these include the Perturb and Observe method, and Incremental Conductance method. There is a lot research on these two algorithms to improve the efficiency [1][2][3].

The drawback of the hill climbing algorithms is that it cannot find the global maximum power point when the solar panels are affected by partially shading. The algorithms to find the GMPP are more complex than the hill climbing algorithms[4][5][6][7][8].

The Perturb and Observe (P&O)

The simplest MPPT method is the Perturb and Observe [9][10]. In the P&O method the perturbation is applied either in the reference voltage or in the reference current signal of the solar cell. To achieve MPP, the system operating point is changed by applying a small perturbation in reference signal. After each perturbation, the power output is measured. If the value of measured power is more than the previous value, then the perturbation in reference signal is continued in the same direction. At any point the new value of solar cell power is measured less than the previous one, then the perturbation is applied in the opposite direction. Figure 1 illustrates the flow chart and the behaviour of the P&O method.

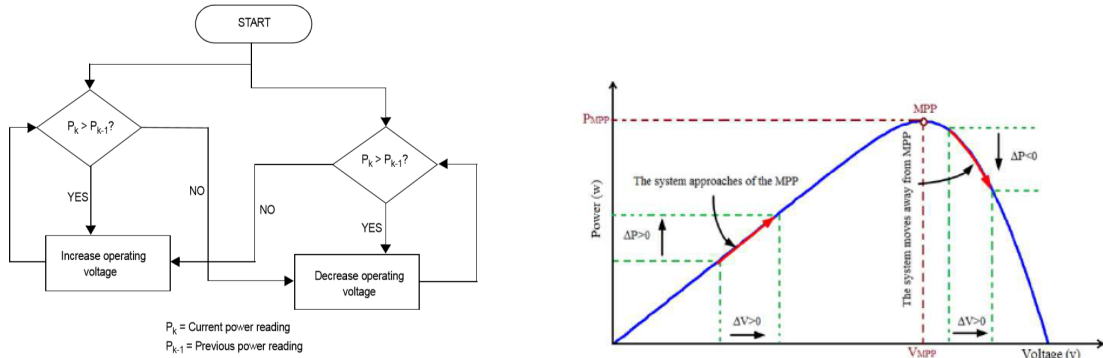


Figure 1: The flow chart and behaviour of P&O method [11][12].

This process will oscillate around the peak point. In order to reduce the oscillation, the perturbation size is kept very small. There is some power loss due to this perturbation and it also fails to track the power under fast varying atmospheric conditions [13].

The Incremental Conductance (IC)

The Incremental Conductance (IC) algorithm uses the fact that solar cell power curve derivative (or slope) versus voltage is 0 at MPP, positive on the left side and negative on the right side of the MPP. Applying the chain rule for the derivative of products of the power yields Equation 3

[11].

$$\frac{dP}{dV} = 0 \quad (1)$$

$$\frac{dP}{dV} = I + \frac{dI}{dV}V \quad (2)$$

$$\begin{cases} \frac{dI}{dV} = -\frac{I}{V} & \text{at MPP} \\ \frac{dI}{dV} > -\frac{I}{V} & \text{left of MPP} \\ \frac{dI}{dV} < -\frac{I}{V} & \text{right of MPP} \end{cases} \quad (3)$$

This algorithm has some advantages compared to the P&O. The IC can determine the MPP when it is achieved, but the P&O oscillates around the MPP. Also the Incremental Conductance can track rapidly increasing and decreasing irradiance conditions with higher accuracy than P&O [11]. Figure 2 shows the flowchart of the Incremental Conductance algorithm.

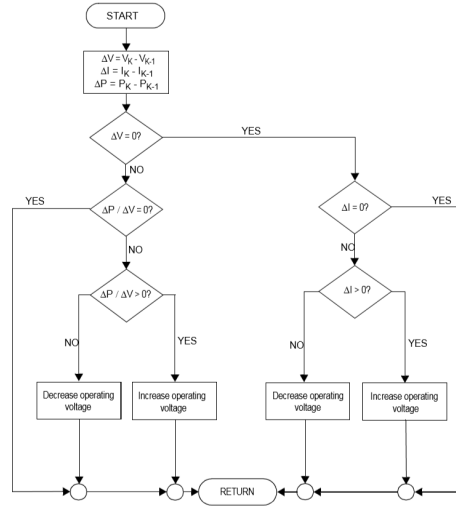


Figure 2: The flowchart of the IC algorithm [11].

Other methods

Other approaches are the fuzzy logic[14] and the neural network[15]. These techniques basically search for the maximum power point (MPP) within a local search space [16]. Being limited to a relatively small area means these approaches are suitable only for tracking the MPP under uniform insolation where only a single peak on the power–voltage (P–V) curve represents the output of the PV array. Under partially shaded or other nonuniform insolation conditions, multiple peaks may appear across the whole P–V curve [17]. The MPPT techniques, such as those mentioned above that are restricted to local search for the MPP, are able to identify only a peak but not the global peak that represents the Global Maximum Power Point (GMPP) [16]. Figure 3 illustrates the PV curves with multiple peaks.

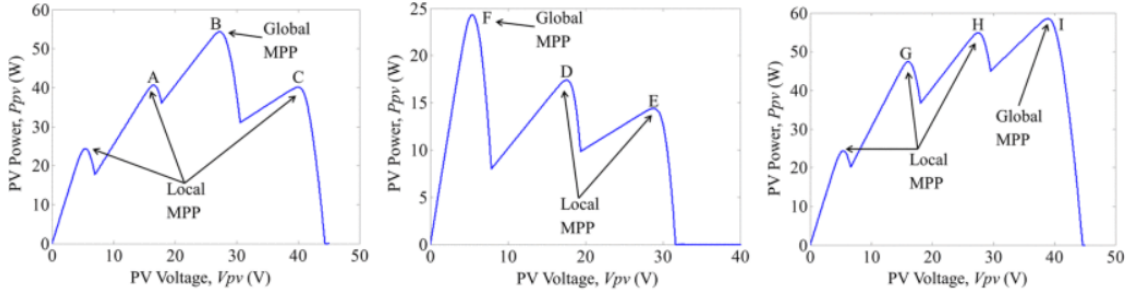


Figure 3: PV curves with the locals and global peaks [18].

The improved differential evolution (DE)

This method is based on the Differential Evolution. The Differential Evolution is an evolutionary algorithm that utilises target vectors as the population in each iteration [16]. The target vectors are equivalent to converter duty cycles, and the solutions obtained for each iteration are equivalent to the output power of the PV array. Increasing the size of the target vector will increase the search space, but the convergence speed will become slower. The target vector will undergoes in this algorithm random mutation if the change in power and duty cycle is above a threshold percentage. Multiple trial vectors is obtained for selection. The output power of the trial vectors is then obtained and the best value will be selected for next generation. This will go on until difference of the duty cycle and power output is smaller than the threshold. The best duty cycle is selected when the threshold is met [16].

When there is a change in solar intensity or load the algorithm can start over again. This algorithm is a good GMPPT with efficiency above 99% [16] but the implementation is relatively more complex in comparison to the hill climbing algorithms. More details about the algorithm and its method are explained in [16][19][20][21]. The proposed algorithm is depicted on figure 4.

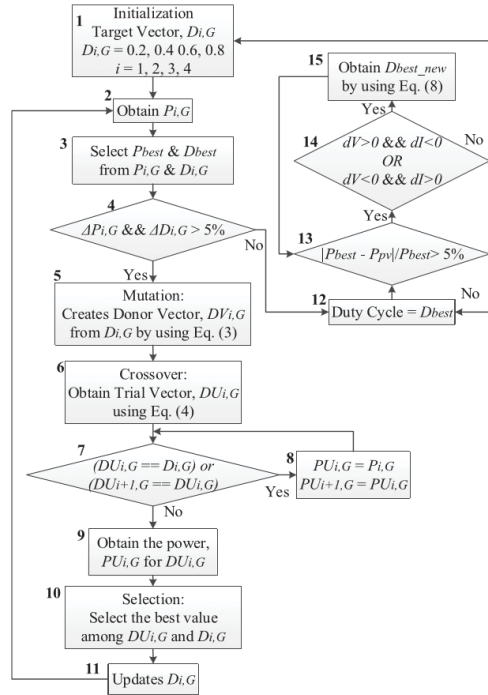


Figure 4: Improved Differential Evolution-Based MPPT Algorithm [16].

2 Requirements

This section determines the functional and non-functional requirements of the project. Functional requirements being requirements of what the system must do, and non-functional requirements being attributes that the system must have.

Non-Functional requirements

- The micro controller has to be as light as possible such that the drone can lift it.
- The power consumption of the micro controller must not affect the power consumption of drone.
- The micro controller has to be as small as possible to be boarded on the drone without affecting the aerodynamic of the drone.

Functional requirements

- The micro controller has to find the MPP of the solar module as efficient as possible.
- The output duty cycle of the micro controller has to be minimum at 50kHz to run the MOSFET of the converter properly.
- The duty cycle signal has to be higher than 4[V] to run the MOSFET of the converter properly.
- The micro controller has to measure the voltage and current of the solar module as accurate as possible to run the MPP algorithm properly.

Trade-off requirements The underneath trade-off have been considered during the project.

- Minimise the complexity of the micro controller and maximise the simplicity of programming such that the implementation of the algorithm becomes feasible for the sub-group.
- Supplying the micro controller by an independent battery than the battery of drone.
- Implementing of MPPT instead of a GMPPT.

3 Design

This section describes the conceptual design of the project. The Solar Drone project aims to increase the flight time of the drone by charging the battery during the flight via the mounted solar cells on the drone.

Conceptual design

To achieve the mentioned target, the Solar Drone group has been split into three sub groups. Mainly, the *Solar cells*, the *Micro Controller* and the *Converter*.

The main conceptual design of the Solar Drone project is illustrated on Figure 5.

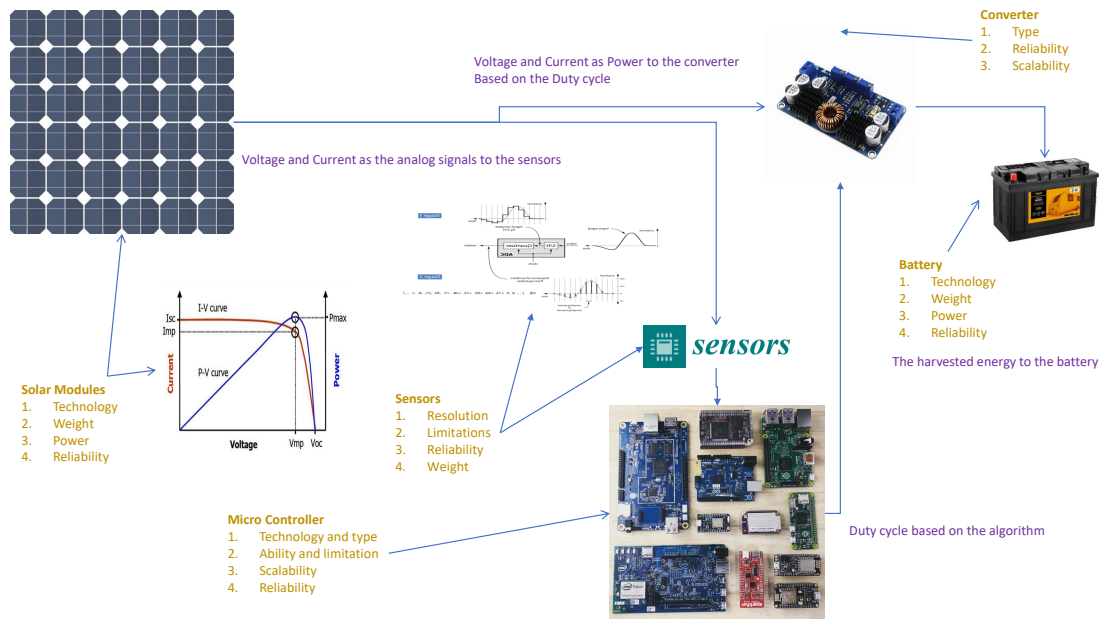


Figure 5: The main conceptual design of the project

Each module on the Figure 5 pointed to a specific sub group.

1. The solar module and the Battery are pointed to the *Solar cells* sub group.
2. The converter is pointed to the *Converter* sub group.
3. The Micro Controller and the sensors are pointed to the *Micro Controller* sub group.

Each sub group should consider the reliability, weights, technology, limitations, etc... of their sub modules into account.

The idea behind the conceptual design is that the solar module generates electrical energy and this energy should be stored to the battery as efficient as possible via the converter and the micro controller.

The task of the sub group *Micro Controller (MC)* is to maximise the output power of the solar cells. To achieve this, an MPPT algorithm has to be implemented on a micro controller. The micro controller measures the voltage and current of the solar module via sensors. The output of the micro controller is the duty cycle which has to be sent to the converter. Finally, the converter charges the battery.

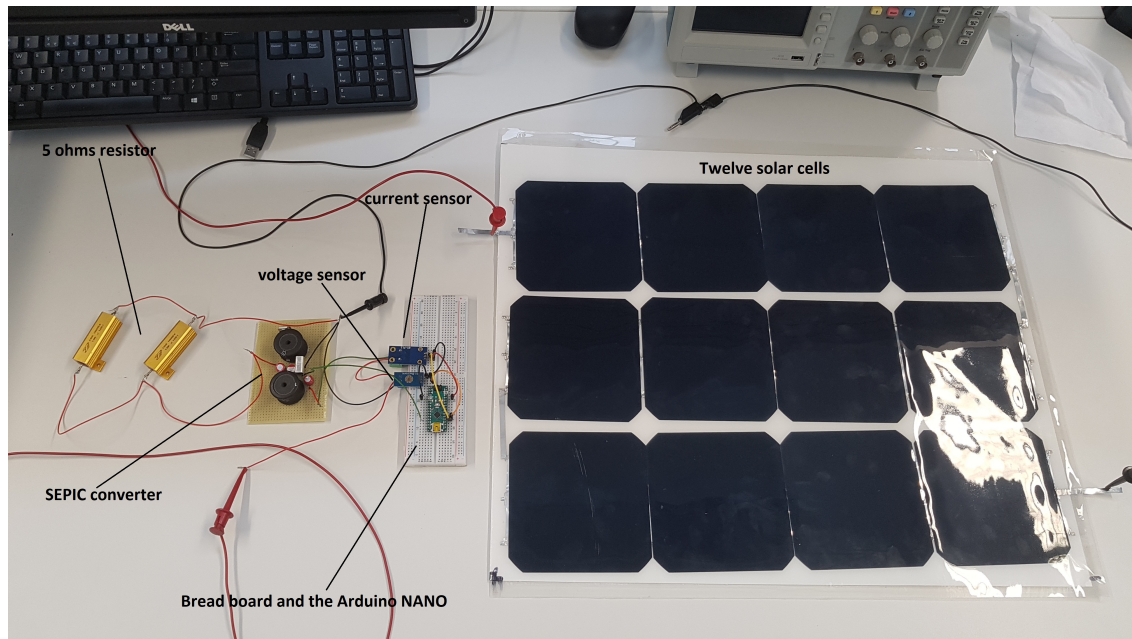


Figure 7: The bread board, Arduino, sensors, SEPIC converter, 5 ohms resistor and the twelve solar cells.

Table 1: The physical specifications of the micro controller

component	size [mm]	area [mm^2]	weight [g]
Arduino NANO	18 * 45	810	7
current sensor	18 * 35	630	4.3
voltage sensor	14 * 27	378	2.2
total		1818	13.5

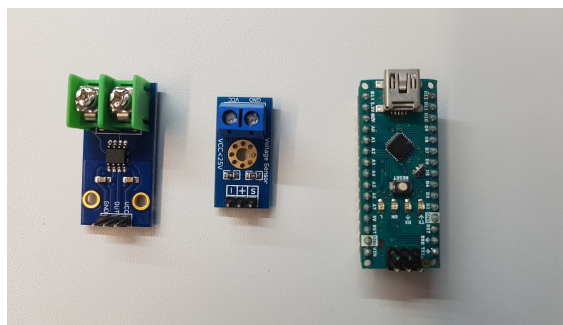


Figure 8: from left to right: current sensor, voltage sensor and Arduino NANO

4 Implementation and validation

This section describes all the designed and implemented subsystems of the subgroup *Micro Controller*. The *Micro Controller* consists of the Arduino NANO, sensors, PWM Generator and algorithms implementation.

4.1 Arduino NANO

There are different ways to program the MPP algorithm. One could use the micro controllers or even the micro processors. The Arduino NANO has been compared with the FPGA, Raspberry Pi and Olimex (see Appendix A). The Arduino NANO has been chosen since it is lighter and has lower power consumption but the most important factors are the simplicity of programming and big community. It also meets the requirements of the MOSFET from the subgroup *Converter*. This section explains the specifications of the Arduino NANO which have been used during the project.

Specifications

The Arduino NANO is based on the Atmega 328. Some specifications of this development board are tabulated on Table 2.

Table 2: Arduino NANO specifications

Clk frequency	ADC	Flash Memory	Operational voltage	Power consumption
16 MHz	10 bit	32KB	5-12 [V]	0.1 [W]

The Arduino NANO has 10 bit ADC's which can be used via 8 analogue pins, namely A0-A7 (see Figure 9).

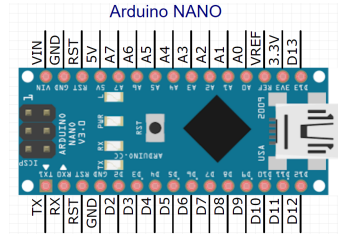


Figure 9: Arduino NANO and its pins

The Arduino NANO has 12 digital i/o's which can be used to assign the PWM signals (pins D2-D13).

The 5[V] output is assigned as a reference voltage for the sensors in this project. However, this value changes slightly if the operational voltage changes.

The Atmega 328 has 32KB Flash Memory and it was enough for implementing and running the algorithm properly.

The Arduino NANO can be programmed by different programming packages such as the Code Blocks and the computation environments like MATLAB but the Arduino IDE is used to program the algorithms. Arduino IDE is used as it is more convenient for programming. The codes can be uploaded into the Arduino via a mini USB jack available on its PCB.

Supplying the Arduino NANO

The Arduino NANO can be supplied by either its USB jack or either by the pin Vin on its PCB. Supplying via the USB is not a good choice for this project because the USB cable adds extra weights to the system. Therefore, the alternative method has been used.

Supplying the Arduino NANO can be done via the battery of the drone or via an independent battery. The rated voltage of the battery of the drone is about 11.4[V]. However, this value varies if the battery is fully charged (12.48[V]) or fully discharged. The 12.48[v] is harmful for the Arduino NANO, since it is higher than the maximum operating voltage of the Arduino.

A solution could be the use of a voltage regulator. However, decreasing or increasing of the input voltage of a voltage regulator can slightly vary the output voltage of the voltage regulator either. Moreover, the voltage regulator dissipates more energy as heat if the input and output voltage are close to each others. This situation could be happened if the team decides to use another battery for the drone with an operating voltage of 7.4[V] during the tests or demonstrations.

These deviation and drawback affect the functionality of the Arduino, especially on the voltage reference of the system. Consequently, the sensors do not work precisely as they are expected. In addition, the Arduino NANO is not able to run the total system as a charger, if the battery is discharged by the operating of the drone. Therefore, it has been decided to supply the Arduino NANO independently by a 9[V] battery pack. However, this choice results in 45 gr extra weights to the system. But this method is more reliable to supply the Arduino NANO and keeps its functionality constant. Figure 10 depicts the Arduino NANO's connection supplied by a 9[V] DC source.

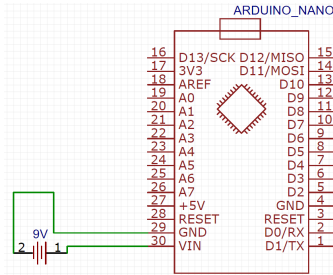


Figure 10: Arduino NANO supplied by a 9V DC battery

4.2 Sensors

The MPPT has to measure the output voltage and output current of the solar module to calculate the MPP. Two sensors have been used to measure the voltage and current as accurate as possible. These sensors are described and evaluated in this section.

4.2.1 Voltage sensor

The voltage sensor is nothing more than a voltage divider which is connected to the ADC of the Arduino NANO, namely pin A0. The ADC of the Arduino NANO are able to receive analogue signals up to 5[V]. This value is not suitable to measure the higher voltages than 5[V]. Therefore, two resistors are connected to each other as the Figure 11 to divide the voltages from the range of 0-25[V] into the range of 0-5[V] which is suitable for the ADC.

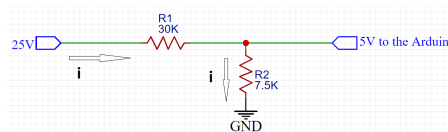


Figure 11: Voltage divider's schematic.

A simple calculation based on the KVL and KCL indicates that the R1 has to be 4 times bigger than the R2.

$$25 - i \cdot (R1 + R2) = 0 \quad (4)$$

$$i \cdot R2 = 5 \quad (5)$$

$$i \cdot R1 = 20 \quad (6)$$

$$\frac{R1}{R2} = \frac{20}{5} = 4 \quad (7)$$

The equation 7 proves that the R1 and R2 could be $30K\Omega$ and $7.5K\Omega$ respectively, as they are on the sensor. However, the measured value for R1 is $29.970K\Omega$ which has to be taken into account during the programming. The Figure 12 shows the connections between the Arduino and the voltage divider.

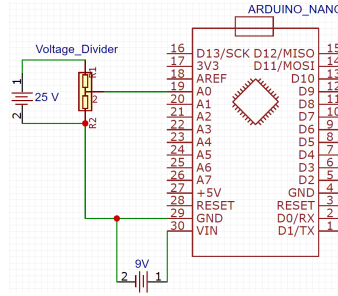


Figure 12: Arduino NANO connected to the voltage divider

Read voltage

The function `analogRead()` in the IDE reads the output of the 10 bit ADC of the Arduino. The value varies from 0 to 1023. The voltage can be measured by two steps.

1. Receive the analogue signal by `analogRead(A0)` and put it in to Equation 8, where the V_{ref} is the voltage reference which is $5[V]$ in this case.

$$v_{out} = \frac{analogRead(A0) * V_{ref}}{1023} \quad (8)$$

2. Put the result of Equation 8 in to Equation 9.

$$Voltage = \frac{v_{out}}{\frac{R2}{R1+R2}} \quad (9)$$

The Voltage gives the measured voltage by the Arduino NANO to the purposed algorithm. As it can be seen from Equation 8 and Equation 9, the Voltage is dependent on the V_{ref} and the resistances from the sensors. These values have been set and measured such that no offset voltage appears during the calculations.

The voltage sensor does not have any capacitance or inductance components. It has only two resistors. It is clear that the bandwidth of such sensor is infinite. However, the sensor has been tested by the signal generator with a sinusoidal signal up to 25MHz. The voltage divider does work under this condition and it divides the voltage as expected. So, it has an infinite bandwidth. The resolution of the voltage sensor is $4.883mV$ per A/D counts ($\frac{5}{1024} = 0.004883$).

4.2.2 Current sensor

The current sensor consists of the ACS712 which is based on the Hall effect and it is able to measure the currents up to 5 amps. Figure 13 shows this sensor and its connections to the Arduino.

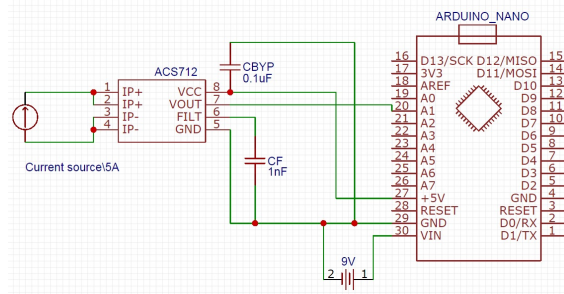


Figure 13: Arduino NANO with the connected current sensor

From the Figure 13 can be seen that the device is connected to a bypass capacitor (0.1 uF) via the pin VCC (5.0 [V]). This capacitor shorts the AC signals to ground, so that any AC noise that may be present on a DC signal is removed, producing a much cleaner and pure DC signal. The device is also connected to a capacitor (1 nF) via the FILTER pin. It has been recommended by the manufacturer to set the bandwidth of the device via this pin (FILTER) and this capacitor. The bandwidth of the sensor is 50KHz. The device should be connected in series configuration between the pins IP+ and IP- as it is depicted on the Figure 13.

Read current

To measure the current, the VIOUT of the sensor has to be connected to one of the ADC's of the Arduino NANO. The quiescent output voltage of the VIOUT is equal to $\frac{V_{CC}}{2}$ (according to the data-sheet). Therefore, using the function `analogRead()` gives us the value 511 if the V_{CC} equals to 5[V] and the current is zero in the pins IP+ and IP-. Reading the current follows the next steps:

Firstly, read the ADC by using `analogRead(A1)` and put it in to Equation 10, where the V_{ref} is the same as the V_{CC} in the design. The unit of the `voltage_hall` is volt.

$$voltage_hall = \frac{V_{ref}}{1023.0} * (analogRead(A1) - 511) \quad (10)$$

The next step is converting the received `voltage_hall` to the current. This step uses the sensitivity of the sensor which is given in the data-sheet. The given sensitivity for this sensor is $185 \frac{mV}{A}$. Hence, the next step is followed by Equation 11.

$$Current = \frac{voltage_hall}{0.185} \quad (11)$$

Since the current sensor senses the voltage of the hall effect, the resolution of this sensor is also $4.883mV$ per A/D counts.

4.3 PWM Generator

The PWM generator is implemented using a counter of the Atmega 328p. The counter has fast PWM mode that generate the PWM signal. The frequency of the PWM signal is calculated with Equation 12. With $f_{clk_I/O}$ the clock frequency of the Arduino NANO, 16 MHz; N the constant pre-scaling value: 1, 8, 64, 256, or 1024; and TOP the value which counter reset. The TOP value is stored in a match register of the counter.

$$f_{PWM} = \frac{f_{clk_I/O}}{N * (1 + TOP)} \quad (12)$$

The PWM signal is generated by comparing the counter value with the counter match registers. Two match registers are used to generate the PWM signal with certain frequency and duty cycle. One register is for setting the frequency and the other for the duty cycle. The resolution of the the counter is 8 bits which means that the counter maximum value is $2^8 - 1$ or 255, because the counter starts counting at zero, one is subtracted. This is also the reason why in Equation 12 one is added to the TOP value. For example PWM signal with frequency of 100kHz and a duty cycle of 10% is programmed by setting the two match registers to 159 and 15 respectively. The PWM signal can be validated by connecting the Arduino to the oscilloscope. This is done with different frequencies and duty cycles. In Figure 14 an example of PWM signal of 100 kHz with duty cycle of 50% can be seen.

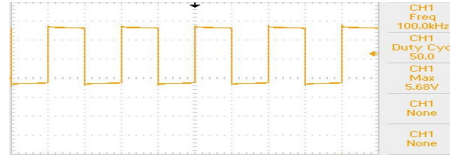


Figure 14: PWM signal of 100 kHz with duty cycle of 50%

The resolution of the duty cycle of the PWM can be calculated using Equation 13.

$$R_{PWM} = \frac{1}{TOP + 1} \quad (13)$$

Thus for 100 kHz PWM signal the resolution of the duty cycle is 0.00625 or 0.625%.

sampling frequency

The sampling frequency to measure the required voltage and current is chosen depending on the transient response of the converter. The transient response of the SEPIC converter, result out the simulation is around 5 ms. A buffer of 5 ms is taken, this result in a sampling period of 10 ms between two measurements and corresponds to 100 Hz.

The sampling frequency is implemented using the counter interrupt of the Atmega 328p. When the counter matches the value of the match register the interrupt function will be executed.

This is validated by toggling a output pin every time the interrupt occurs. This give a frequency of 50 kHz. This also can be validated with the oscilloscope. On the oscilloscope the frequency of the toggled signal is 49.9 kHz.

Another method is using the built in delay function to wait for 10 ms to measure the voltage and the current when changing the duty cycle.

4.4 Implementation of Algorithms

This section discusses how the algorithms are implemented on the micro controller. The P&O and IC have been chosen to be implemented on the micro controller. Both algorithms are relatively simple to implement. The P%O is chosen for its robustness and the IC because of its fast tracking under varying irradiance.

The two algorithms are programmed in their own function and called every interrupt period. In the interrupt function switch statement is used to choose between P&O or IC.

P&O

The P&O function decides in an *if statement* which direction the duty cycle has to be set every sampling period. The duty cycle is then set using the function *setDuty* with input parameter the amount of steps you want to increase or decrease.

IC

The IC function also decides in an *if statement* which direction the duty cycle has to be set every sampling period. In the hardware implementation $\frac{dP}{dV} = 0$, where the slope is zero, almost never occurs so it is approximated with Equation 14 [3].

$$\begin{cases} |\frac{\Delta I}{\Delta V} + \frac{I}{V}| \leq error & \text{at MPP} \\ \frac{\Delta I}{\Delta V} + \frac{I}{V} > error & \text{left of MPP} \\ \frac{\Delta I}{\Delta V} + \frac{I}{V} < -error & \text{right of MPP} \end{cases} \quad (14)$$

The error term in Equation 14 is decided on the basis of trail-and-error.

DE

The DE algorithm is already implemented but need debugging, and because lack of time and the solar cells are going to be put in series on the drone there is no need for a GMPPT.

Variable step size

By increasing the step size of the duty cycle every sampling period while the operation point is on the left side the P-V curve, where the slope is positive, until operation point reaches the left side of the P-V curve, where the slope is negative. Then the operation point returns to left side of the P-V and set the step size back to initial step size. This process starts over again until it reaches the MPP. This is done by defining a variable that buffers the previous step size. The implementation need only a variable that buffer the step size. This variable is *count* in the code see Appendix D

5 Calibration

This section describes the methods which have been used to calibrate the functionality of the sub components. It considers the sensors.

The sensors (the voltage and current) were not able to measure the voltage and current as accurate as needed. This problem was observed during the first test of the sensors. The tests have been performed using the available power supply at the Tellegen Hall which is able to supply voltages and currents up to 20[V] and 5[A] respectively. A multimeter has been used to measure the real voltages and currents during the tests.

To tackle with the inaccuracy of the sensors, some statistic methods have been considered to improve the proposed functionality of the sensors. The next two subsections explain the mentioned methods.

5.1 Voltage sensor

To test the voltage sensor, the sensor was connected to the power supply and the voltmeter in parallel configuration. The output of the sensor was being detected by the Arduino. The *real voltages* are the voltages from the voltmeter and the *measured voltages* are from the Arduino.

Reading the voltage

The first observations from the Arduino by the sensors showed that the measured voltages keep oscillating around the expected value. This behaviour affects the functionality of the implemented algorithm. Therefore, the *ResponsiveAnalogRead* library added to the IDE of the Arduino NANO. The function *analog.getValue()* from the mentioned library read the values from the ADC of the Arduino NANO and gives the most reliable value from the ADC. Therefore, Equation 8 changes to Equation 15.

$$v_{out} = \frac{\text{analog.getValue}(A0) \cdot V_{ref}}{1023} \quad (15)$$

After using Equation 15, the Arduino measured the voltages without oscillating of the values. However, during the test of the micro controller together with the converter, this problem observed again. It was because the proposed converter did not have an input capacitor. This shortcoming caused fluctuations of the voltages. The *Converter* group added a capacitor at the input of the converter to solve the problem. Figure 15 and 16 show the oscillating of the voltages before and after of adding the input capacitor.

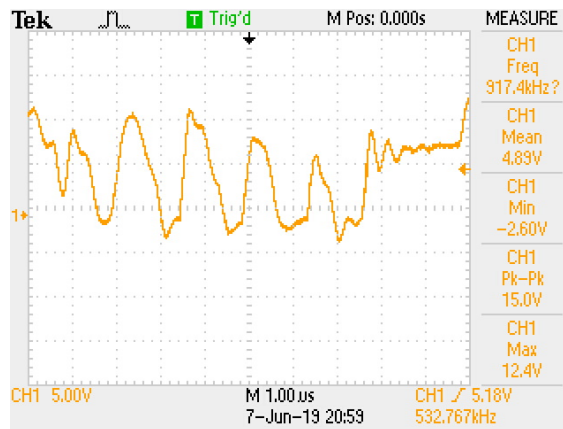


Figure 15: The input voltage of the converter without the capacitor



Figure 16: The input voltage of the converter with the capacitor

Evaluation of error

Figure 17 shows the real and measured voltages by the voltmeter and Arduino and the evaluated error in a box plot. Table 3 gives the values of the box plot.

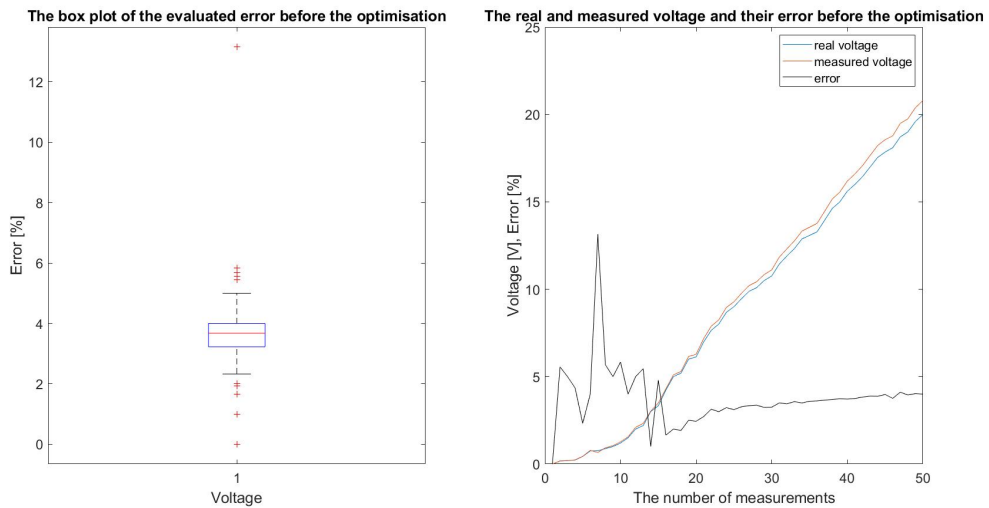


Figure 17: The real and measured voltage (right_hand side) and the evaluated error before the calibration.(see Appendix C and Table 24).

Table 3: The box plot values before the calibration

total observation	50
minimum	0
maximum	13.1579
25th percentile	3.2258
median	3.6747
75th percentile	4
lower adjacent	2.3258
upper adjacent	5
total outliers	10

From the Figure 17 can be observed that the real voltage and measured voltage by the sensor deviates from each other. The yellow line from Figure 17 gives that the evaluated errors at the lower voltages are more inaccurate than the higher voltages. The adjacent bounds (2.33-5%) from the box plot indicate the evaluated errors for the 95% confidence interval. The bounds have to be decreased to accurate the sensor.

To decrease the error, a regression line has been calculated with the help of *cftool* from the *MATLAB*. Figure 18 shows the regression line which is calculated by the real and measured voltages.

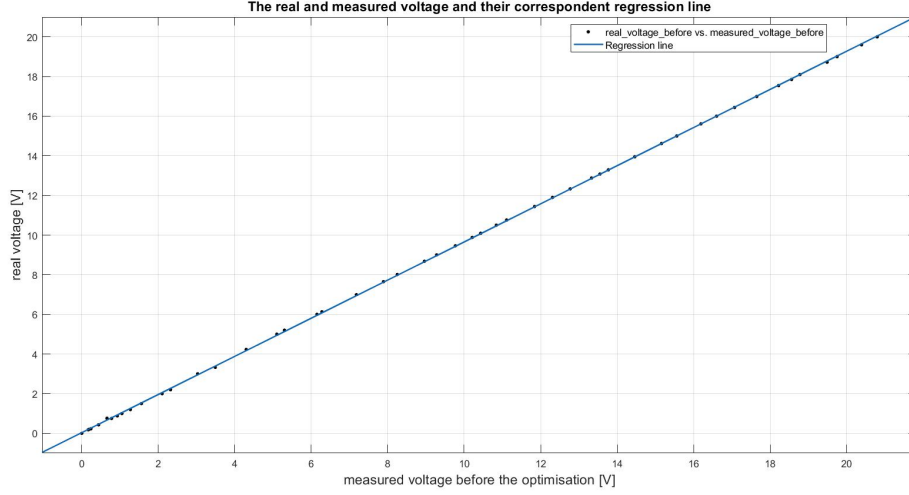


Figure 18: The regression line for the real and measured voltages.

The Equation 16 gives the correspondent function of the proposed regression line, where the x is the measured voltage and the $f(x)$ is the real value. Table 4 gives the coefficients of the Equation 16.

$$f(x) = p_1 \cdot x + p_2 \quad (16)$$

Table 4: The coefficients of the equation 16.

Coefficient	value	95% confidence bounds
p_1	0.9619	(0.9602, 0.9636)
p_2	0.03481	(0.01554, 0.05407)

The Equation 16 has been added to Equation 9 and results in Equation 17.

$$Voltage = \frac{v_{out}}{\frac{R_2}{R_1+R_2}} * 0.9619 + 0.03481 \quad (17)$$

Applying the Equation 17 decreases the evaluated errors by the sensor significantly as it depicted on Figure 19.

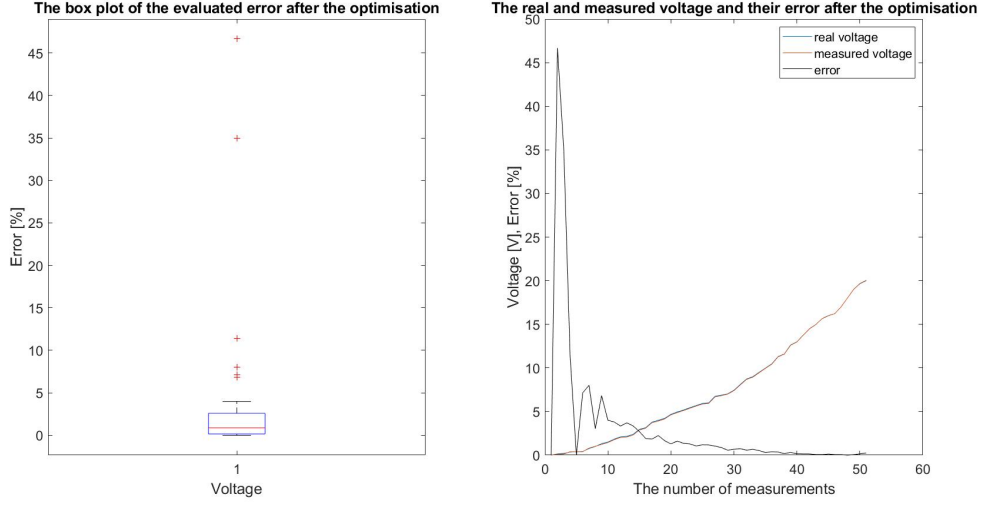


Figure 19: The real and measured voltage (right_hand side) and the evaluated error after the calibration.

Table 5 gives the values of the box plot.

Table 5: The box plot values after the calibration

total observation	51
minimum	0
maximum	46.667
25th percentile	0.15845
median	0.87209
75th percentile	2.5895
lower adjacent	0
upper adjacent	4
total outliers	6

From the Table 3 and Table 5 can be seen that the median, 25th percentile, 75th percentile and adjacent bounds have been decreased significantly. These changes are also more obvious at the higher voltages on the Figure 19.

Although the maximum error from the Figure 19 increased dramatically compared to the maximum error from the Figure 17, this error is out of the 95% confidence interval of the evaluated errors. Moreover, the operating voltage of the converter should be minimum 1.2[V] to operate the converter properly. Therefore, this error is not considered to evaluate the Equation 17.

Error model

The Equation 17 decreases the inaccuracy of the voltage sensor. However, this model has its own error.

To justify the final result of the sensor, an error model has been calculated. Figure 20 shows the evaluated errors vs the measured voltages and the correspondent regression line after the calibration.

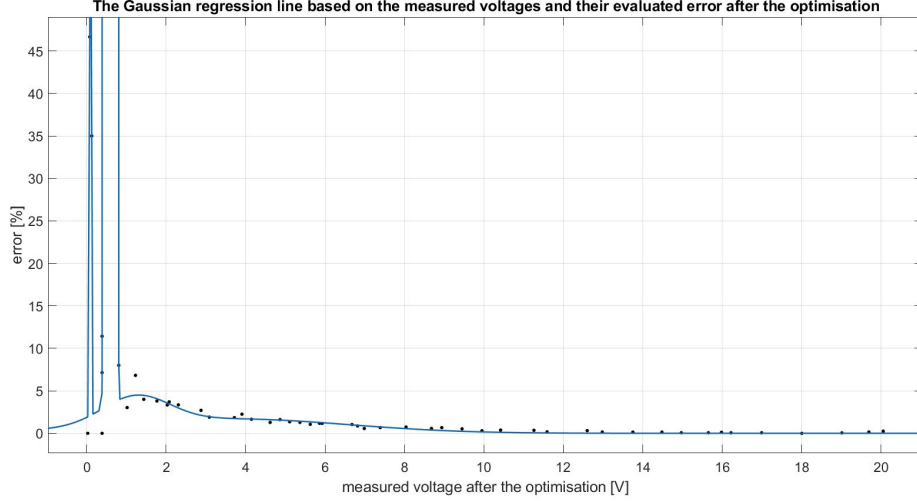


Figure 20: The evaluated errors vs the measured voltages and the correspondent regression line after the calibration

The Equation 18 and Table 6 give the regression line and the correspondent coefficients respectively, where the x is the measured voltage and the $f(x)$ is the evaluated error. The Equation 18 is based on the Gaussian curve fitting with 4 terms. It is because the other curve fittings available in the *cftool* did not cover all the evaluated error properly. However, this model is not suitable for the voltages higher than 9 [V]. Since it indicates the lower errors than usual.

$$f(x) = a_1 \cdot \exp\left(-\frac{x - b_1}{c_1}\right)^2 + a_2 \cdot \exp\left(-\frac{x - b_2}{c_2}\right)^2 + a_3 \cdot \exp\left(-\frac{x - b_3}{c_3}\right)^2 + a_4 \cdot \exp\left(-\frac{x - b_4}{c_4}\right)^2 \quad (18)$$

Table 6: The correspondent coefficients of the equation 18.

Coefficient	value	95% confidence bounds
a_1	267.3	(-2.23e+07, 2.23e+07)
b_1	0.104	(-42.41, 42.62)
c_1	0.01794	(-386.2, 386.2)
a_2	3.5e+08	(-4.838e+23, 4.838e+23)
b_2	0.6006	(-4.364e+10, 4.364e+10)
c_2	0.049	(-1.843e+12, 1.843e+12)
a_3	3.285	(-3.924, 10.49)
b_3	1.242	(-0.3573, 2.842)
c_3	1.184	(-1.71, 4.078)
a_4	1.696	(-0.46, 3.852)
b_4	3.654	(-7.931, 15.24)
c_4	4.134	(-6.605, 14.87)

To have a better error model, the measured voltages higher than 1[V] have been considered to calculate the regression line. Since the converter does not work under 1.2[V]. Moreover, the Solar Trainer (see Appendix B) works in higher voltages around 15-22 [V].

Figure 21 shows the correspondent regression line.

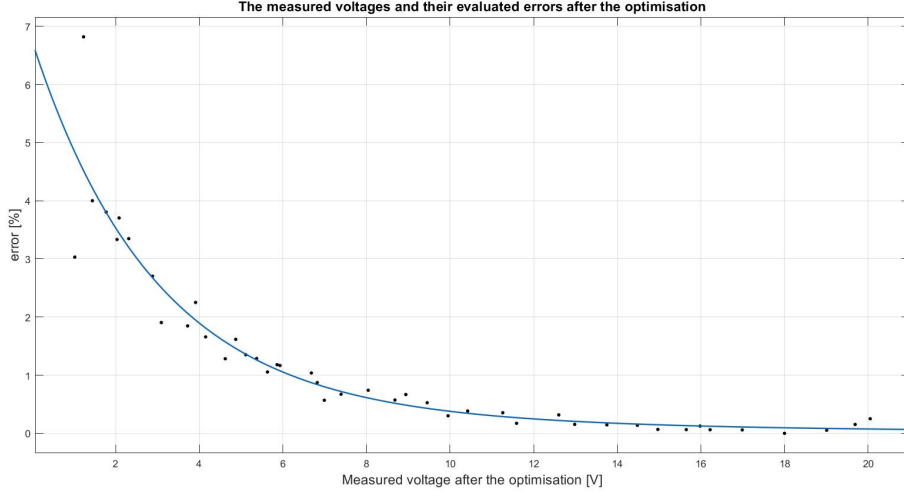


Figure 21: The evaluated errors vs the measured voltages and the correspondent regression line after the calibration for the range of 1-20[V].

Equation 19 describes the regression line, where the x is the measured voltage and the $f(x)$ is the error. Table 7 gives the coefficients.

$$f(x) = a * \exp(b * x) + c * \exp(d * x) \quad (19)$$

Table 7: The correspondent coefficients of the equation 19.

Coefficient	value	95% confidence bounds
a	6.257	(-0.46, 12.97)
b	-0.3461	(-0.7587, 0.06662)
c	0.4843	(-7.414, 8.383)
d	-0.09803	(-1.101, 0.9045)

5.2 Current sensor

To test the current sensor, the sensor was connected to the power supply and the ammeter in series configuration. The *real currents* are the currents from the ammeter and the *measured currents* are from the Arduino.

Reading the current

The current sensor reads the ADC of the Arduino NANO with the `analog.getValue()` function available at the `ResponsiveAnalogRead library`. This function protects the implemented algorithm from the oscillation of the measured currents by the ADC. Hence, the Equation 10 changes to Equation 20.

$$voltage_hall = \frac{V_{ref}}{1023.0} * (analog.getValue(A1) - 511) \quad (20)$$

Evaluation of error

Figure 22 illustrates the real and measured currents and the evaluated errors before the calibration.

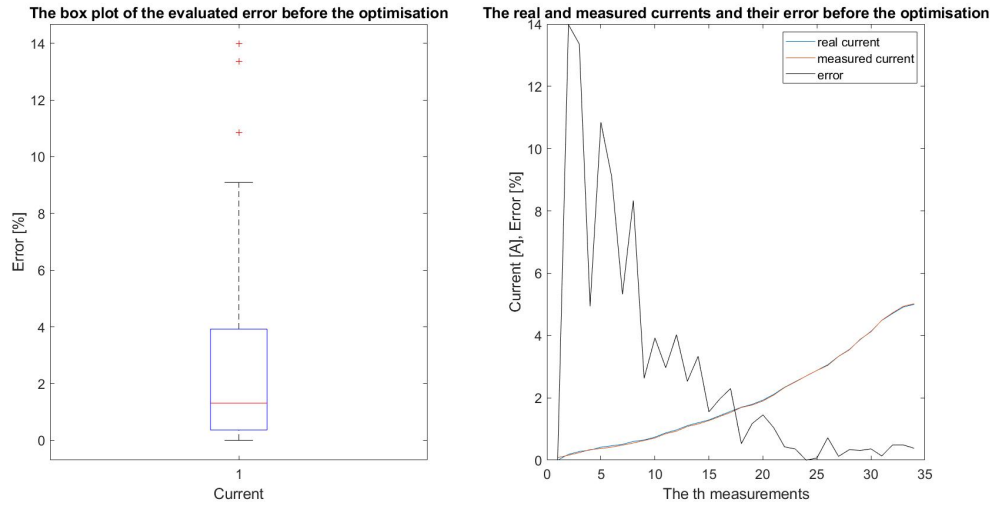


Figure 22: The real and measured currents (right_hand side) and the evaluated error before the calibration.(see Appendix C Table 25)

From the Figure 22 can be seen that the higher currents result in lower errors. Table 8 gives the correspondent values of the box plot.

Table 8: The box plot values before the calibration

total observation	34
minimum	0
maximum	13.9785
25th percentile	0.36276
median	1.3124
75th percentile	3.9242
lower adjacent	0
upper adjacent	9.0909
total outliers	3

To decrease the error, the regression line for the real and measured voltages has been calculated. Figure 23 illustrates the regression line.

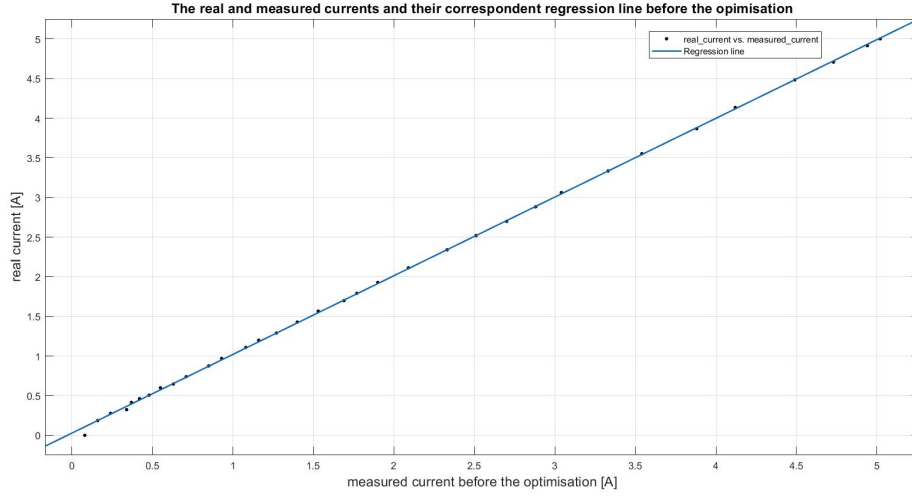


Figure 23: The real and measured currents and the regression line before the calibration.

The regression line is calculated by the Equation 21, where the x is the measured current and the $f(x)$ is the real current. Table 9 gives the coefficients of the Equation 21.

$$f(x) = p_1 * x + p_2 \quad (21)$$

Table 9: The correspondent coefficients of the Equation 21.

Coefficient	value	95% confidence bounds
p_1	0.9927	(0.9873, 0.9982)
p_2	0.02798	(0.01435, 0.04161)

The current has to be measured by the Arduino by the Equation 22

$$Current = \frac{voltage_hall}{0.185} * 0.9927 + 0.02798 \quad (22)$$

Applying the Equation 22 in to the Arduino results in Figure 24.

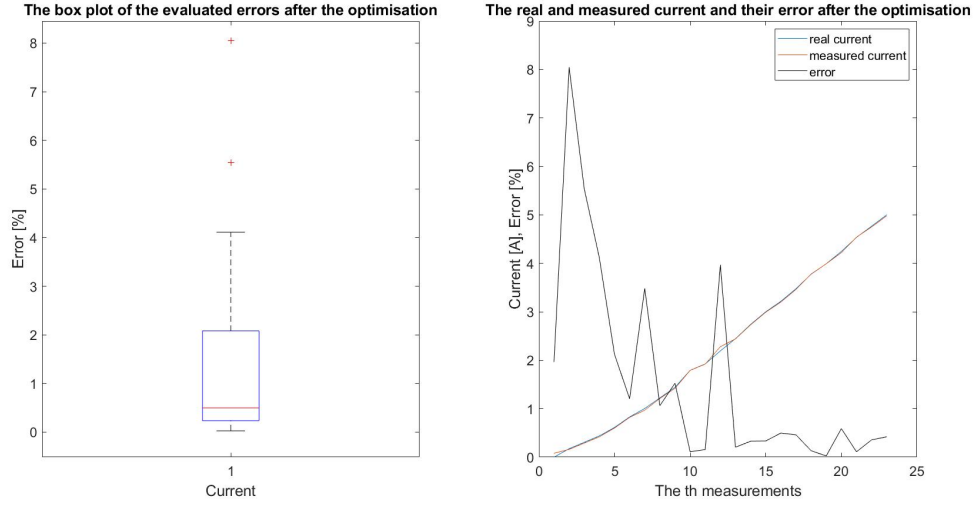


Figure 24: The real and measured currents (right_hand side) and the evaluated error after the calibration.(see Appendix C Table 25)

Table 10: The box plot values after the calibration

total observation	23
minimum	0.025056
maximum	8.046
25th percentile	0.23552
median	0.49751
75th percentile	2.0813
lower adjacent	0.025056
upper adjacent	4.1096
total outliers	2

Table 10 gives the values of the box plot from Figure 24. Comparison between the Table 8 and Table 10 proves that the error parameters have been decreased significantly.

Error model

The evaluated error after the calibration based on the measured current is depicted on Figure 25.

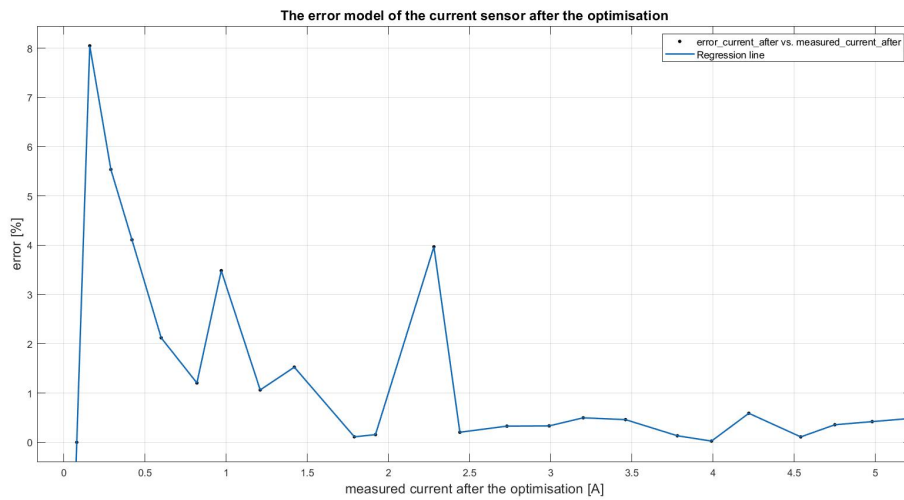


Figure 25: The evaluated errors vs the measured voltages and the correspondent regression line after the calibration

Figure 25 and its correspondent values from Table 25 are used to justify the total errors of the measurements. A mathematical error model for the current sensor has not been calculated because the regression line could not cover the evaluated errors properly. Hence, the Table 25 is used to find a proper error.

6 Results

The algorithms are tested with two setups: The Solar Trainer module, a solar cell simulator; and the same solar cells used for the drone, 12 in series. And The average efficiency is taken form 10 samples.

6.1 Solar Trainer

To validate the algorithm the Solar Trainer IV and PV curve have to be known, this can be done by connecting a variable load to the Solar Trainer and measuring the voltage and current with the multimeter. The Solar Trainer has three different irradiances level by changing the short circuit current. The short circuits are the 0.4, 0.8 and 1.2 [A]. In Figure 26 the IV and PV curves for the three different irradiances level are plotted.

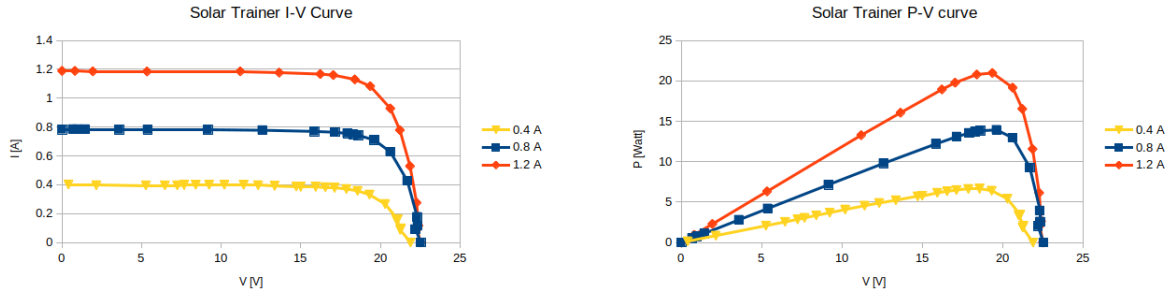


Figure 26: The I-V and P-V Curve of the Solar Trainer

In Table 11 the Maximum power point of the three irradiance level can be found.

Table 11: Maximum power point of the Solar Trainer

$I_{sc}[A]$	$I_{max}[A]$	$V_{max}[V]$	$P_{max}[Watt]$
0.4	0.358	17.9	6.6
0.8	0.764	19.6	13.9
1.2	1.083	19.4	21

Figure 27 shows the Solar Trainer during the tests.

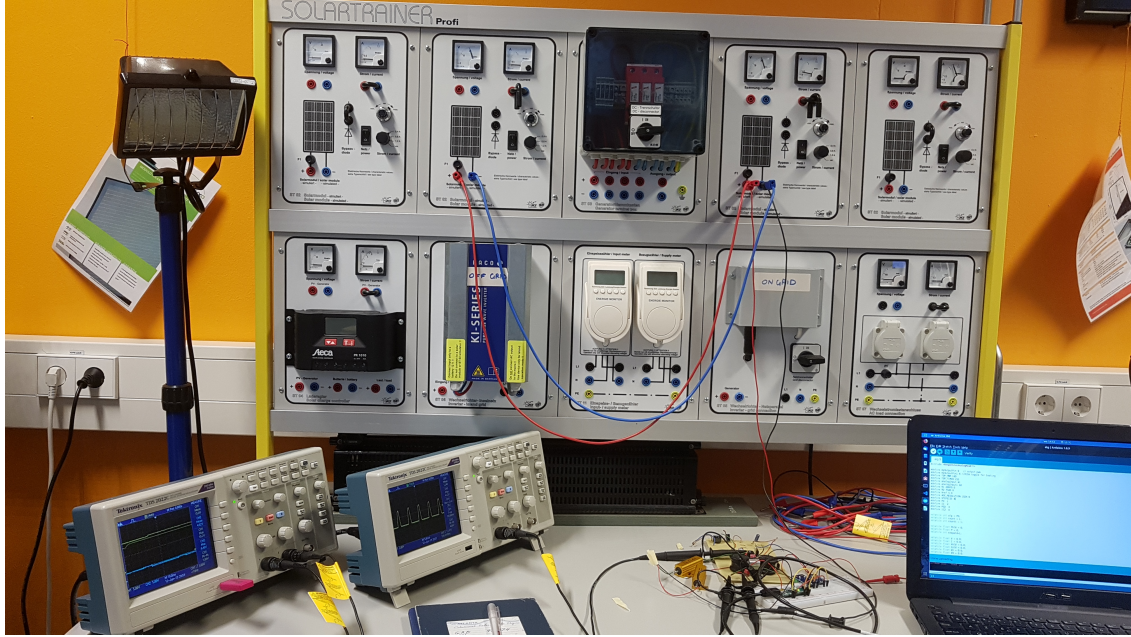


Figure 27: The Solar Trainer during the test

P&O algorithm

The P&O algorithm is validated with the SEPIC converter with a load of five ohms at the output. The step size of the duty cycle is 0.625%.

Table 12: Results of the P&O algorithm with SEPIC converter and step size of 0.625%. The η_{av} is efficiency.

$I_{sc}[A]$	Duty cycle oscillation	I[A]	V[V]	P[W] oscillation	$\eta_{av}\%$
0.4	0.21-0.26	0.40	18.85-19.86	7.45-7.85	117
0.8	0.27-0.29	0.66	19.23-19.89	13.30-13.75	93
1.2	0.29-0.31	0.95	19.9-20.33	19.17-19.52	91

In Table 12 for $I_{sc} = 0.4$ the MPP measured with P&O is higher than the MPP measured with the multimeter and variable load. This efficiency is not logic and is discussed in the next paragraph.

Evaluated error

The measured voltages and currents available in Table 12 have their own error which has been discussed in section 5. Using the error models of the voltage and current sensors (Equation 19 and Table 25) give the errors of the measured values. Table 13 gives the results of the P&O algorithm together with the evaluated errors.

Table 13: Results of the P&O algorithm and their evaluated errors

I [A]	error [%]	V [V]	error [%]	total error [%]	P [W]
0.4	4.11	18.85 - 19.86	0.08 - 0.09	4.2	$(7.45 - 7.85) + \sqrt{-0.3}$
0.66	2.12	19.23 - 19.89	0.09	2.21	$(13.30 - 13.75) + \sqrt{-0.3}$
0.95	3.48	19.9 - 20.33	0.07	3.55	$(19.17 - 19.52) + \sqrt{-0.7}$

From Table 13 can be seen that adding the errors to the calculated powers results in a closer value

to the maximum powers from the Table 11, except for the first row of the mentioned tables. For the first row, the error should be subtracted from the calculated power. However, the calculated power is still higher than the maximum power (6.6[W]). It could be because of a human mistake during the test or a non-calibrated multimeter or the Solar Trainer.

Also this inaccuracy could be from the current sensor which is not able to measure the currents as accurate as needed at low currents (see Figure 24). Although, the built-in ammeter of the Solar Trainer at the $I_{sc} = 0.4$ mode gave the values as the sensor detected .

IC algorithm

The IC algorithm is also validated with the SEPIC converter with a load of five ohms at the output. The step size is also 0.625%.

Table 14: Result of the IC algorithm with the SEPIC converter and step size of 0.625%

$I_{sc}[A]$	Duty cycle	I[A]	V[V]	P[W]	$\eta_{av}\%$
0.4	0.25	0.40	15.87	6.27 \pm 0.3	90
0.8	0.27	0.58	21.08	12.18 \pm 0.3	88
1.2	0.32	0.95	19.93	18.84 \pm 0.7	91

From the measurement it can be seen that the IC has lower efficiency than P&O but it does not oscillate as the P&O does. The evaluated error has been calculated as the Table 13.

6.2 Twelve solar cells in series

The algorithms are also validated with twelve solar cells in series. These solar cells will be eventually be mounted on the drone. The setup is the same as the Solar Trainer only with the real solar cells.

To know the MPP of the twelve solar cells in series a duty cycle sweep from 25% to 85% with step size of 0.6% is performed by the Arduino. This is done with two irradiance level : 530 and 900 $W.m^{-2}$. The duty cycle operation range of the SEPIC converter is between 25% and 85%. The MPP for two irradiance level can be seen in Table 15. The full duty cycle sweep can be found in Appendix C.

Table 15: MPP for twelfth solar cells in series

Irradiance[$W.m^{-2}$]	Duty cycle	V[V]	I[A]	P[W]
530	0.63	4.40	1.39	6.11
900	0.67	4.61	2.02	9.50

Figure 28 shows the twelve solar cells during the tests.

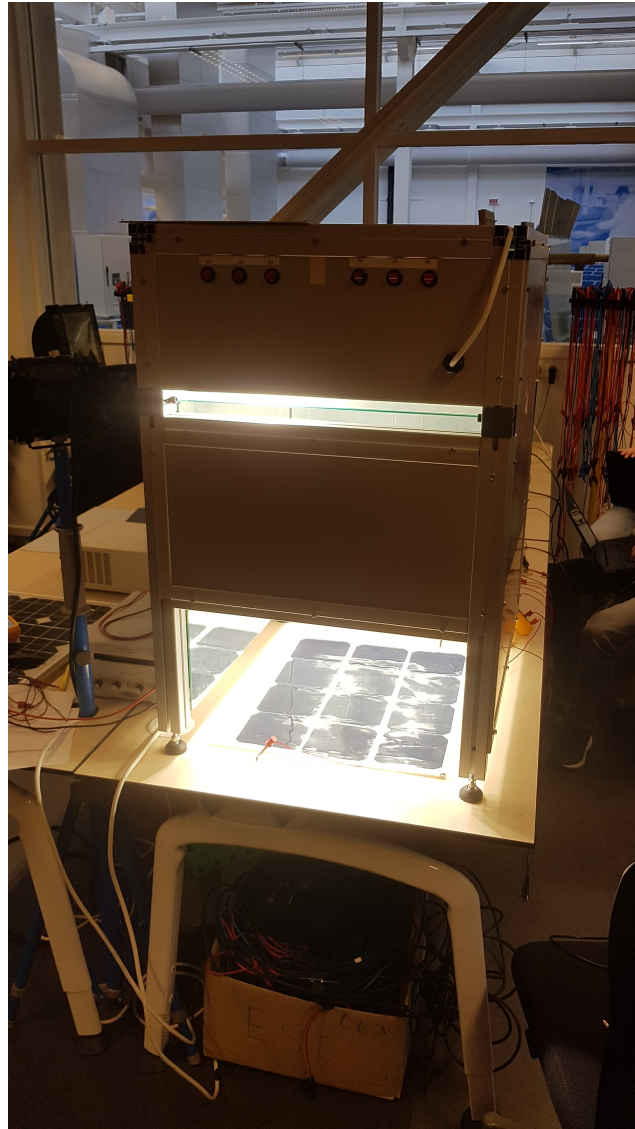


Figure 28: The twelve solar cells under test

P&O algorithm

The result of the P&O algorithm with the twelve solar cells is tabulated in Table 16.

Table 16: Result of the P&O algorithm with SEPIC converter and step size of 0.625%

Irradiance [$W.m^{-2}$]	Duty cycle	I [A]	V [V]	P [W]	η_{av} %
530	0.61-0.66	1.29-1.50	3.34-4.42	(5-5.83) \pm 0.2	89
900	0.65-0.71	1.99-2.47	3.53-4.61	(8.61-9.50) \pm 0.2	91

IC algorithm

The result of the IC algorithm by the twelve solar cells is tabulated in Table 17.

Table 17: Result of the IC algorithm with SEPIC converter and step size of 0.625%

Irradiance [$W.m^{-2}$]	Duty cycle	I [A]	V [V]	P [W]	η_{av} %
530	0.56	1.08	5.01	5.39 +/- 0.3	88
900	0.63	1.91	4.87	9.32 +/- 0.3	98

As can be seen from above the P&O and IC algorithm perform very well. The drawback of the P&O method is that the power oscillates around the MPP while IC locks on a power. The tricky part of the IC method is to find the right error value. If the error value is too high it will lock on the wrong power and if the error value is too low it keeps searching for the MPP. And for every PV system the error value is different so it has to be modified.

Variable step size

This is tested for both algorithm and gives the same result as the fixed step size version but only converges faster to the MPP.

7 Discussion and Conclusion

The P&O and IC have been implemented on the Arduino NANO properly. They can find the MPP of the solar module under different solar irradiances. However, the DE algorithm was not tested since the Solar Drone group decided to have the solar module in series configuration.

The Arduino runs the MOSFET of the converter properly.

The calibration model of the sensors helped the micro controller to measure the voltages and currents more accurate. However, choosing another micro controller with a higher ADC resolution could have been improved the system to determine the MPPT or GMPPT more precisely.

The P&O and IC methods have a considerable good efficiency and can be used to for the solar drone. The IC method oscillates less than the P&O but has to be tuned for different setups, the error term in Equation 14 and step size need to be tuned.

We prefer the P&O method to the IC method because of its robustness. Also it does not need to be tuned. The speed of the P&O method can be increased using a variable step.

Bibliography

- [1] M. Nasir and M. F. Zia. Global maximum power point tracking algorithm for photovoltaic systems under partial shading conditions. In *2014 16th International Power Electronics and Motion Control Conference and Exposition*, pages 667–672, Sep. 2014.
- [2] E. M. Ahmed and M. Shoyama. Variable step size maximum power point tracker using a single variable for stand-alone battery storage pv systems. *Power Electronics*, 11(2):218–227, Mar. 2011.
- [3] A. Safari and S. Mekhilef. Simulation and hardware implementation of incremental conductance mppt with direct control method using cuk converter. *IEEE Transactions on Industrial Electronics*, 58(4):1154–1161, April 2011.
- [4] E. Koutroulis and F. Blaabjerg. A new technique for tracking the global maximum power point of pv arrays operating under partialshading conditions. *IEEE J. Photovolt*, 2(2):184–190, Apr 2012.
- [5] T. L. Nguyen and K. Low. A global maximum power point tracking scheme employing direct search algorithm for photovoltaic systems. *IEEE Transactions on Industrial Electronics*, 57(10):3456–3467, Oct 2010.
- [6] Y. Ji, D. Jung, J. Kim, J. Kim, T. Lee, and C. Won. A real maximum power point tracking method for mismatching compensation in pv array under partially shaded conditions. *IEEE Transactions on Power Electronics*, 26(4):1001–1009, April 2011.
- [7] H. Renaudineau, F. Donatantonio, J. Fontchastagner, G. Petrone, G. Spagnuolo, J. Martin, and S. Pierfederici. A pso-based global mppt technique for distributed pv power generation. *IEEE Transactions on Industrial Electronics*, 62(2):1047–1058, Feb 2015.
- [8] K. Ishaque and Z. Salam. A deterministic particle swarm optimization maximum power point tracker for photovoltaic system under partial shading condition. *IEEE Transactions on Industrial Electronics*, 60(8):3195–3206, Aug 2013.
- [9] S. Kolesnik and A. Kuperman. On the equivalence of major variable-step-size mppt algorithms. *IEEE Journal of Photovoltaics*, 6(2):590–594, March 2016.
- [10] J. Ahmed and Z. Salam. A modified p o maximum power point tracking method with reduced steady-state oscillation and improved tracking efficiency. *IEEE Transactions on Sustainable Energy*, 7(4):1506–1515, Oct 2016.
- [11] S. Oprea M. Rosu-Hamzescu. Practical guide to implementing solar panel mppt algorithms. *Microchip Technology Inc*, 2013.
- [12] Ahmed YAHDHOU, Abdel Mahmoud, and Issakha Youm. Modeling and optimization of a photovoltaic generator with matlab/simulink. *International Journal of Innovative Technology and Exploring Engineering (IJITEE)*, 3:108–111, 09 2013.
- [13] G.Harita A. Pradeep Kumar Yadav, S.thirumaliah. Comparison of mppt algorithms for dc-dc converters based pv systems. *International Journal of Advanced Research in Electrical, Electronics and Instrumetation Engineering*, 1(1):2278–8875, 2012.
- [14] S. Tang, Y. Sun, Y. Chen, Y. Zhao, Y. Yang, and W. Szeto. An enhanced mppt method combining fractional-order and fuzzy logic control. *IEEE Journal of Photovoltaics*, 7(2):640–650, March 2017.
- [15] F. Lin, K. Lu, and B. Yang. Recurrent fuzzy cerebellar model articulation neural network based power control of a single-stage three-phase grid-connected photovoltaic system during grid faults. *IEEE Transactions on Industrial Electronics*, 64(2):1258–1268, Feb 2017.

- [16] K. S. Tey, S. Mekhilef, M. Seyedmahmoudian, B. Horan, A. T. Oo, and A. Stojcevski. Improved differential evolution-based mppt algorithm using sepic for pv systems under partial shading conditions and load variation. *IEEE Transactions on Industrial Informatics*, 14(10):4322–4333, Oct 2018.
- [17] K. S. Tey and S. Mekhilef. Modified incremental conductance algorithm for photovoltaic system under partial shading conditions and load variation. *IEEE Transactions on Industrial Electronics*, 61(10):5384–5392, Oct 2014.
- [18] K. S. Tey and S. Mekhilef. Modified incremental conductance algorithm for photovoltaic system under partial shading conditions and load variation. *IEEE Transactions on Industrial Electronics*, 61(10):5384–5392, Oct 2014.
- [19] R. Storn and K. Price. Minimizing the real functions of the icec'96 contest by differential evolution. In *Proceedings of IEEE International Conference on Evolutionary Computation*, pages 842–844, May 1996.
- [20] Mohammad Faridun Naim Tajuddin, Shahrin Md Ayob, Zainal Salam, and Mohd Sazli Saad. Evolutionary based maximum power point tracking technique using differential evolution algorithm. *Energy and Buildings*, 67:245 – 252, 2013.
- [21] Ahmed A. Zaki Diab and Hegazy Rezk. Global mppt based on flower pollination and differential evolution algorithms to mitigate partial shading in building integrated pv system. *Solar Energy*, 157:171 – 186, 2017.
- [22] Arduino. Arduino nano. <https://store.arduino.cc/arduino-nano>, 2019. [Online; accessed 2019-4-27].

A Arduino NANO

The Arduino NANO development board is used to implement and run the MPPT algorithms, sensors and PWM. All the mentioned functions have to be controlled by the written codes into the Arduino.

There are different types of micro controllers and micro processors which could have been used in this projects, for example Olimex, Raspberry Pi, FPGA etc. Table 18 tabulates different parameters of the micro processors and micro controllers. The information have been gathered from the data-sheets and [22].

	FPGA	Raspberry	Olimex	Arduino NANO
Type	Micro processor	Micro processor	Micro controller	Micro controller
Clk frequency	2.4GHz	1.4GHZ	80MHz	16MHz
CPU	Xilinx spartan	Cortex A53	ARM-STM32	Atmega328p
ADC register		64-32 bits	32 bits	10 bits
Flash Memory		1GB	256KB	32KB
Power consumption	10-100W	1.5-6.7W		0.1W
Weights	127g	7-45g	21.8g	7g

Table 18: Comparison table between different types of processors. Some data are not available on the data-sheets. The Power consumption depends on the implemented codes on the micro controllers

The chosen controller has to be as light as possible to be board on the Solar Drone. From the table 18 can be seen that the Arduino NANO is much lighter than others. Moreover, the micro controller has to be less power consumption to save the electrical energy for the drone. In this case, the Arduino NANO could be the best choice in terms of weights and power consumption. On the other hands, the micro controller should be sufficient enough in terms of clock frequency, Flash Memory, CPU and ADC register to run the implemented codes properly.

The Arduino NANO does meet all the requirements for our projects, for example the PWM frequency and ADC register. Moreover Arduino has big community. Therefore, the Arduino NANO has been chosen as the micro controller in this project.

B Solar simulators

This section gives the characteristics of the two solar modules at the Solar Lab. The results were checked whether the solar simulators are suitable to operate the Arduino NANO together with the SEPIC converter or not.

The implemented algorithm and the converter had to be tested together to check their functionality. The I-V characteristics of the two solar simulators have been drawn to check whether the operating of the solar simulators do meet the requirements of the converter or not. These measurements also have been done to find the MPP of the simulators in different configurations. The results could have been done to check the algorithms which is implemented on the Arduino NANO. The two simulators are available at the Solar Lab are the Solar Trainer and the ST014.

B.1 SOLAR TRAINER

Firstly, we measured the Solar Trainer in two different configurations including the single module and the TCT configuration. The Solar Trainer in the single module generates 20 [V] for the Voc, and 0.4 [A] for the Isc. This Voc is much higher than the workings voltage of the converter. In addition, the input voltage of the converter should be in the range of 1.2 [V]- 7.2[V]. Otherwise, the converter faces failure. Figures 29, 30, 31 and 32 depict the I-V and P-V curves of the Solar Trainer in different configurations. Figure 33 shows the Solar Trainer in the TCT configuration. The tables 19 and 22 tabulate the correspondent measurements of the single module and the TCT configuration respectively. The tables 20 and 21 tabulate the voltages and currents of the Solar Trainer in 0.8 and 1.2 [A] modes respectively. The maximum powers of the mentioned tables are important.

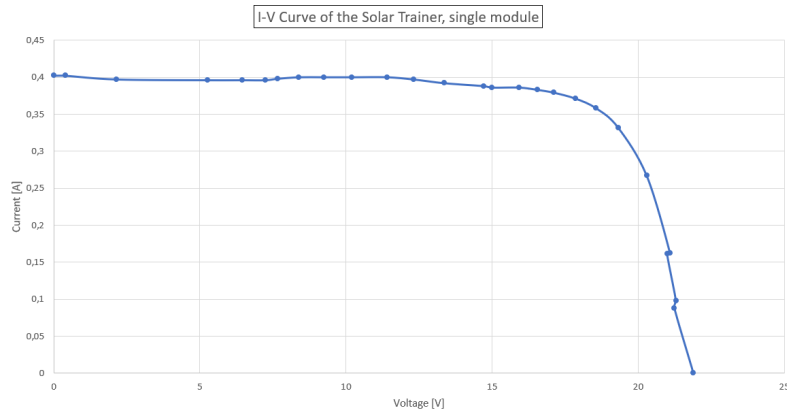


Figure 29: Solar Trainer, single module, I-V curve

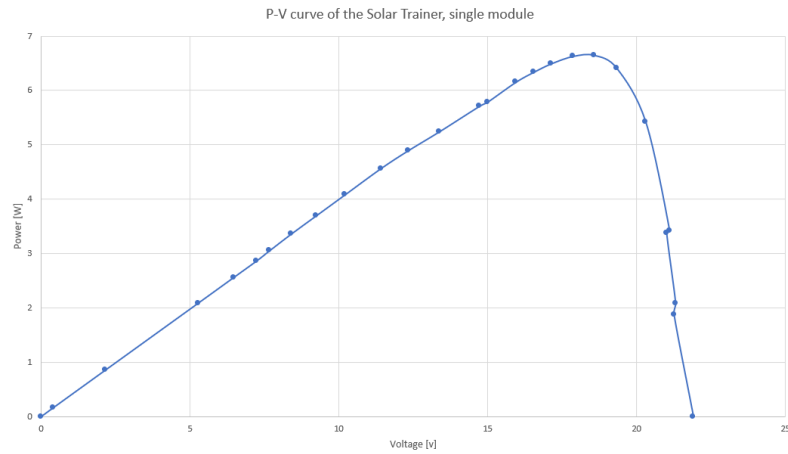


Figure 30: Solar Trainer, single module, P-V curve

Table 19: The measured voltages and currents of the SOLAR TRAINER in the single module for $I_{sc}=0.4$.

Voltage [V]	Current [A]	Power [W]	Voltage [V]	Current [A]	Power [W]
0	0,402	0	15	0,386	5,79
0,4	0,402	0,1608	15,94	0,386	6,15284
2,15	0,397	0,85355	16,55	0,383	6,33865
5,27	0,396	2,08692	17,13	0,379	6,49227
6,46	0,396	2,55816	17,87	0,371	6,62977
7,24	0,396	2,86704	18,57	0,358	6,64806
7,67	0,398	3,05266	19,32	0,332	6,41424
8,4	0,4	3,36	20,3	0,267	5,4201
9,24	0,4	3,696	21,1	0,162	3,4182
10,2	0,4	4,08	21	0,161	3,381
11,41	0,4	4,564	21,3	0,098	2,0874
12,32	0,397	4,89104	21,25	0,088	1,87
13,36	0,392	5,23712	21,9	0	0
14,72	0,388	5,71136			

Table 20: The measured voltages and currents of the SOLAR TRAINER in the single module for $I_{sc}=0.8$.

Voltage [V]	Current [A]	Power [W]
0	0,783	0
0,675	0,785	0,53
1.441	0.785	1.13
3.59	0,782	2,81
5.38	0.782	4,21
9.16	0,781	7.15
12.59	0.778	9.795
15.86	0.77	12.21
17.15	0,764	13.10
17.93	0.756	13.83
18.29	0.75	13.72
18.62	0.743	13.84
19.63	0.71	13.93
20.63	0.628	12.96
21.7	0.427	9.27
22.32	0.177	3.95
2.35	0.116	2.59
22.21	0,092	2.04

Table 21: The measured voltages and currents of the SOLAR TRAINER in the single module for $I_{sc}=1.2$.

Voltage [V]	Current [A]	Power [W]
0	1.189	0
0.81	1.189	0.963
1.936	1.186	2.30
5.34	1.185	6.32
11.2	1.186	13.28
13.65	1.177	16.06
16.23	1.167	18.94
17.05	1.16	19.78
18.4	1.13	20.79
19.37	1.083	20.98
20.63	0.929	19.17
21.23	0.779	16.54
21.87	0.529	11.57
22.28	0.276	6.15
22.4	0.118	2.646
22.32	0.093	2.08
22.52	0	0

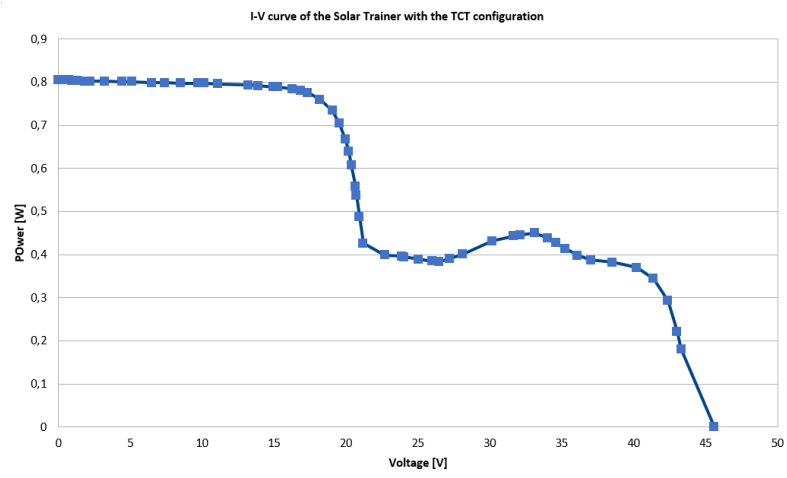


Figure 31: Solar Trainer, TCT configuration, I-V curve

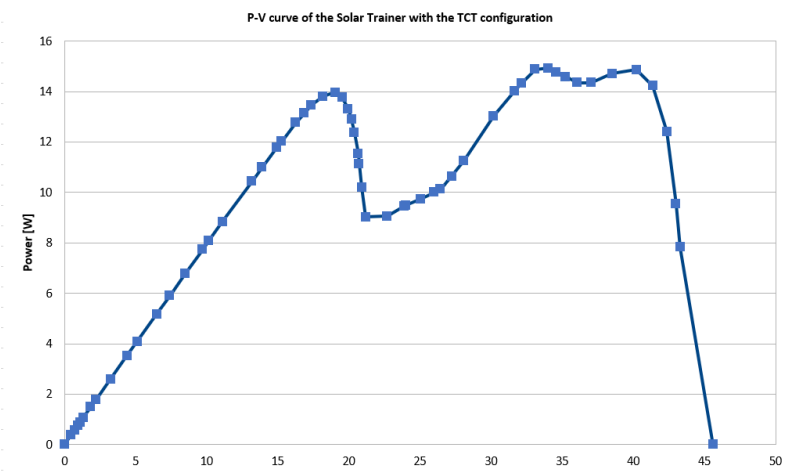


Figure 32: Solar Trainer, TCT configuration, P-V curve

Table 22: The measured voltages and currents of the SOLARTRAINER in the TCT configuration.

Voltage [V]	Current [A]	Power [W]	Voltage [V]	Current [A]	Power [W]
0	0,806	0	20,38	0,607	12,37066
0,475	0,805	0,382375	20,66	0,558	11,52828
0,71	0,805	0,57155	20,71	0,538	11,14198
0,92	0,804	0,73968	20,91	0,488	10,20408
1,1	0,804	0,8844	21,18	0,426	9,02268
1,33	0,804	1,06932	22,7	0,399	9,0573
1,85	0,802	1,4837	23,89	0,396	9,46044
2,23	0,802	1,78846	24,02	0,395	9,4879
3,232	0,802	2,592064	25,05	0,389	9,74445
4,41	0,801	3,53241	25,99	0,385	10,00615
5,1	0,801	4,0851	26,43	0,383	10,12269
6,48	0,799	5,17752	27,22	0,391	10,64302
7,39	0,799	5,90461	28,09	0,401	11,26409
8,5	0,798	6,783	30,17	0,432	13,03344
9,7	0,798	7,7406	31,62	0,443	14,00766
10,15	0,798	8,0997	32,11	0,446	14,32106
11,1	0,796	8,8356	33,09	0,45	14,8905
13,17	0,793	10,44381	34,01	0,439	14,93039
13,89	0,792	11,00088	34,57	0,427	14,76139
14,94	0,789	11,78766	35,24	0,414	14,58936
15,25	0,789	12,03225	36,07	0,398	14,35586
16,26	0,785	12,7641	37,02	0,388	14,36376
16,85	0,78	13,143	38,5	0,382	14,707
17,33	0,776	13,44808	40,2	0,37	14,874
18,18	0,76	13,8168	41,37	0,344	14,23128
19,04	0,734	13,97536	42,36	0,293	12,41148
19,52	0,705	13,7616	43	0,222	9,546
19,94	0,668	13,31992	43,3	0,181	7,8373
20,18	0,639	12,89502	45,6	0	0

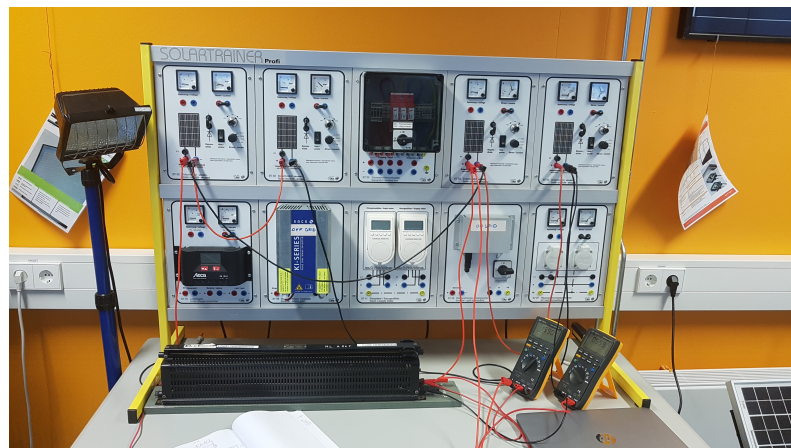


Figure 33: Solar Trainer, TCT configuration

B.2 ST014 simulator

The other simulator (ST014) also generates electricity at 20 [V] for the Voc. However, this value could decrease by shading of some cells. The shading of some cells results the Voc at 6 [V]. Moreover, the Isc decreased to 717 [uA] as well and this value is much lower than the expected current by the solar cells which will be mounted on our drone. Therefore, this simulator is not suitable for our work. Figures 34, 35 and 36 show the results of the ST014. Table 23 corresponds for the values of the mentioned figures.

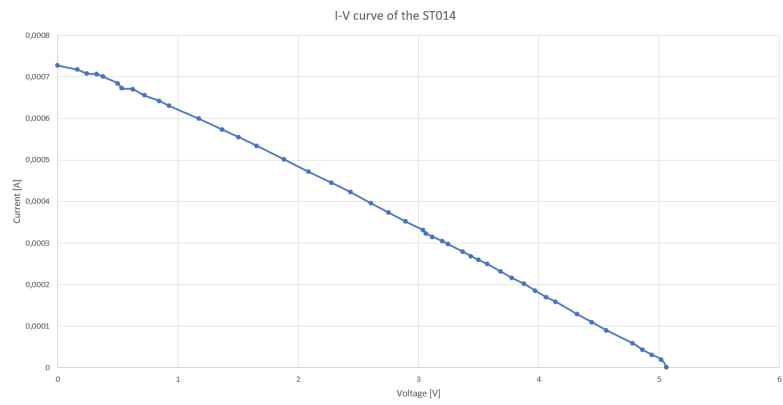


Figure 34: ST014, I-V curve

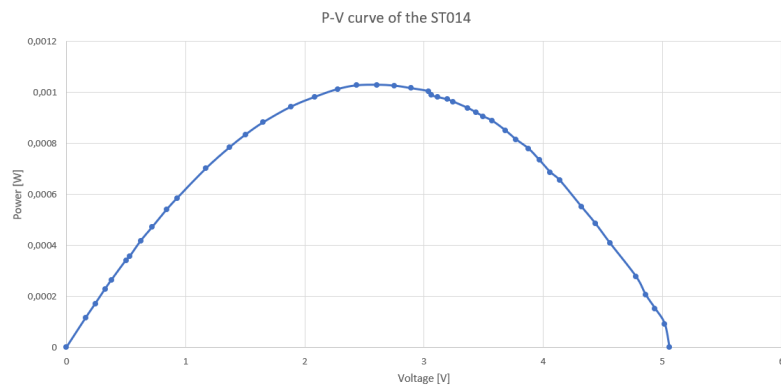


Figure 35: ST014, P-V curve

Table 23: The measured voltages and currents of the ST014.

Voltage [V]	Current [A]	Power [W]	Voltage [V]	Current [A]	Power [W]
0	0,000727	0	3,061	0,000323	0,000989
0,162	0,000717	0,000116	3,117	0,0003148	0,000981
0,242	0,000708	0,000171	3,195	0,0003043	0,000972
0,324	0,000706	0,000229	3,245	0,0002969	0,000963
0,378	0,0007	0,000265	3,369	0,0002785	0,000938
0,5	0,000684	0,000342	3,435	0,0002683	0,000922
0,532	0,000672	0,000358	3,498	0,0002588	0,000905
0,624	0,00067	0,000418	3,572	0,0002488	0,000889
0,721	0,000655	0,000472	3,682	0,0002312	0,000851
0,844	0,000642	0,000542	3,773	0,000216	0,000815
0,927	0,00063	0,000584	3,876	0,0002012	0,00078
1,172	0,000599	0,000702	3,97	0,0001849	0,000734
1,367	0,000573	0,000783	4,06	0,0001692	0,000687
1,502	0,000555	0,000834	4,14	0,0001582	0,000655
1,653	0,000534	0,000883	4,32	0,0001279	0,000553
1,882	0,000501	0,000943	4,44	0,0001092	0,000485
2,085	0,000471	0,000982	4,56	0,0000898	0,000409
2,275	0,000445	0,001012	4,78	0,000058	0,000277
2,434	0,000422	0,001027	4,86	0,0000426	0,000207
2,606	0,000395	0,001029	4,94	0,0000308	0,000152
2,751	0,000373	0,001026	5,02	0,0000185	9,29E-05
2,89	0,0003516	0,001016	5,06	0	0
3,037	0,0003306	0,001004			



Figure 36: ST014 under partially shading

As it can be seen from the Figures 34 and 35, the results are not as perfect as it was expected. It is because the module on the ST014 was affected by the other lights available at the Solar Lab than the ST014's light. Moreover, observing the voltages and currents manually, affected the precision of the measurements, since they fluctuated rapidly during the observing when the module got warm. The results showed that the the ST014 is not suitable for testing the algorithms together with the purposed converters. However, a SEPIC converter with a higher current limitation has been used to test the micro controller by the Solar Trainer.

C Tables of the measurements

Table 24: The real (r) and measured (m) voltages and their evaluated error before and after the calibration.

r [V] before	m [V] before	error[%]	r [V] after	m [V] after	error [%]
0	0	0	0	0.03	0
0.18	0.17	5.56	0.15	0.08	46.67
0.20	0.19	5.00	0.20	0.13	35
0.23	0.24	4.35	0.35	0.39	11.4
0.43	0.44	2.33	0.39	0.39	0
0.75	0.78	4.00	0.42	0.39	7.14
0.76	0.66	13.16	0.75	0.81	8.00
0.88	0.93	5.68	0.99	1.02	3.03
1	1.05	5.00	1.32	1.23	6.82
1.20	1.27	5.83	1.50	1.44	4.00
1.50	1.56	4.00	1.84	1.77	3.80
2	2.10	5.00	2.10	2.03	3.33
2.20	2.32	5.45	2.16	2.08	3.70
3	3.03	1	2.39	2.31	3.35
3.33	3.49	4.80	2.96	2.88	2.70
4.23	4.30	1.65	3.15	3.09	1.90
5	5.10	1.99	3.79	3.72	1.85
5.20	5.30	1.92	4	3.91	2.25
6	6.15	2.50	4.22	4.15	1.66
6.13	6.28	2.45	4.68	4.62	1.28
6.99	7.18	2.72	4.95	4.87	1.62
7.65	7.89	3.14	5.18	5.11	1.35
8.01	8.25	3	5.44	5.37	1.29
8.68	8.96	3.23	5.69	5.63	1.05
9	9.28	3.11	5.93	5.86	1.18
9.46	9.77	3.28	6	5.93	1.17
9.88	10.21	3.34	6.75	6.68	1.04
10.09	10.43	3.37	6.88	6.82	0.87
10.50	10.84	3.24	7.03	6.99	0.57
10.76	11.11	3.25	7.44	7.39	0.67
11.44	11.84	3.50	8.10	8.04	0.74
11.90	12.31	3.45	8.73	8.68	0.57
12.33	12.77	3.57	9	8.94	0.67
12.88	13.33	3.49	9.5	9.45	0.53
13.08	13.55	3.59	9.98	9.95	0.30
13.29	13.77	3.61	10.46	10.42	0.38
13.95	14.46	3.66	11.30	11.26	0.35
14.62	15.16	3.69	11.61	11.59	0.17
15	15.56	3.73	12.64	12.60	0.32
15.61	16.19	3.72	13	12.98	0.15
16	16.6	3.75	13.77	13.75	0.14
16.44	17.07	3.83	14.50	14.48	0.14
16.99	17.65	3.88	14.98	14.97	0.07
17.54	18.22	3.88	15.66	15.65	0.06
17.85	18.56	3.98	16	15.98	0.12
18.10	18.78	3.76	16.23	16.22	0.06
18.72	19.49	4.11	17	16.99	0.06
19	19.75	3.95	18	18	0
19.6	20.39	4.03	19	19.01	0.05
20	20.80	4.00	19.66	19.69	0.15
			20	20.05	0.25

Table 25: The real (r) and measured (m) currents and their evaluated errors before and after the calibration.

m [A] before	r [A] before	error [%]	r [A] after	m [A] after	error [%]
0.08	0	0	0	0.08	1.96
0.16	0.186	13.98	0.174	0.16	8.05
0.24	0.277	13.36	0.307	0.29	5.54
0.34	0.324	4.94	0.438	0.42	4.11
0.37	0.415	10.84	0.613	0.60	2.12
0.42	0.462	9.09	0.830	0.82	1.20
0.48	0.507	5.32	1.005	0.97	3.48
0.55	0.6	8.33	1.223	1.21	1.06
0.63	0.647	2.63	1.442	1.42	1.53
0.71	0.739	3.92	1.792	1.79	0.11
0.85	0.876	2.97	1.923	1.92	0.16
0.93	0.969	4.03	2.193	2.28	3.97
1.08	1.108	2.53	2.445	2.44	0.20
1.16	1.2	3.33	2.739	2.73	0.33
1.27	1.29	1.55	3	2.99	0.33
1.40	1.428	1.96	3.216	3.2	0.50
1.53	1.566	2.30	3.476	3.46	0.46
1.69	1.699	0.53	3.775	3.78	0.13
1.77	1.791	1.17	3.991	3.99	0.03
1.90	1.928	1.45	4.245	4.22	0.59
2.09	2.112	1.04	4.535	4.54	0.11
2.33	2.340	0.43	4.767	4.75	0.36
2.51	2.519	0.36	5.001	4.98	0.42
2.7	2.7	0			
2.88	2.882	0.07			
3.04	3.062	0.72			
3.33	3.334	0.12			
3.54	3.552	0.34			
3.88	3.868	0.31			
4.12	4.135	0.36			
4.49	4.484	0.13			
4.73	4.707	0.49			
4.94	4.916	0.49			
5.02	5.001	0.38			

Table 26: Twelve solar cells in series. 530 W.m^{-2}

Duty cycle	V[V]	I[A]	P[W]
0.25	6.39	0.13	0.85
0.26	6.39	0.13	0.85
0.26	6.39	0.13	0.85
0.27	6.39	0.13	0.85
0.27	6.39	0.13	0.85
0.28	6.37	0.13	0.85
0.29	6.37	0.13	0.85
0.29	6.37	0.13	0.85
0.30	6.37	0.13	0.85
0.31	6.35	0.13	0.85
0.31	6.35	0.13	0.85
0.32	6.35	0.13	0.85
0.32	6.35	0.13	0.85
0.33	6.32	0.13	0.84
0.34	6.32	0.16	1.01
0.34	6.30	0.16	1.00
0.35	6.30	0.16	1.00
0.36	6.30	0.18	1.16
0.36	6.28	0.18	1.16
0.37	6.28	0.18	1.16
0.37	6.25	0.18	1.16
0.38	6.23	0.21	1.32
0.39	6.23	0.24	1.48
0.39	6.21	0.24	1.47
0.40	6.21	0.26	1.64
0.41	6.18	0.26	1.63
0.41	6.14	0.29	1.78
0.42	6.14	0.29	1.78
0.43	6.14	0.32	1.94
0.43	6.11	0.34	2.09
0.44	6.09	0.34	2.09
0.44	6.04	0.37	2.23
0.45	6.02	0.40	2.38
0.46	6.02	0.42	2.53
0.46	5.99	0.45	2.68
0.47	5.97	0.47	2.83
0.47	5.90	0.50	2.95
0.48	5.88	0.53	3.09
0.49	5.85	0.55	3.23
0.49	5.83	0.58	3.37
0.50	5.81	0.60	3.51
0.51	5.76	0.63	3.63
0.51	5.69	0.68	3.89
0.52	5.64	0.71	4.00
0.52	5.60	0.74	4.12
0.53	5.57	0.76	4.24
0.54	5.53	0.79	4.35
0.54	5.43	0.84	4.56
0.55	5.36	0.84	4.50

0.56	5.31	0.92	4.88
0.56	5.29	0.95	5.00
0.57	5.22	1.00	5.21
0.57	5.13	1.02	5.25
0.58	5.01	1.05	5.26
0.59	4.96	1.10	5.47
0.59	4.92	1.15	5.68
0.60	4.87	1.18	5.75
0.61	4.75	1.23	5.86
0.61	4.63	1.26	5.83
0.62	4.54	1.29	5.84
0.63	4.47	1.34	5.98
0.63	4.40	1.39	6.11
0.64	4.31	1.42	6.10
0.64	4.09	1.42	5.80
0.65	3.88	1.42	5.50
0.66	3.79	1.47	5.57
0.66	3.72	1.50	5.56
0.67	3.55	1.50	5.31
0.68	3.32	1.50	4.96
0.68	3.11	1.50	4.65
0.69	3.06	1.50	4.58
0.69	2.92	1.50	4.37
0.70	2.83	1.52	4.30
0.71	2.73	1.52	4.16
0.71	2.57	1.52	3.91
0.72	2.40	1.52	3.66
0.73	2.31	1.52	3.51
0.73	2.24	1.52	3.41
0.74	2.15	1.52	3.27
0.74	2.01	1.52	3.05
0.75	1.89	1.52	2.87
0.76	1.82	1.52	2.77
0.76	1.75	1.52	2.66
0.77	1.68	1.52	2.55
0.77	1.58	1.52	2.41
0.78	1.51	1.52	2.30
0.79	1.42	1.52	2.16
0.79	1.35	1.52	2.05
0.80	1.30	1.55	2.01
0.81	1.26	1.55	1.94
0.81	1.18	1.55	1.83
0.82	1.09	1.55	1.69
0.83	1.04	1.55	1.62
0.83	1.02	1.55	1.58
0.84	0.97	1.55	1.51
0.84	0.93	1.55	1.43
0.85	0.88	1.55	1.36

Table 27: Twelve solar cells in series. 900 W.m^{-2}

Duty cycle	V[V]	I[A]	P[W]
0.25	6.84	0.13	0.91
0.26	6.84	0.13	0.91
0.26	6.84	0.13	0.91
0.27	6.84	0.13	0.91
0.27	6.84	0.13	0.91
0.28	6.84	0.13	0.91
0.29	6.84	0.13	0.91
0.29	6.84	0.13	0.91
0.30	6.84	0.13	0.91
0.31	6.84	0.13	0.91
0.31	6.82	0.13	0.91
0.32	6.82	0.13	0.91
0.32	6.82	0.13	0.91
0.33	6.82	0.16	1.08
0.34	6.79	0.16	1.08
0.34	6.79	0.16	1.08
0.35	6.77	0.18	1.25
0.36	6.77	0.18	1.25
0.36	6.77	0.21	1.43
0.37	6.75	0.21	1.43
0.37	6.75	0.21	1.43
0.38	6.72	0.24	1.60
0.39	6.70	0.24	1.59
0.39	6.70	0.29	1.94
0.40	6.70	0.29	1.94
0.41	6.68	0.29	1.94
0.41	6.63	0.32	2.09
0.42	6.63	0.34	2.27
0.43	6.63	0.37	2.44
0.43	6.60	0.37	2.43
0.44	6.60	0.40	2.61
0.44	6.56	0.42	2.76
0.45	6.53	0.45	2.92
0.46	6.53	0.47	3.10
0.46	6.51	0.50	3.25
0.47	6.49	0.53	3.41
0.47	6.46	0.55	3.57
0.48	6.42	0.58	3.71
0.49	6.39	0.58	3.70
0.49	6.37	0.66	4.18
0.50	6.37	0.68	4.35
0.51	6.32	0.71	4.48
0.51	6.28	0.74	4.62
0.52	6.23	0.76	4.74
0.52	6.21	0.81	5.05
0.53	6.18	0.87	5.36
0.54	6.14	0.89	5.48
0.54	6.09	0.95	5.76
0.55	6.04	0.97	5.87

0.56	5.99	1.02	6.14
0.56	5.95	1.08	6.40
0.57	5.90	1.13	6.66
0.57	5.85	1.18	6.91
0.58	5.76	1.23	7.10
0.59	5.69	1.31	7.46
0.59	5.64	1.34	7.55
0.60	5.62	1.39	7.81
0.61	5.55	1.44	8.01
0.61	5.43	1.50	8.12
0.62	5.31	1.55	8.23
0.63	5.27	1.60	8.43
0.63	5.20	1.68	8.73
0.64	5.13	1.73	8.88
0.64	5.01	1.78	8.93
0.65	4.87	1.81	8.81
0.66	4.73	1.89	8.93
0.66	4.68	1.97	9.21
0.67	4.61	2.02	9.31
0.68	4.47	2.05	9.14
0.68	4.28	2.07	8.87
0.69	4.16	2.12	8.84
0.69	4.07	2.20	8.97
0.70	3.98	2.25	8.97
0.71	3.86	2.28	8.80
0.71	3.67	2.28	8.38
0.72	3.44	2.28	7.84
0.73	3.34	2.31	7.71
0.73	3.23	2.33	7.53
0.74	3.08	2.36	7.28
0.74	2.94	2.36	6.95
0.75	2.76	2.36	6.51
0.76	2.62	2.36	6.17
0.76	2.48	2.36	5.84
0.77	2.43	2.39	5.79
0.77	2.33	2.41	5.63
0.78	2.17	2.41	5.24
0.79	2.01	2.41	4.84
0.79	1.94	2.41	4.67
0.80	1.89	2.41	4.56
0.81	1.82	2.41	4.39
0.81	1.70	2.41	4.10
0.82	1.58	2.41	3.82
0.83	1.51	2.41	3.65
0.83	1.44	2.41	3.48
0.84	1.37	2.44	3.34
0.84	1.30	2.44	3.17
0.85	1.26	2.44	3.06

D Algorithm code

```

1 //Author: Cong
2 //P\%0 and incremental conductance algorithm
3
4 #include <ResponsiveAnalogRead.h>
5
6 #define myOutputPin 9 // output pwm
7 #define TOP_PWM 160
8 #define TOP_TIMER 155
9 #define analogInput A1
10 #define analogInput1 A0
11 #define R1 29970.0
12 #define R2 7500.0
13 #define Vref 5.0
14 #define ADC_RESOLUTION 1023.0
15 #define STEPSIZE 1 //1==> 0.625% stepsize
16 #define P0 1 //P&0 alg
17 #define IC 2 //IC alg
18 #define P02 3 //P0 with variable step size
19 #define IC2 4 //IC with variable step size
20 #define CURVE 5 //duty sweep
21 #define eff 21.58 //21.58 8.18 13.35 \\efficiency value to be set to
    calculate the efficiency
22 #define Con 1 // a constant value use for testing
23
24 volatile int alg = P0; //choose which algorithm to use
25 volatile int count = 1; // value use for variable step size
26 volatile int countt = 1; //value for dividing the sampling frequency
27
28 volatile float Pold = 0;
29 volatile float P = 0;
30 volatile int stepold=1;
31
32 volatile float V = 0.0;
33 volatile float I = 0.0;
34 volatile float Vold = 0.0;
35 volatile float Iold = 0.0;
36 volatile float dI = 0.0;
37 volatile float dV = 0.0;
38 volatile float Pbest = 0.0;
39 volatile float Dbest = 0.0;
40 volatile float err = 0.06; // err for IC
41
42
43
44
45 void changeDuty(float d)
46 {
47     if (d > 1)
48         return;
49     else
50         OCR1A = (int)(d*TOP_PWM) - 1;
51 }
52
53 void setDuty(int d)
54 {
55     unsigned int temp = OCR1A + d;

```

```

56  if (temp > TOP_PWM-1)
57      return;
58  else
59      OCR1A = temp;
60  }
61
62
63  void init_timer()
64  {
65      TCCROA = 0;
66      TCCROB = 0;
67      TCNT0 = 0;                //timer0 to 0
68      OCROA = TOP_TIMER;       //timer TOP
69      TCCROA |= (1 << WGM01);   //ctc mode
70      TCCROB |= (1 << CS02) | (0 << CS01) | (1 << CS00); //prescale 1024
71      TCCROA |= (0 << COM0A1) | (1 << COM0A0); //toggle pin
72      TIMSK0 = (1 << OCIE0A);   //enable timer 0
73      interrupt
74  }
75
76  void init_pwm()
77  {
78      TCCR1A = 0;
79      TCCR1B = 0;
80      TCNT1 = 0;
81      ICR1 = TOP_PWM-1;        //set timer TOP (100kHz)
82      float r = random(0.25, 0.85);
83      changeDuty(0.5);         // set initial duty cycle(50%)
84      TCCR1A |= (1 << COM1A1); //Non-inverted output on OC1A
85      TCCR1A |= (1 << WGM11); // Fast PWM with TOP in ICR
86      TCCR1B |= (1 << WGM13) | (1 << WGM12);
87      TCCR1B |= (0 << CS12) | (1 << CS10); // clock on, no pre-scaler
88  }
89
90
91  ResponsiveAnalogRead voltage_sensor(analogInput, true); //use
92  ResponsiveAnalogRead current_sensor(analogInput1, true);
93
94  void setup() {
95      cli();
96      sei();
97      analogReference(DEFAULT);
98      Serial.begin(9600);
99      pinMode(myOutputPin, OUTPUT);
100     // pinMode(myOutputPin1, OUTPUT);
101     pinMode(analogInput, INPUT); //sensor voltage
102     pinMode(analogInput1, INPUT); //sensor current
103     init_timer();
104     init_pwm();
105  }
106
107
108  void print(){
109
110     if(alg!=0){
111         Serial.print((float)(OCR1A+1)/TOP_PWM);

```

```

112     Serial.print(" I:");
113     Serial.print(I);
114     Serial.print(" V:");
115     Serial.print(V);
116     Serial.print(" P:");
117     Serial.print(P);
118     Serial.print(" eff:");
119     Serial.println(P/eff);}
120     else{
121     Serial.print((float)(OCR1A+1)/TOP_PWM);
122     Serial.print(" I:");
123     Serial.print(readI());
124     Serial.print(" V:");
125     Serial.print(readV());
126     Serial.print(" P:");
127     Serial.print(readV()*readI());
128     Serial.print(" eff:");
129     Serial.println(P/eff);}
130
131
132
133 }
134
135 void loop() {
136 //do nothing
137
138 }
139
140
141 float readV()
142 {
143
144     int av=0;
145     for(int i = 0; i<1; i++) {
146         voltage_sensor.update();
147         av=av+voltage_sensor.getValue();
148     }
149
150     V = (av/1*Vref)/ADC_RESOLUTION;
151     V =V / (R2/(R1+R2));
152     V=round(1000.0*V)/1000.0;
153     V = V * 0.9619+ 0.03481; //error model
154
155     return V;
156 }
157
158 float readI()
159 {
160
161
162     int av=0;
163     for(int i = 0; i<1; i++) {
164         current_sensor.update();
165         av=av+current_sensor.getValue();
166     }
167
168     I = ( Vref / ADC_RESOLUTION ) * ( av/1 - 511 ) / 0.185;
169     I = round(1000.0*I)/1000.0;

```

```
170 I = I*0.9927+0.02798; //error model
171
172 return I;
173
174 }
175
176 void po(){
177
178 V= readV();
179 I = readI();
180 P = V*I;
181
182 if( (OCR1A<=(int)(0.85*TOP_PWM)-1) & (OCR1A > (int)(0.2*TOP_PWM)-1) ){
183     if((P>=Pold && stepold>=0) | (P<=Pold && stepold<=0) )
184     {
185
186         setDuty(STEPSIZE);
187         stepold = 1;
188     }
189     else
190     {
191         setDuty(-STEPSIZE);
192         stepold = -1;
193     }
194 }
195 else {
196
197     changeDuty(0.25);
198 }
199
200 Pold=P;
201
202 }
203
204 void po2(){
205
206 P = readV()*readI();
207
208 if( (OCR1A <= (int)(0.85*TOP_PWM)-1) & (OCR1A > (int)(0.2*TOP_PWM)-1) ){
209     if((P-Pold>=0 && stepold>=0) | (P-Pold<=0 && stepold<=0) )
210     {
211
212         setDuty(count*STEPSIZE);
213         stepold = 1;
214         count++;
215     }
216     else
217     {
218         setDuty(-STEPSIZE*count);
219         stepold = -1;
220         count = 1;
221     }
222 }
223 else {
224
225     changeDuty(0.25);
226     count = 1;
227 }
```

```
228
229     Pold=P;
230
231 }
232
233 void ic(){
234
235     Vold=V;
236     Iold=I;
237     V=readV();
238     I=readI();
239     dV=V-Vold;
240     dI=I-Iold;
241     P=V*I;
242
243     if( (OCR1A<=(int)(0.85*TOP_PWM)-1) & (OCR1A> (int)(0.2*TOP_PWM)-1) ){
244
245         if(dV==0 && dI==0){
246             Serial.print("MPP found1 ");
247             //do nothing
248         }
249
250         else if (dV==0 && dI>0){
251             setDuty(STEPSIZE);
252             Serial.print("Increases duty1 ");
253         }
254
255         else if (dV==0 && dI<0){
256             setDuty(-STEPSIZE);
257             Serial.print("Decrease duty1 ");
258         }
259
260         else if (abs(dI/dV + I/V) <= err )
261         {
262             //setDuty(0);
263             Serial.print("MPP found ");
264             } //do nothing*/
265
266         else if (dI/dV >-I/V ){
267             setDuty(STEPSIZE);
268             Serial.print("Increases duty2 ");
269         }
270
271         else {//(dI/dV <-I/V)
272             setDuty(-STEPSIZE);
273             Serial.print("Decrease duty2 ");
274         }
275
276     }
277
278     else{
279
280         changeDuty(0.25);
281
282     }
283 }
284
285 }
```

```

286
287 void ic2(){
288
289     Vold=V;
290     Iold=I;
291     V=readV();
292     I=readI();
293     dV=V-Vold;
294     dI=I-Iold;
295     P=V*I;
296
297     if( (OCR1A <= (int)(0.85*TOP_PWM)-1) & (OCR1A > (int)(0.2*TOP_PWM)-1) ){
298
299         if(dV==0 && dI==0){
300             Serial.print("MPP found1 ");
301             count=1;
302             //do nothing
303         }
304
305         else if (dV==0 && dI>0){
306
307             setDuty(STEPSIZE*count);
308             count++;
309             Serial.print("Increase duty1 ");
310         }
311
312         else if (dV==0 && dI<0){
313
314             setDuty(-STEPSIZE*count);
315             count = 1;
316             Serial.print("Decrease duty1 ");
317         }
318
319
320         else if ( abs(dI/dV + I/V) <= err )
321         {
322             //setDuty(0);
323             count=1;
324             Serial.print("MPP found ");
325             } //do nothing
326
327         else if (dI/dV >-I/V ){
328             setDuty(STEPSIZE*count);
329             count++;
330             Serial.print("Increas duty ");
331         }
332
333         else {//(dI/dV+I/V <-I/V){
334             setDuty(-STEPSIZE*count);
335             count = 1;
336             Serial.print("Decrease duty ");
337         }
338
339     }
340
341     else{
342         count = 1;
343         changeDuty(0.25);

```

```
344 }
345 }
346 }
347
348
349
350
351
352 void curve()
353 {
354     if(OCR1A <(int) (TOP_PWM*0.85)-1){
355
356         OCR1A = OCR1A + STEPSIZE;
357         V=readV();
358         I=readI();
359         Serial.print((float)(OCR1A+1)/TOP_PWM);
360         Serial.print(" ");
361         Serial.print(V);
362         Serial.print(" ");
363         Serial.print(I);
364         Serial.print(" ");
365         Serial.println( V*I);
366     }
367     else{
368         changeDuty(0.25);
369     }
370 }
371 }
372
373
374 ISR(TIMERO_COMPA_vect)
375 {
376     if(countt==1) //count 1 --> 100hz, 2 --> 50hz
377     {
378         switch(alg) {
379
380             case P0 :
381                 po();
382                 break;
383             case P02 :
384                 po2();
385                 break;
386
387             case IC :
388                 ic();
389                 break;
390
391             case IC2 :
392                 ic2();
393                 break;
394
395             case CURVE :
396                 curve();
397                 break;
398
399             default :
400                 ic();
401                 break;
```

```

402     }
403
404     countt=0;
405
406     }
407     if(alg!=CURVE) print();
408
409
410     countt++;
411
412 }
413

```

```

1 //Author: Cong
2 //DE algorithm
3
4 #include <ResponsiveAnalogRead.h>
5
6
7 #define myOutputPin 9 // output pwm
8 #define myOutputPin1 6 //OCOA toggle for testing
9 #define TOP_PWM 159
10 #define TOP_TIMER 155
11 #define analogInput A1
12 #define analogInput1 A2
13 #define R1 29970.0
14 #define R2 7500.0
15 #define STEP 1
16 #define F 0.6
17 #define CR 0.67
18 #define Vref 5.0
19 #define WAIT 100
20 #define threshold 0.05
21 #define ADC_RESOLUTION 1023
22
23 volatile float Pold = 0;
24 volatile float P = 0;
25 volatile float V = 0;
26 volatile float I = 0;
27 volatile bool done=false;
28 volatile long randomNumber[3];
29 volatile int check[4]={0.0, 0.0, 0.0, 0.0};
30
31 volatile float Di[4] = {0.2, 0.4, 0.6, 0.8};
32 volatile float Pi[4] = {0.0, 0.0, 0.0, 0.0};
33 volatile float DVi[4] = {0.2, 0.4, 0.6, 0.8};
34 volatile float DUi[4] = {0.0, 0.0, 0.0, 0.0};
35 volatile float PUi[4] = {0.0, 0.0, 0.0, 0.0};
36
37
38
39 float Pbest=0;
40 float Ppr=0;
41 float Dbest=0;
42 float dV,dI;
43 float Vbest,Ibest;
44
45 void setDuty(int d)

```

```

46 {
47   long unsigned temp = OCR1A + d;
48   if (temp > TOP_PWM){
49     OCR1A=0;
50     return;
51   }
52   else
53     OCR1A = temp;
54 }
55
56 void changeDuty(float d)
57 {
58   if (d > 1)
59     return;
60   else
61     OCR1A = d*(TOP_PWM+1)-1;
62 }
63
64 void init_timer()
65 {
66   TCCROA = 0;
67   TCCROB = 0;
68   TCNT0 = 0; //timer0 to 0
69   OCROA = TOP_TIMER; //timer TOP
70   TCCROA |= (1 << WGM01); //ctc mode
71   TCCROB |= (1 << CS02) | (0 << CS01) | (1 << CS00); //prescale 1024
72   TCCROA |= (0 << COM0A1) |(1 << COM0A0) ; //toggle pin
73   TIMSK0 = (1 << OCIE0A); //enable timer 0
74   interrupt
75 }
76
77 void init_pwm()
78 {
79   TCCR1A = 0;
80   TCCR1B = 0;
81   TCNT1 = 0;
82   ICR1 = TOP_PWM; //set timer TOP (100kHz)
83   changeDuty(0.50); // set initial duty cycle(50%)
84   TCCR1A |= (1 << COM1A1); //Non-inverted output on OC1A
85   TCCR1A |= (1 << WGM11); // Fast PWM with TOP in ICR
86   TCCR1B |= (1 << WGM13) | (1 << WGM12);
87   TCCR1B |= (0 << CS12) | (1 << CS10); // clock on, no pre-scaler
88 }
89
90 ResponsiveAnalogRead voltage_sensor(analogInput, true);
91 ResponsiveAnalogRead current_sensor(analogInput1, true);
92
93
94 void setup ()
95 {
96   cli();
97   sei();
98   Serial.begin(9600);
99   pinMode (myOutputPin, OUTPUT);
100 // pinMode (myOutputPin1, OUTPUT);
101 pinMode(analogInput, INPUT); //sensor voltage
102 pinMode(analogInput1, INPUT); //sensor current

```

```

103 // init_timer();
104 init_pwm();
105
106 }
107
108 void start2(){
109
110 Ppr=0;
111 for(int i=0; i<4; i++){ // obtain Pi
112     changeDuty(Di[i]);
113     delay(WAIT);
114     Pi[i] = readV()*readI(); //select Pbest and Dbest
115     if(Pi[i]>Ppr){
116         Pbest=Pi[i];
117         Dbest=Di[i];
118         Ppr=Pi[i];
119     }
120
121 }
122 }
123
124 for(int i=0; i<4; i++){
125     if((Dbest-Di[i])/Dbest>threshold && (Pbest-Pi[i])/Pbest>threshold)
126         break;
127     else if(i==3){
128         done=true;
129         changeDuty(Dbest);
130         delay(WAIT);
131         Vbest=readV();
132         Ibest=readI();
133         load();
134     }
135     }
136     mutation();
137 }
138
139 void start(){
140     Di[0] = 0.2;
141     Di[1] = 0.4;
142     Di[2] = 0.6;
143     Di[3] = 0.8;
144     Ppr=0;
145
146     for(int i=0; i<4; i++){ // obtain Pi
147         changeDuty(Di[i]);
148         delay(WAIT);
149         Pi[i] = readV()*readI(); //select Pbest and Dbest
150         if(Pi[i]>Ppr){
151             Pbest=Pi[i];
152             Dbest=Di[i];
153             Ppr=Pi[i];
154         }
155
156     }
157 }
158
159 for(int i=0; i<4; i++){

```

```

160     if((Dbest-Di[i])/Dbest>threshold && (Pbest-Pi[i])/Pbest>threshold)
161     break;
162     else if(i==3){
163         done=true;
164         changeDuty(Dbest);
165         delay(WAIT);
166         Vbest=readV();
167         Ibest=readI();
168         load();
169     }
170     mutation();
171 }
172 }
173
174 void load(){
175
176     float a;
177     while(done)
178     {
179         Serial.print((float)(OCR1A+1)/(TOP_PWM+1));
180         Serial.print(" ");
181         Serial.println("Pbest");
182
183         if(abs(Pbest-(readV()*readI()))/Pbest > threshold){
184
185             dV=Vbest-readV();
186             dI=Ibest-readI();
187
188             if((dV>0 && dI<0) || (dV<0 && dI>0) ){
189
190                 a=(Ibest/Vbest) *( pow(Dbest,2)/pow(1-Dbest,2))*(readV()/readI());
191                 Dbest= sqrt(a)/(1+sqrt(a)); //formule
192                 changeDuty(Dbest);
193                 delay(WAIT);
194                 Vbest=readV();
195                 Ibest=readI();
196                 Pbest=Vbest*Ibest;
197             }
198             else{ done=false;}
199             start();
200
201         }
202     }
203 }
204 }
205
206
207
208 void mutation()
209 {
210     while(check[0]==0 || check[1]==0 || check[2]==0 || check[3]==0 ){
211         for(int j = 0; j<3 ;j++){
212             randomNumber[j]=random(0, 4);
213         }
214         check[randomNumber[0]]=1;
215
216         if(Dbest<=Di[randomNumber[0]])

```

```

217     DVi[randomNumber[0]] = Di[randomNumber[0]] - F*abs(Di[randomNumber[1]] - Di[
218         randomNumber[2]]);
219     else
219         DVi[randomNumber[0]] = Di[randomNumber[0]] + F*abs(Di[randomNumber[1]] - Di[
220             randomNumber[2]]);
221 }
222 check[0]=0;
223 check[1]=0;
224 check[2]=0;
225 check[3]=0;
226
227 crossover();
228
229 }
230
231 void crossover(){
232     for(int i= 0;i<4;i++){
233         if(random(0,100)/100.0>=CR)
234             DUi[i]=DVi[i];
235         else
236             DUi[i]=Di[i];
237     }
238
239     for(int i=0; i<4; i++){ // obtain PUi
240
241         if(DUi[i]==Di[i] ){
242             PUi[i]=Pi[i];
243             if(DUi[i+1]==DUi[i]){
244                 PUi[i+1]=PUi[i];
245                 i++;
246             }
247         }
248         else{
249             changeDuty(DUi[i]);
250             delay(WAIT);
251             PUi[i] = readV()*readI();
252
253         }
254     }
255 }
256
257 for(int i=0; i<4; i++){
258     if(PUi[i]>=Pi[i]) Di[i]=DUi[i];
259 }
260
261 start2();
262 }
263
264
265
266
267 float readV()
268 {
269
270     int av=0;
271     for(int i = 0; i<1; i++) {
272         voltage_sensor.update();

```

```
273     av=av+voltage_sensor.getValue();
274     }
275
276     V = (av/1*Vref)/ADC_RESOLUTION;
277     V =V / (R2/(R1+R2));
278     V=round(1000.0*V)/1000.0;
279     V = V * 0.9619+ 0.03481;
280
281     return V;
282 }
283
284 float readI()
285 {
286
287
288     int av=0;
289     for(int i = 0; i<1; i++) {
290         current_sensor.update();
291         av=av+current_sensor.getValue();
292     }
293
294     I = ( Vref / ADC_RESOLUTION ) * ( av/1 - 511 ) / 0.185;
295     I = round(1000.0*I)/1000.0;
296     I = I*0.9927+0.02798;
297
298     return I;
299 }
300 }
301
302 void loop ()
303 {
304
305     start();
306
307 }
```


APPENDIX C

Thesis III: DC/DC Converter

Joey Gelderblom & Joris van Roessel

EE3L11 : Thesis Bachelor Project, Electrical Engineering

Solar Drone: Single-Ended Primary-Inductor Converter June, 2019

Group D: DC/DC Converter

Faculty of Electrical Engineering, Mathematics & Computer Science

Authors:

Joris van Roessel, 4387481

Joey Gelderblom, 4441478

Supervised by:

Dr. P.J. van Duijsen

Dr. I. Olindo

Abstract

This document describes the design, simulation and implementation process of a DC/DC converter that will be used for the solar drone project. In this project a solar system will be designed specifically to fit on a drone. This system needs to harvest more energy from solar irradiance than it costs to keep its extra weight in the air, thus in other words extending the flight-time of a drone. The DC/DC converter described in this thesis needs to extract solar energy from a PV-module in order to charge the battery of the drone. The converter will be controlled by the micro-controller subgroup using MPPT (Maximum Power Point Tracker) algorithm. This will be done by supplying a PWM signal to the converter.

The DC/DC converter that will be discussed in this document is the SEPIC (Single-Ended Primary-Inductor Converter). At the end of this thesis we succeeded in designing, simulating and building a SEPIC that is able to be controlled by an Arduino micro-controller. It also ensures safe charging of lithium-ion battery of the drone for solar irradiances up to 1100 W/m^2 . The overall power efficiency of this SEPIC in practice is 82.9% under the circumstances of operating at MPP.

Preface and Acknowledgements

For the past nine weeks, we have specialised ourselves in the discipline of DC/DC converters for PV applications. This subject was well connected to the majority of courses covered in the Electrical Engineering Bachelor programme. With the gathered knowledge throughout our Bachelor study we were able to design, simulate and apply our own converter in the rapidly expanding world of solar energy technology. Besides applying the gained knowledge from the Bachelor study we got the opportunity to expand our knowledge within this field.

Besides applying and building upon the knowledge gained from the Bachelor programme, we also got the opportunity to think beyond the technical part of a project. We got in touch with the business and ethical sides of a project. We experienced this as a great opportunity to get a better understanding of the entirety of a project. This will be very helpful in the future of our electrical engineering careers. These parts of the Bachelor graduation project are covered outside this document.

We would like to express our sincere thanks to our supervisors Dr. P.J. van Duijsen and Dr. I. Olindo for supporting us throughout the project.

Secondly, we want to thank dr. I.E. Lager for the well organised Bachelor graduation programme. Throughout the project we were clearly informed about the structure and deadlines of the programme. We experienced this as very pleasant and are grateful for that.

Furthermore we would like to thank M. Schumacher for the arrangement of all components that we needed in order to build our converter.

Also we would like to thank our other project members D.C. de Best, M.S. Mollaie Daryani, V.C. Nguyen and D.D.D.T.D. Sitaldin for being great support throughout the project.

We finally want to thank our families for the support and the opportunity that they gave us to be able to become an Electrical Engineer.

*Joris van Roessel & Joey Gelderblom
Delft, June 2019*

Contents

1	Introduction	5
1.1	Subdivision of the Project	5
1.2	Objective	5
1.3	Thesis Structure	6
2	Program of Requirements	6
3	Single-Ended Primary-Inductor Converter (SEPIC)	7
3.1	Properties SEPIC	7
3.2	Differences with other DC/DC converters	7
3.2.1	Boost	8
3.2.2	Buck/Boost converter	8
4	Working Principle	9
4.1	Continuous mode	9
4.1.1	On- and Off-states	9
4.1.2	Duty cycle	10
5	Theoretical Design	11
5.1	Components	11
5.1.1	Inductor	11
5.1.2	Switch	12
5.1.3	Diode	13
5.1.4	Capacitor	14
5.2	Components values	15
6	Simulink Simulation	16
6.1	Simulating the working principle	16
6.1.1	Load supply	16
6.1.2	Inductor current	17
6.1.3	Coupling capacitor voltage	19
6.2	Simulating with PV-cells and MPP	19
6.2.1	PV-cells and MPP application	20
6.2.2	Output power	21
6.3	Simulating with a lithium-ion battery	22
6.3.1	Lithium-ion battery	22
6.3.2	Charging the battery	23
7	Practical Application	25
7.1	Inductor	26
7.1.1	Coupled inductor	26
7.2	MOSFET selection	27
7.2.1	Heatsink	28
7.2.1.1	Practical use of Heatsink	28
7.3	Capacitors	28
7.4	Measurements & Results	29
8	Conclusion and Future Work	30
8.1	Conclusion	30
8.2	Future Work	30
9	Appendices	33

A	PV- and IV-Curves of the Simulink PV-Array Block	33
A.1	6-series configuration	33
A.2	12-series configuration	34
A.3	16-series configuration	34
B	Simulink Simulation Results with PV Cells and MPP	35
B.1	6-series configuration	35
B.2	12-series configuration	36
B.3	16-series configuration	37
C	Simulink Simulation Results with PV Cells, MPP and Lithium-ion Battery	38
C.1	Lithium-ion battery in Simulink	38
C.2	6-series configuration	39
C.3	12-series configuration	39
C.4	16-series configuration	40
C.5	Corresponding plots	40
D	Output voltage of first design SEPIC	43
E	Power Efficiency Measurements for MOSFET Decision	44
E.1	SEPIC design 2, IRF530NS MOSFET [10]	44
E.2	SEPIC design 2, CSD18536KCS MOSFET [18]	44
E.3	SEPIC design 3, IRF530NS MOSFET [10]	45
F	Power Efficiency Measurements for Duty Cycle Sweep.	46
F.1	SEPIC design 3, IRF530NS MOSFET [10]	46
G	Inductor Trade-off	47
H	Practical Measurements	48
H.1	Resistive load 20Ω	49
H.2	Lithium-ion battery as load	53

1 Introduction

For the past couple of decades the technical world of solar energy has made big steps in not only the technical efficiency of harvesting solar energy but also in the degree of accessibility by citizens. We as a society are heading towards a world of renewable and climate friendlier source of energy. Because of the increase in efficiency of today's PV-cells, it becomes more attractive for the world of transportation where the PV-system needs to be portable. One segment in this field is drones. The main current bottleneck of the use of drones for any application is the short flight-time due to the battery's weight limitation. With the use of a lightweight, renewable and efficient energy source like today's PV-cells it is possible to extend this flight-time of a battery driven drone. In this Bachelor project a solar system will be designed which will increase the flight-time of a drone.

1.1 Subdivision of the Project

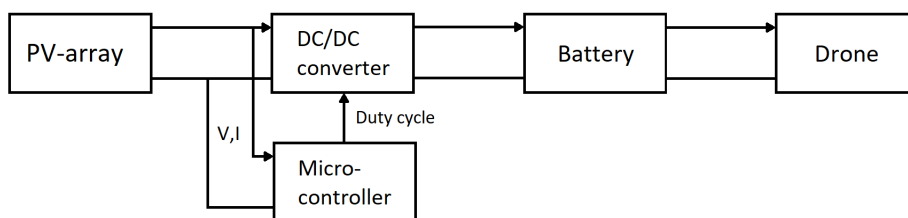


Figure 1: Block diagram of the overall project system.

The project will be divided in three subgroups each responsible for a subsystem of the project. These three subsystems are Power Management & Drone Design, Micro-controller and DC/DC Converter. This thesis will cover the DC/DC Converter subsystem.

The Power Management & Drone Design subgroup is responsible for managing all power flows in the system and will do a research on what the possible extension of flight-time will be. Secondly the total system consisting of the PV-cells, micro-controller and DC/DC converter needs to be applied on a drone. A design and configuration of the PV-cells will be done by this group.

For the Micro-controller subgroup it will be the responsibility to write an algorithm implemented on a micro-controller that will create a PWM signal with varying duty cycle. This duty cycle has to so that the maximum power from the PV-array is extracted, this is also known as MPPT (Maximum Power Point Tracking). The PWM signal will be applied to the DC/DC converter.

The DC/DC Converter subgroup is responsible for extracting power from the PV-array, using the PWM signal of the micro-controller subgroup, and the transportation and conversion of power to charge the battery of the drone at a safe and maximum possible efficient manner.

1.2 Objective

The main objective of the DC/DC Converter subgroup is to design and implement a converter that is capable of safely charging a battery with a PV-array as input power source. It has to be able to be controlled by the Micro-controller subgroup. This micro-controller will send a PWM signal so that the converter will be operating at the MPP of the PV-array at a certain solar irradiance and PV-cell configuration. An overview of the full system is presented in a block diagram shown in [Figure 1](#). The main objective for the DC/DC converter will be to operate as efficient as possible under the circumstances of operating at MPP.

1.3 Thesis Structure

This document will cover the DC/DC converter in six chapters. In chapter 2 it will be stated which DC/DC converter will be used for this project and why we think this converter is favourable over others. In the third chapter the working principle of this converter will be discussed. After we know which converter will be used and how it operates, in chapter 4 a theoretical design will be done. This theoretical design will then be developed in the Matlab application Simulink. In chapter 5 simulations will be done in Simulink. These simulations will be done with 3 setups of the designed converter. With each setup there will be an addition up to the third setup where the converter is connected to a PV-array as input source and a lithium-ion battery as load. Chapter 6 is about the practical design steps taken in the process of actually manufacturing the converter. This chapter will conclude with results from measurements done in the case of a PV-array as input source and both with a resistive load and a lithium-ion battery as load. The last chapter will cover conclusions of the obtained results from both simulations and practical measurements. This chapter will end with a discussion of the future work that can be done if the project would be continued in order to obtain a better performance.

2 Program of Requirements

This program of requirements is about the DC/DC converter part of the solar drone project. With these requirements it is possible to give a concrete conclusion of the work done at the end of the project and indicates what possible work for the future could be in order to satisfy the requirements or even improve them.

As was already stated in [subsection 1.2](#) the main objective of the DC/DC Converter subgroup is to design and implement a converter that is capable of safely charging a battery with a PV-array as input power source as efficient as possible operating at MPP. This results in three requirements that we try to meet at the end of the project.

1. The DC/DC converter must be able to be controlled by the micro-controller.
2. The current flow into the battery cannot not exceed the maximum charge rating of the battery thus guarantee safe charging.
3. The DC/DC converter has an overall power efficiency of 85% operating at MPP.

The literature study done before this thesis showed that a typical SEPIC ([section 3](#)) has a power efficiency of 90%. Because this is the first time we will design a converter and also for PV-application and charging a battery, a requirement of 85% seems reasonable.

3 Single-Ended Primary-Inductor Converter (SEPIC)

The SEPIC is a boost converter followed by an inverted buck-boost converter. It has the capability of the buck-boost converter which is able to both stepping up and down the input voltage, depending on the duty cycle value. The input impedance can be specified by adjusting the duty cycle. Therefore the SEPIC converter is perfect for PV applications, because it is able to match the entire I-V characteristic curve [1].

3.1 Properties SEPIC

let's start with some properties of the SEPIC converter. First of all a very convenient property of the SEPIC is the non-pulsating input current, which does not depend on the operation mode. The input current of the SEPIC is continuous and is able to draw a ripple-free current from for example a PV-array. This is very important for effective MPPT (maximum power point tracking), more over MPPT in the thesis of the micro-controller subgroup. The switch (s) is used to control the output voltage. A PWM (Pulse Width Modulation) signal will control the switch. The varying duty cycle of the PWM signal determines the voltage scaling of the converter. A helpful property of the SEPIC is that the switch control terminal is connected to ground which leaves the user the option to use a simplified gate drive circuitry. A additional gate driver is needed when the PWM signal from the micro-controller is not powerful enough to operate the switch. For this project the micro-controller is an Arduino Nano. This micro-controller will be able to control the gate of the switch. Therefore a gate driver circuit will not be needed.

In practice a transistor will be used as the switch. This can either be a MOSFET (Metal Oxide Semiconductor Field Effective Transistor) or a IGBT (Insulated-Gate Bipolar Transistor). The decision on which of the two suits best for the solar drone project will be further elaborated in [subsubsection 5.1.2](#).

In [Figure 2](#) a circuit diagram of the SEPIC is shown.

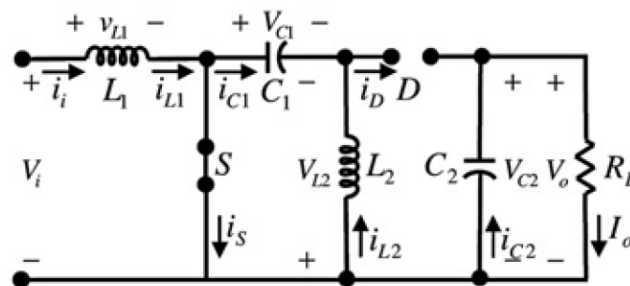


Figure 2: SEPIC circuit diagram [2]

3.2 Differences with other DC/DC converters

There are many DC/DC converters which all have their pros and cons. However not all converters are suitable for the solar drone application. First of all the converter must be able to convert the input voltage, which comes from the PV-array, to the rated voltage of the battery. This input voltage will most of the time be smaller than the output voltage, so the DC/DC converter must be capable of boosting the input voltage. However in a situation where more PV-cells are connected in series, the input voltage could potentially be greater than the rated output voltage of the battery. In this case the converter must be able to buck the input voltage.

3.2.1 Boost

Most of the time, the SEPIC converter will be used as a boost converter. The PV-array produces a voltage which is lower than the rated voltage of the battery at the output. Another DC/DC converter that is used for boosting the input voltage, is the boost converter. There are however some differences between the two.

First of all the SEPIC converter is most of the time not as efficient as the boost-converter. One of the reasons is that the SEPIC converter consist of more components. These components are not ideal and thus have losses which results in heat. A second reason is that the Boost converter has a duty cycle range of 100% for boosting and the SEPIC only has 50%. The boost converter thus is able to use more duty-cycle range for boosting. This results in preciser output voltage values. The Boost converter however is not able to step down the input voltage from the PV-array if needed and therefore is not capable of operating on the complete IV-curve. In other words, when the voltage of the input from the PV-module is greater than the voltage of the battery, the converter will operate in a non-operational region. Because of the buck-boost property of the SEPIC, it is able to step up and step down the input voltage and as a result does not have a non-operational region [3]. The SEPIC is thus overall employable.

3.2.2 Buck/Boost converter

There is however a DC/DC converter which is capable of both boosting and bucking, it is the simple buck/boost converter. There are some differences between the two, for example the SEPIC produces a much lower input ripple current than the buck-boost converter. The higher input ripple current of the buck/boost converter results in a limit of the maximum output power. The switch peak current rating will be hit during the on-time of the MOSFET, which results in a lower output power for the buck/boost converter [4]. The maximum output power of the SEPIC has a much higher value which comes in handy when charging the battery. Moreover the ripple current in [subsubsection 5.1.1](#). Secondly the SEPIC has a non-inverted output, this in contrast with the buck-boost converter. In other words, the output of the SEPIC has the same polarity as the input. This is not necessarily a problem because the buck-boost-converter could be connected with the polarity inverted to the output, however the disadvantage of this is that the common ground property is not applicable anymore and this results in a much more complex DC/DC converter to operate.

4 Working Principle

The working principle of the SEPIC is the same as all other switching regulators. The inductors and capacitors exchange energy to one another in order to regulate the output. These energy flows are controlled by the MOSFET which is controlled by the PWM signal coming from the micro-controller. The duty cycle of this signal determines the balance of time between the MOSFET operating in the on- and off-state per period. These energy flows are created by the inductor resisting changes in current by creating a magnetic field that stores energy, or releasing this stored energy.

4.1 Continuous mode

The SEPIC operates in continuous mode if the current through $L1$ does not reach zero during discharging in the off-state. A high switching frequency or great inductor value can prevent this, however a high inductance comes with the cost of efficiency. The off-state is the case when the switch is open and thus the on-state being the case if the switch is closed. Operating in continuous mode has its advantages over operating in discontinuous mode. The performance is usually better in continuous mode and in addition, it allows the converter to extract the maximum output power from a given input voltage and switch-current rating [5].

4.1.1 On- and Off-states

In the on-state the switch is closed and the source will charge inductor $L1$. This is due the inductor resisting change in current by creating an opposing voltage across its terminals. When the current stabilises and thus the rate of change of current decreases, the opposing voltage will also decrease. At this stage the inductor stores energy in the form of a magnetic field. While the current I_{L1} increases, the current I_{L2} becomes more negative, thus increasing in magnitude but oriented opposite of I_{L1} . The current flows in the on-state are shown in Figure 3.

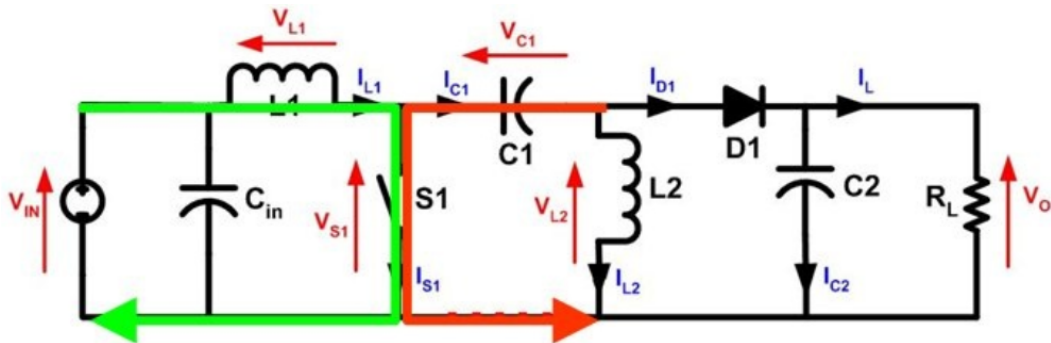


Figure 3: SEPIC circuit in the on-state (switch is closed) [6].

Because the switch is on, it acts as a short circuit. Not only this but also the fact that the instantaneous voltage V_{L1} is approximately V_{in} , causes the voltage V_{L2} to be approximately $-V_{C1}$ according to the following average voltages:

$$V_{in} = V_{L1} + V_{C1} + V_{L2} \tag{1}$$

Because the voltage V_{C1} is approximately equal to V_{in} , $V_{L1} = -V_{L2}$. Therefore it is possible to wound both inductors on the same core, which will be discussed in subsection 5.1.1.

Due to the diode $D1$ the capacitor $C1$ supplies energy to $L2$ which will store it in the form of a magnetic field.

When the switch is turned off, the current through $L1$ and $C1$ will be the same, as inductors do not allow instantaneous changes in current. The negative current I_{L2} adds up with I_{L1} and will be delivered to the load, thus both inductors will supply the load in the off-state. Capacitors $C1$ and $C2$ are charged by $L1$ and $L1+L2$ respectively in this state. The current flows of this state are shown in Figure 4.

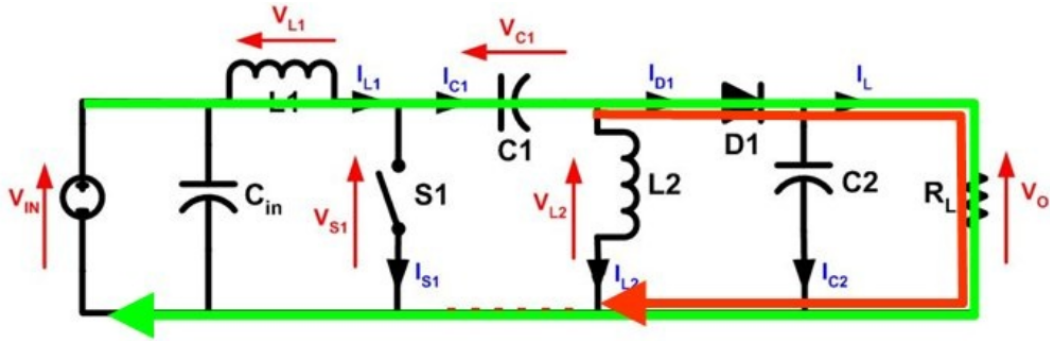


Figure 4: SEPIC circuit in the off-state (switch is open) [6].

4.1.2 Duty cycle

The duty cycle of the SEPIC converter is a function of three different voltages namely; input voltage V_{in} , output voltage V_{out} and the forward voltage drop of the diode V_{FWD} . The equation for the duty cycle is as follows:

$$D = \frac{V_{out} + V_{FWD}}{V_{in} + V_{out} + V_{FWD}} \quad (2)$$

$$D_{max} = \frac{V_{out} + V_{FWD}}{V_{in(min)} + V_{out} + V_{FWD}} \quad (3)$$

$$V_{out} = \frac{D}{1 - D} * V_{in} - V_{FWD} \quad (4)$$

Where V_{FWD} is the forward voltage drop across the diode. It can thus already be concluded that a low forward voltage drop across the diode will be a must. The diode selection is further elaborated in [subsubsection 5.1.3](#).

5 Theoretical Design

For designing a SEPIC a couple parameters need to be specified, like the input voltage range and the maximum ripples for the output voltage and inductor current. After that a selection of components can be made. In [Table 1](#) the parameters are specified for the SEPIC design of this thesis.

Specified parameters SEPIC	Values
PV-cell configuration	6-series
$V_{in(min)}$	$6*0.2 = 1.2V$
$V_{OC} = V_{in(max)}$	$6*0.68V = 4.08V$
$V_{out} = V_{battery}$	7.4V
V_{FWD}	0.35V
I_{out}	$V_{battery}/R_{load} = 0.37A$
f_{sw}	100kHz
Output voltage ripple	2%
Ripple current inductors	30%

Table 1: Parameters and assumptions used to design the SEPIC.

For the purpose of this theoretical design a 6-series connection of PV-cells is assumed. Therefore the minimum and maximum input voltage of the SEPIC is six times that of a single solar cell (Actually in this thesis later on higher order of series connections are used, therefore this design process could be optimised in the future, moreover in [subsection 8.2](#)). The output of the SEPIC has to be the same voltage level as the battery. For this theoretical design a 7.4V battery is assumed to be used.

The forward voltage drop of the diode was selected to be as low as possible. This resulted in the use of a Schottky diode. These diodes have an V_{FWD} in the range of 0.15-0.45V. The lowest available value for our project was 0.35V.

For the switching frequency a value of 100kHz is used. The switch will be operated by the PWM signal coming from the micro-controller. The Arduino Nano is capable of creating a PWM signal at this frequency.

The ripple allowances are chosen by rules of thumb [7].

In the following subsections all components of the SEPIC will be discussed and a possible value will be selected which will suit for the PV application.

5.1 Components

The SEPIC consists of various components; inductors, capacitors, a diode and a switch. These components need to be selected based on parameters for the converter for the solar drone project from [Table 1](#). In this section a description of all components will be given and described on how they are selected based on the specified parameters.

5.1.1 Inductor

The inductors in the SEPIC cause ripple currents due to charging and discharging. Choosing an inductor value is coherent to specifying the maximum ripple current of the inductor. A greater inductance value results in improvement of the efficiency of the converter but decreases the voltage ripple performance at the output. A good rule for choosing the inductance value according to [7] is allowing ripple current of approximately 20-40%. Therefore an approximate ripple of 30% is chosen for this project. This results in the following ripple current flowing in both inductor L1 and L2 of the same inductance:

$$\Delta I_L = I_{in} * 30\% = I_{out} * \frac{V_{out}}{V_{in(min)}} * 30\% \quad (5)$$

The inductance value for both inductors can then be calculated using the following equation(from [8]):

$$L1 = L2 = L = \frac{V_{in(min)}}{\Delta I_L * f_{sw}} * D_{max} \quad (6)$$

D_{max} is the maximum duty cycle needed by the converter. This is for a constant output voltage at the minimum input voltage. This results in an inductance value of $32\mu H$. In the theoretical design $47\mu H$ will be used as these inductors are easily accessible and are close enough to the calculated values. The peak currents of both inductors are given by:

$$I_{L1(peak)} = I_{out} * \frac{V_{out} + V_{FWD}}{V_{in(min)}} * (1 + \frac{30\%}{2}) \quad (7)$$

$$I_{L2(peak)} = I_{out} * (1 + \frac{30\%}{2}) \quad (8)$$

It is possible to wound both inductors L1 and L2 on the same core. Due to mutual inductance the value of the inductance in Equation 6 is replaced by 2L. This gives the following equation:

$$L1' = L2' = \frac{L}{2} = \frac{V_{in(min)}}{2 * \Delta I_L * f_{sw}} * D_{max} \quad (9)$$

5.1.2 Switch

As mentioned before the selection for the switch used is between a MOSFET and an IGBT. These switching elements both have their own characteristics. The characteristics on which they differ are due to for which conditions they are used. These conditions are; operating frequency, rated output power and voltage. Table 2 presents the preferred conditions for both switching elements according to [9].

	MOSFET	IGBT
Operating frequency [kHz]	>200	<20
Output power [W]	<500	>5000
voltage [V]	<250	>1000

Table 2: Preferred conditions under which a MOSFET and an IGBT perform [9].

These conditions are clearly visualised in Figure 5. For the solar drone project the operating voltage range is much below 250V which makes the MOSFET more favourable. This is also the case for the output power which will be below 500W for this project. Only the operating frequency will be in the undetermined range between 20 and 200kHz. The PWM frequency from the micro-controller will be 100kHz. Thus it can be concluded that the MOSFET is better suited for the solar drone project.

To make sure the micro-controller's control signal can actually turn on the MOSFET, the voltage level of the on signal needs to be greater than the gate-source threshold voltage V_{gs-th} . In case this is not possible a gate driver circuit is required to amplify this control signal. This gate driver circuit also acts as a isolation between the micro-controller and the MOSFET.

The MOSFET that will be used for both the theoretical and practical design will be the IRF530NS [10]. This

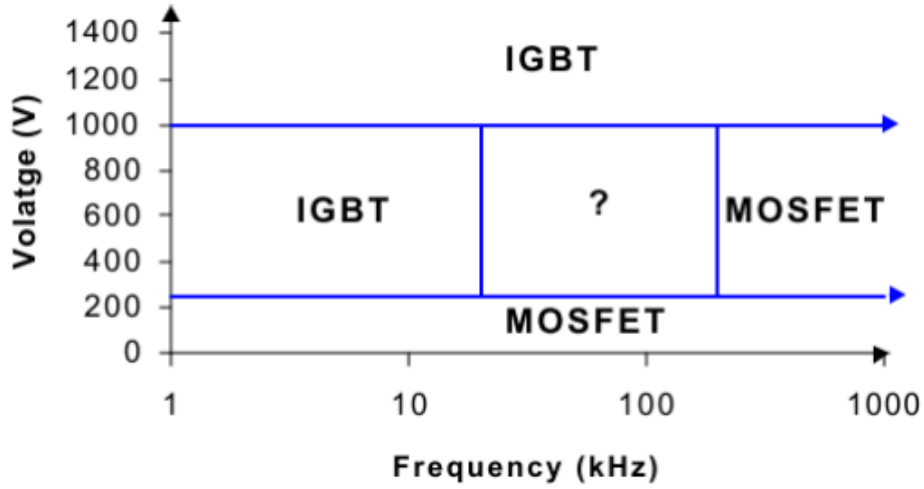


Figure 5: Preferred operating regions for the MOSFET and IGBT [9].

MOSFET is able to operate under all possible conditions and was easily accessible. These conditions are that the rated drain voltage for the MOSFET must be greater than $V_{in} + V_{out}$ and that the MOSFET is capable of handling the peak current it is exposed to:

$$I_{S1(peak)} = I_{L1(peak)} + I_{L2(peak)} \quad (10)$$

$$I_{S1(rms)} = I_{out} * \sqrt{((V_{out} + V_{in(min)}) * (V_{out} + V_{FWD})) / V_{in(min)}^2} \quad (11)$$

Ideally the switch operates instantaneous between the on and off state. But practically this is impossible and thus cause switching losses [11]. A higher switching frequency will increase the total switching loss due to it occurring more often. A charged capacitor connected to the gate driver circuit can help to decrease the time that the MOSFET needs to switch between states. This time can be calculated using the following equation according to [12]:

$$t_{on} = t_{off} = \frac{Q_{sw}}{I_G} \quad (12)$$

Where Q_{sw} is the gate switch charge [10] and I_G is the gate drive current.

For the IRF530NS MOSFET the turn-off and -on delay are specified in the data sheet [10]. The turn-off and -on delay are 35ns and 9.2ns respectively. The period of the PWM signal is 10 μ s. This implies that the switch delay time of the MOSFET is $\frac{35ns+9.2ns}{10\mu s} * 100\% = 0.442\%$ of the period, which is an acceptable small percentage, suitable for this project.

5.1.3 Diode

The SEPIC uses one diode. This diode must be chosen carefully to handle the peak current flow when the switch opens and must be able to handle the reverse voltage. According to [7] The diode peak current in a SEPIC converter is the same as the switch peak current $I_{S1(peak)}$ from Equation 10. The minimum peak reverse voltage the diode must endure the V_{RD1} . This is given in Equation 13.

$$V_{RD1} = V_{in(max)} + V_{out(max)} \quad (13)$$

These current flows and voltages correspond to the SEPIC circuit diagram depicted in [Figure 2](#). The output current multiplied by the voltage drop across the diode equals the power dissipation of the diode. This because the output current equals the average diode current. In order to minimise the efficiency loss Schottky diodes are recommended according to [\[7\]](#). As already mentioned in [section 5](#) a Schottky diode with a V_{FWD} of 0.35V was selected as this was the lowest possible forward voltage drop available.

5.1.4 Capacitor

There are two capacitors depicted in [Figure 2](#). A coupling capacitor C_s and output capacitor C_{out} . The coupling capacitor depends on the RMS current which is given in [Equation 14](#) [\[7\]](#).

$$I_{C_s(rms)} = I_{out} * \sqrt{\frac{V_{out} + V_{FWD}}{V_{in(min)}}} \quad (14)$$

The voltage rating of the coupling capacitor C_s has to be greater than the maximum input voltage of the SEPIC converter. Because the coupling capacitor voltage is approximately equal to V_{in} . The peak to peak ripple voltage on C_s (assuming no ESR(Equivalent Series Resistance)) is ([\[7\]](#)):

$$\Delta V_{C_s} = \frac{I_{out} * D_{max}}{C_s * f_{sw}}, \text{ (Assuming no ESR)} \quad (15)$$

In order to achieve this maximum voltage peak to peak ripple across the coupling capacitor the capacitance has to be greater than:

$$C_s = \frac{I_{out} * D_{max}}{\Delta V_{C_s} * f_{sw}}, \text{ (Assuming no ESR)} \quad (16)$$

A coupling capacitor of $22\mu F$ with a ESR value of $28m\Omega$ will be used at the simulation model and in practice [\[13\]](#).

The output capacitor C_{out} supplies the output current to the load when the inductor charges if the switch is closed. Therefore the output capacitor has to be able to handle the maximum RMS current. This is the same current from [Equation 14](#). The output capacitor controls the ripple voltage on the output of the converter. According to [\[7\]](#) it can be assumed that half of the ripple is caused by the ESR and the other half by the capacitance of the output capacitor itself. This ripple is shown in [Figure 6](#) and associated [Equation 17](#) and [Equation 19](#).

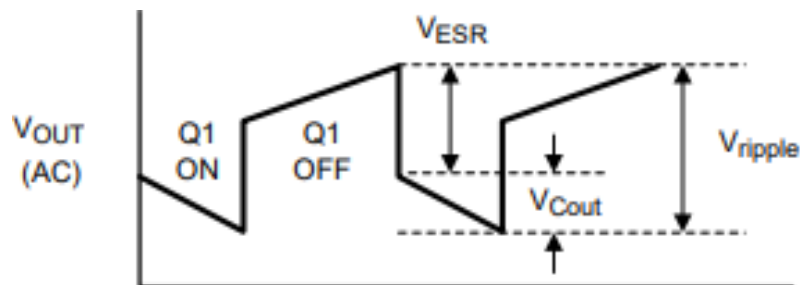


Figure 6: Output ripple voltage [\[7\]](#).

$$ESR_{C_{out}} \leq \frac{V_{ripple} * 0.5}{I_{L1(peak)} + I_{L2(peak)}} \quad (17)$$

$$I_{C_{out}(rms)} = I_{out} * \sqrt{(V_{out} + V_{FWD})/V_{in(min)}} \quad (18)$$

$$C_{out} \geq \frac{I_{out} * D}{V_{ripple} * 0.5 * f_{sw}} \quad (19)$$

The output capacitor must thus meet the requirements of a maximum ESR and a minimal capacitance to meet the wanted voltage ripple. This would be a maximum ESR of $32.8m\Omega$ and a minimum capacitance of $40.6\mu F$. A capacitor of $47\mu F$ and with $20m\Omega$ will be used at the simulation model and in practice [14].

5.2 Components values

An overview of all values calculated using the above equations are shown in Table 3. The calculated component values and ultimately used values are shown in Table 4.

D_{max}	81.15%
ΔI_L	0.4563A
$I_{L1(peak)}$	1.8320A
$I_{L2(peak)}$	0.4255A
$I_{S1(peak)}$	2.2575A
$I_{S1(rms)}$	1.7357A
V_{RD1}	11.48V
$I_{C_s(rms)}$	0.7677A
ΔV_{C_s}	0.1365V
$ESR_{C_{out}}$	$32.8m\Omega$
$I_{C_{out}(rms)}$	0.7677A

Table 3: (Using the parameter from Table 1).

Passive components SEPIC	Calculated values	Used values in simulation	ESR
L_1	$32.01\mu H$	$47\mu H$	0.09Ω
L_2	$32.01\mu H$	$47\mu H$	0.09Ω
C_{out}	$40.57\mu F$	$47\mu F$	0.02Ω
C_s	$20\mu F$	$22\mu F$	0.028Ω

Table 4: Passive component values for the SEPIC (Using the parameter from Table 1).

6 Simulink Simulation

With the use of the Simulink application from Matlab the SEPIC has been simulated before it was build. The simulation process will be done in three steps. First the SEPIC will be connected to a voltage source as input and has a resistive load as output. This setup is shown in Figure 7. This setup will be used to illustrate the working principle of the SEPIC.

The second setup will feature a simulated PV-array as input for the SEPIC and has a resistive load as output, in Figure 12 this setup is shown. This simulation will be done in two steps, first the MPP (Maximum Power Point) of the corresponding cell configuration and solar irradiance will be determined, this results in a specific duty cycle. After that the corresponding duty cycle will be applied to the gate of the MOSFET and then power efficiency measurement will be done.

For the third setup the resistive load will be replaced by a lithium-ion battery. This Simulink setup is shown in Figure 14. The full system can now be simulated. With this setup power efficiency measurements will be done and the current charging the battery will be simulated. The current flow will determine whether and how fast the battery is charging for the solar input conditions.

6.1 Simulating the working principle

The setup in Simulink used to simulate the working principle of the SEPIC is shown in Figure 7. The component values used in the simulation are the values from Table 4. The resistances in the schematic represent the ESR values. R_l is the load used for simulation and has a value of 20Ω .

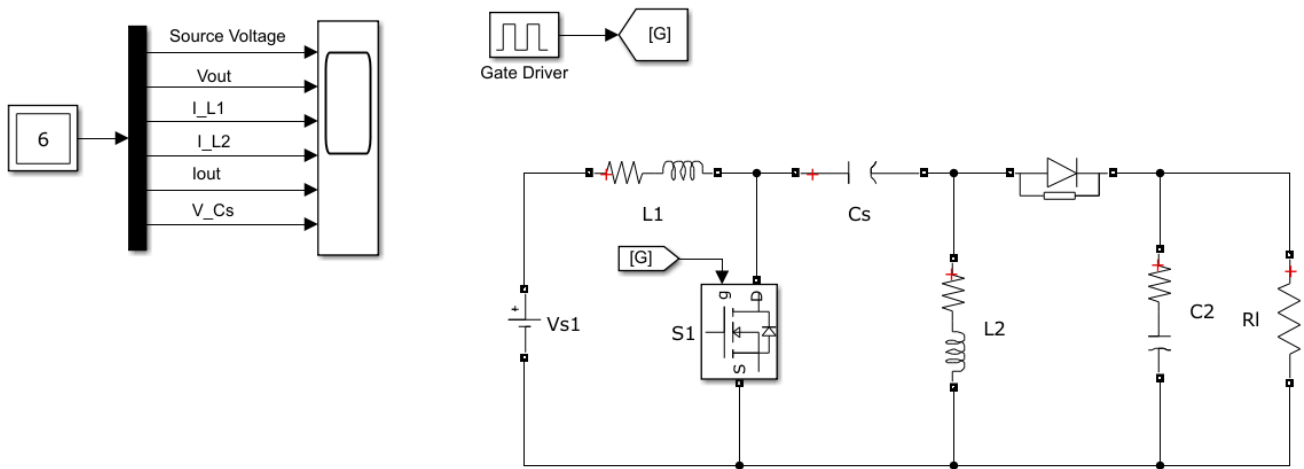


Figure 7: Simulink SEPIC setup 1

6.1.1 Load supply

From Figure 4 it can be concluded that energy is increasingly supplied to the resistive load during the off-state, PWM signal is low. In order to verify this the output voltage and current of the SEPIC is simulated using the Simulink setup in Figure 7. With those measurements the output power is also calculated. The plots of the output voltage & current and power are shown in Figure 8 and Figure 9 respectively. From these plots it can be concluded that indeed the load is supplied with increasing power during the off-state.

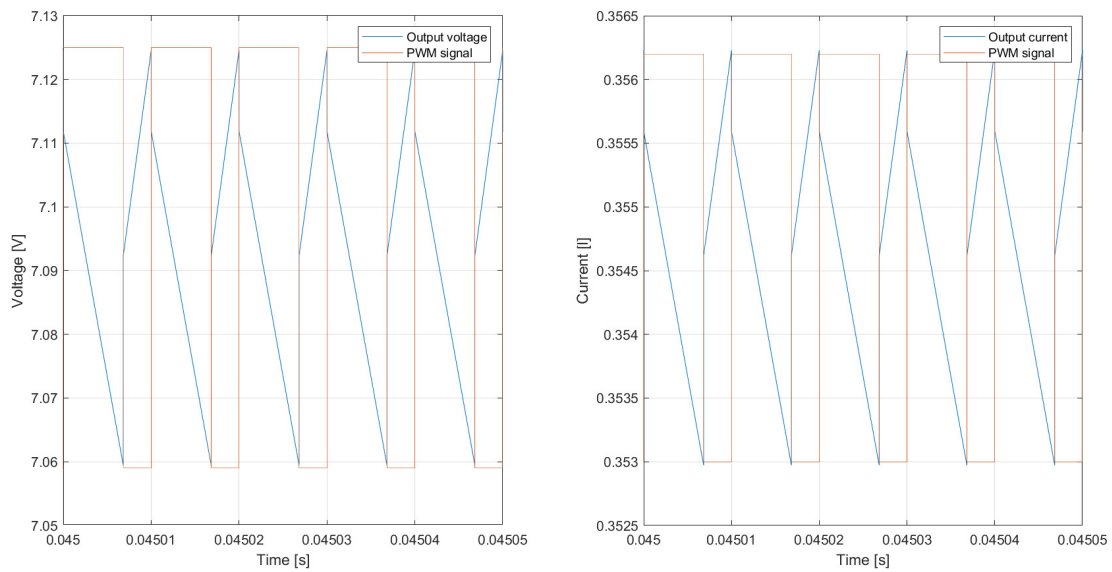


Figure 8: Output voltage and current of SEPIC plotted with corresponding PWM signal (Note that the PWM signal is adjusted to fit within the output voltage and current range, conditions: 3.6V input, 68.28% duty cycle)

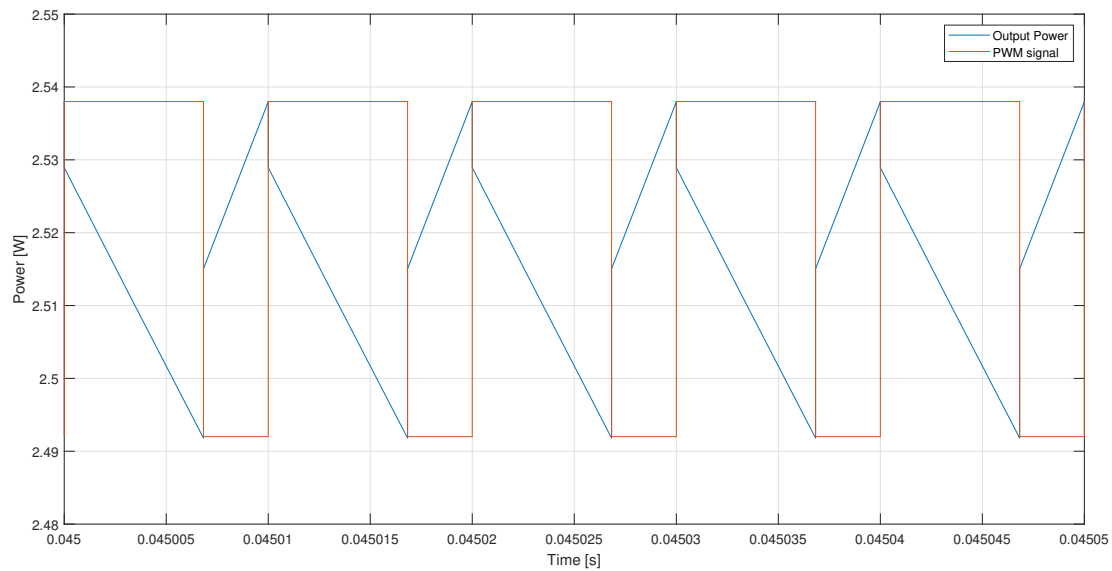


Figure 9: Output power of SEPIC plotted with corresponding PWM signal (Note that the PWM signal is adjusted to fit within the output power range, conditions: 3.6V input, 68.28% duty cycle)

6.1.2 Inductor current

It was already stated in [subsection 4.1.1](#) that during the on-state, PWM signal is high and MOSFET acts as a closed switch, both inductor currents are increasing in magnitude continuously due to inductors resist discontinuous

currents. The current through the second inductor is oriented in opposite direction of the current through L1, therefore becoming more negative. When the PWM signal becomes low and the SEPIC thus operates in the off-state, both inductors will discharge to supply the load. This is reflected in the output voltage plot in Figure 8. The inductor currents in both states are shown in Figure 10.

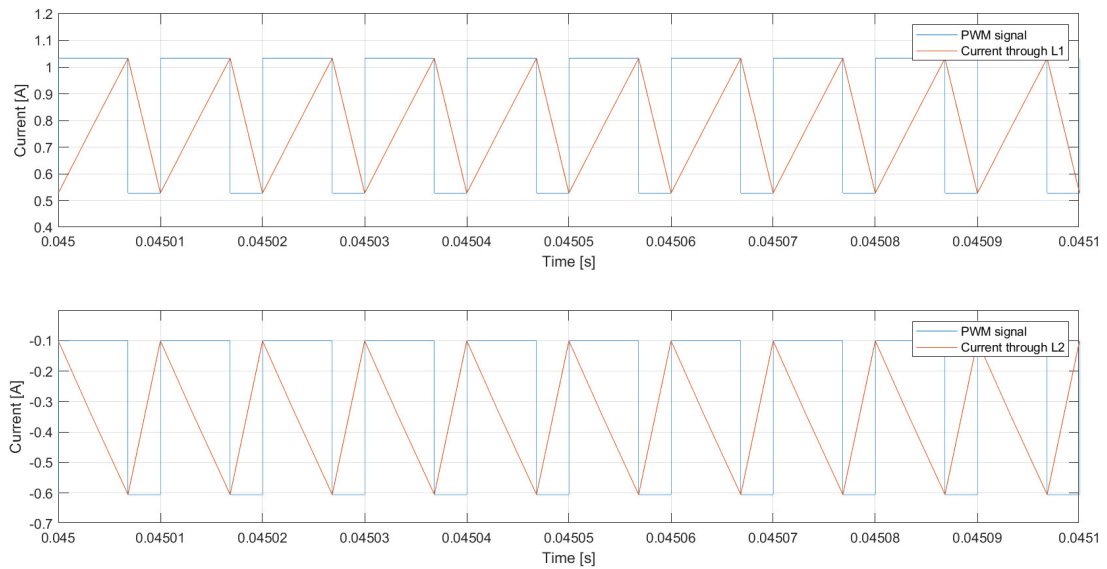


Figure 10: (1) Current through inductor L1 with corresponding PWM signal, (2) Current through inductor L2 with corresponding PWM signal (Note that the PWM signal is adjusted to fit within the inductor currents range, conditions: 3.6V input, 68.28% duty cycle)

6.1.3 Coupling capacitor voltage

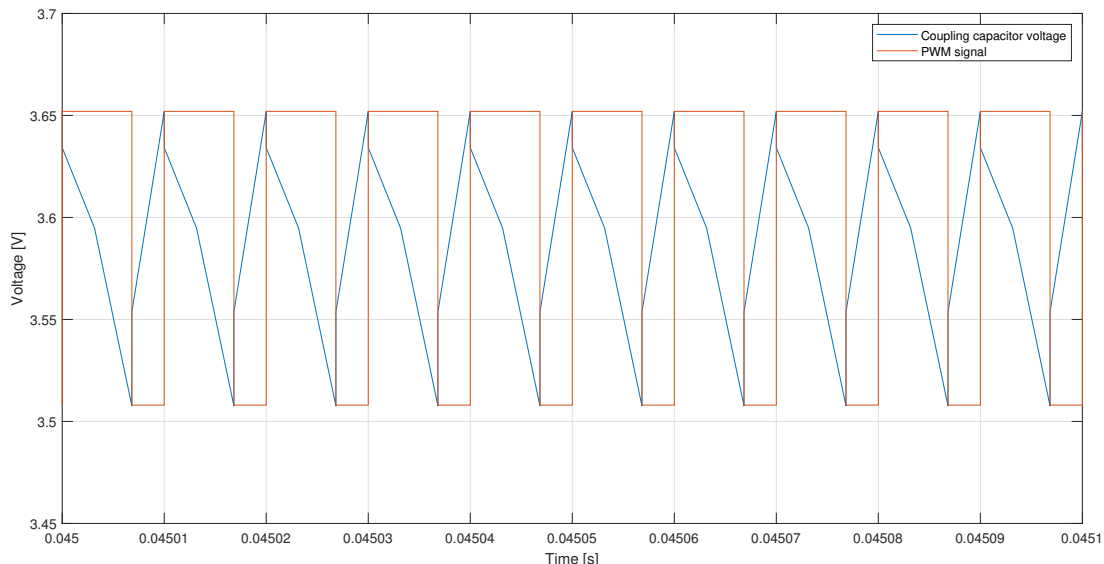


Figure 11: Coupling capacitor voltage of SEPIC plotted with corresponding PWM signal (Note that the PWM signal is adjusted to fit within the coupling capacitor voltage range, conditions: 3.6V input, 68.28% duty cycle)

In [subsubsection 4.1.1](#) it was stated that average coupling capacitor voltage V_{C_s} is equal to the input voltage of the converter. [Figure 11](#) shows the simulation of the voltage across the coupling capacitor for an input voltage of 3.6V. The average of this ripple voltage is exactly 3.6V therefore verifying the working principle.

6.2 Simulating with PV-cells and MPP

The second Simulink SEPIC setup is shown in [Figure 12](#). The voltage source in the previous setup is replaced by the simulation of a PV-array. This source can simulate any user-defined PV-cell and configuration. Measurements done with this setup are more representative as it simulates the conditions in which the converter has to operate in this project.

After the solar cell and configuration are set within the PV-array simulator block, the only two inputs are the operating temperature [$^{\circ}C$] and solar irradiance [W/m^2]. For the simulations in this project a fixed operating temperature of $25^{\circ}C$ is used and the solar irradiance will be a variable. The setup also contains a PWM Generator block. This block is designed to create a PWM signal with an increasing duty cycle from 0-100%. This is used to find the corresponding duty cycle to operate on the MPP.

Because solar cells are now used as power source, an input capacitor is used in order to increase the efficiency of the converter and get a more stable input power. This is due the frequent switching of the MOSFET, it causes the voltage output of the solar cells to drop to zero per period. This results in fluctuating power supply. The input capacitor stabilises the voltage output and thus the power output of the solar cells. For the input capacitor the same capacitance of $47\mu F$ is used as the output capacitor. A greater capacitance results in a lower voltage ripple but increases the rise time of the voltage.

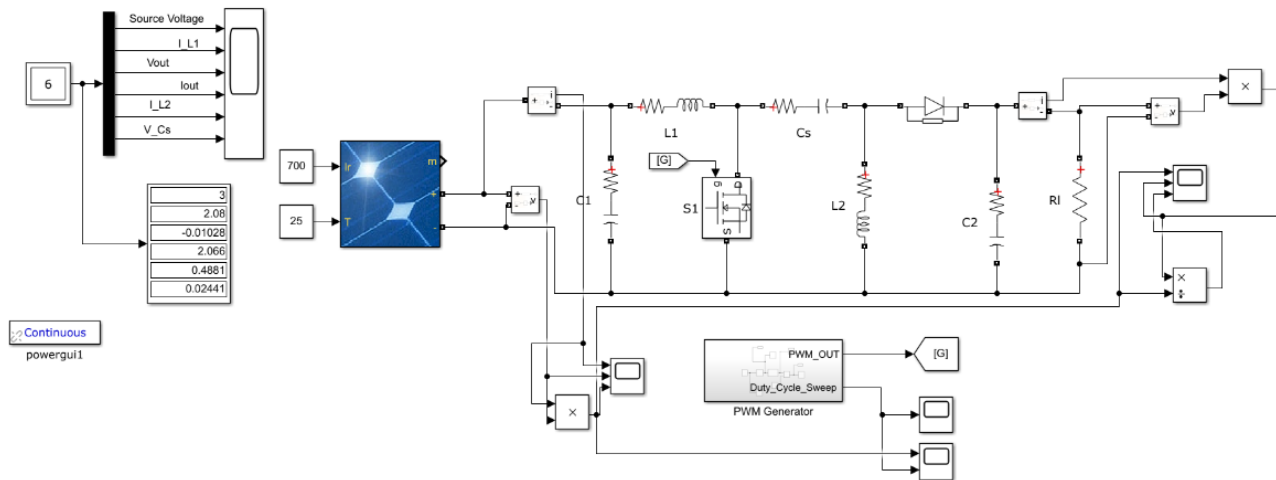


Figure 12: Simulink SEPIC setup 2.

6.2.1 PV-cells and MPP application

The simulated solar cells are set to match the solar cells that are going to be used [15] for the project as much as possible. The IV and PV curves are simulated for different solar irradiances and different series-configurations. No parallel strings are used as it would increase the input current of the SEPIC to a magnitude which the inductors is not able to cope. This would require bigger and heavier inductors. The trade-off for using these inductors is further elaborated in subsection 7.1. The small inductors used in the third SEPIC design are rated for 3.7A and saturate at 5.5A. From the IV curves it can be seen that at a solar irradiance of 700 W/m^2 the short circuit current is 4.2A and the MPP current is 4A. Therefore it must be closely monitored in practical measurements if the small inductors are capable of operating under these conditions.

The IV and PV curves for a 6-, 12- and 16-series connection are shown in Appendix A in Figure 18, Figure 19 and Figure 20 respectively. From the PV curves the maximum theoretical power per solar irradiance can be determined and its corresponding voltage V_{MPP} . The point on the curves where the system is operating is determined by the equivalent resistance of the circuit. By changing the duty cycle of the PWM signal supplied to the gate of the MOSFET this resistance value changes and therefore it is possible to operate at the MPP.

It can be concluded from the PV curves that the MPP changes with solar irradiance. These points are marked with a purple circle. The micro-controller subgroup will implement an algorithm that uses the voltage and current output of the solar cell to adjust the duty cycle of the PWM signal to keep track and keep operating on the MPP. This is called MPPT (Maximum Power Point Tracker). For the purpose of simulating the SEPIC the MPP per solar irradiance is determined by continuously increasing the duty cycle from 0 to 100% and measuring the power output of the PV-array block. An example is shown in Figure 13. Using the MPP duty cycles the SEPIC can on average draw 99.5% of the maximum theoretical power available from the PV-array.

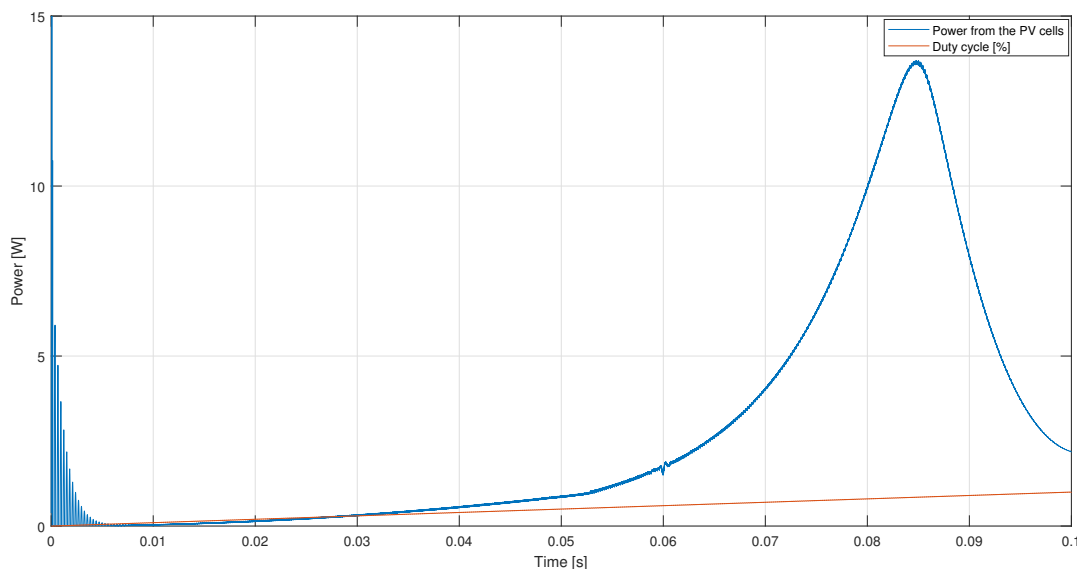


Figure 13: Power output of the PV-array block with corresponding duty cycle (conditions: 700 W/m^2 and 6-series configuration).

6.2.2 Output power

Using the MPP duty cycle per solar irradiance and cell-configuration the output power efficiency of the SEPIC can be simulated. All the simulation measurements can be found in [Appendix B](#). Note that for these measurements a resistive load of 20Ω is used. Other values will result in other duty cycle values for the MPP.

In order to charge a battery a current must flow in it. The greater the current the faster the battery charges. The lithium-ion battery has a rated charge current of 2A. Because the battery is rated 7.4V, this means that for the majority of the time the battery can only charge with a maximum power of 14.8W. From the measurements on a 6-series configuration ([Table 12](#)) it can be concluded that for solar irradiances below 700 W/m^2 a maximum of 10.95W is delivered to the battery. Thus with this configuration and assuming solar irradiances of maximum 700 W/m^2 the battery will never receive a higher charge current than its rated for.

For the 12- and 16-series configuration ([Table 13](#), [Table 14](#)) the maximum charge current will get exceeded for high solar irradiances. The micro-controller must measure the battery current flow and can anticipate on this. A solution would be to decrease the duty cycle until the output current of the SEPIC is 2A. This results in a trade-off, which amount of solar cells is most suitable to use in this project. Less solar cells will decrease the amount of power wasted and decrease the power consumption of the drone due to less weight. More solar cells will increase the time the battery is charging at full charge rate but at the cost of more energy consumption due to extra weight.

The SEPIC power efficiency in setup [Figure 12](#) is also simulated for all three configurations. In [Appendix B](#) the power efficiency of the 6-, 12- and 16-series configuration is shown per solar irradiance for a duty cycle sweep from 0-100% in [Figure 21](#), [Figure 22](#) and [Figure 23](#) respectively.

From these measurements one can see that for the simulated configurations and solar irradiances that the MPP duty cycle operating range is from 54.8-84.8%. Within this range it can be concluded that for a higher order of series configuration the SEPIC has a higher power efficiency. These power efficiency's are 88%, 91% and 93% for 6-, 12- and 16-series configuration respectively.

However every solar irradiance and configuration has its own MPP duty cycle. Only using the power efficiency on these specific duty cycles gives the following average power efficiency per configuration: 85%, 90% and 91% for 6-,

12- and 16-series configuration respectively. It can thus be concluded that the SEPIC could operate theoretically on an average power efficiency level of 90.7% for the simulated circumstances but has an average power efficiency level of 88.7% for operating on MPP for the simulated circumstances.

6.3 Simulating with a lithium-ion battery

With the third setup the resistive load is replaced with a lithium-ion battery. This setup is shown in Figure 14. The output capacitor stays in the system despite the use of a battery load. Simulations showed that the use of a capacitor parallel to the battery resulted in a lower voltage ripple at the cost of slight decrease of power efficiency. For charging a lithium-ion battery it is important that the voltage ripple of the battery is low. Higher ripples result in heating of the battery and reduce its lifetime.

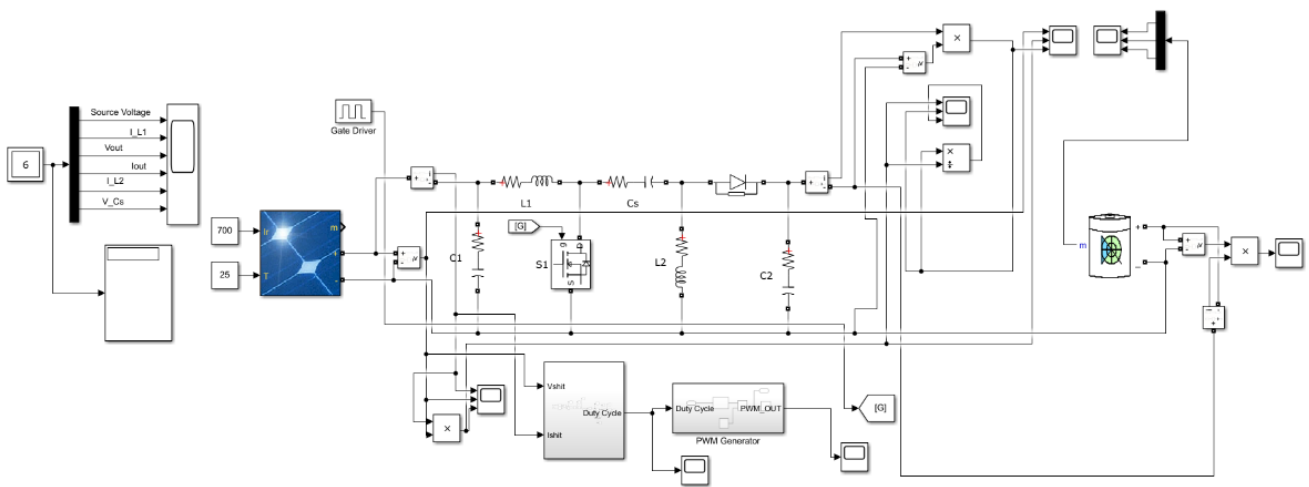


Figure 14: Simulink SEPIC setup 3.

Just like the previous setup first the MPP duty cycle per solar irradiance and PV-cell configuration is determined by a duty cycle sweep from 0-100%. This plot is shown in Appendix C, Figure 24. For all configurations and solar irradiances this is done. With all MPP duty cycles determined the SEPIC is simulated for all circumstances in MPP. These measurements can be found in Appendix C and are further elaborated and clarified in subsection 6.3.2.

6.3.1 Lithium-ion battery

Simulink has the ability to simulate a battery. In order to match the simulated battery to the lithium-ion battery used for the drone, the specifications of the battery are plugged into the battery block. These specifications are shown in Table 5. The battery block in Simulink can plot the characteristics of the simulated battery. This plot is shown in subsection C.1, Figure 25.

Type	Lithium-ion
Nominal voltage [V]	7.4
Rated capacity [mAh]	2000

Table 5: Characteristics of the simulated battery in Simulink.

It can be seen from the characteristics plot that the battery's voltage only has a great change when almost fully charged or discharged. Because the battery's voltage drops when almost discharged, the battery will be charged faster for the same amount of power delivered then when the battery is operating on its nominal voltage. The battery has a charge rate of 1C. This implies that the maximum charge current is $1C * 2000\text{mAh} = 2\text{A}$. Therefore high solar irradiances or a greater amount of solar cells used could transcribe this limit. If this is possible with the final configuration and irradiance circumstances, the micro-controller subgroup must measure the output current of the SEPIC and adjust the duty cycle so that the transferred power to the battery decreases.

6.3.2 Charging the battery

Ultimately the solar cells should deliver power to the battery. The most important factor is the current delivered to the battery. This determines the rate at which energy flows into the battery. Measurements on operating at MPP are shown in [Appendix C](#). The output power of the SEPIC is calculated different from the previous setup. There the output voltage and current were simply multiplied. This was possible as the output was connected to a resistive load. Now the output of the SEPIC is connected to a battery which is a energy source. The output power is now calculated using the following equation;

$$P_{out} = \frac{(SOC(t) - SOC(0)) * 7200C * V_{battery}}{t} \quad (20)$$

Where SOC is the state of charge of the battery expressed from 0-1. The 7200 Coulomb comes from the rated capacity of 2000mAh of the battery. Dividing the output power by the power extracted from the solar cells gives the efficiency of SEPIC operating at MPP. These efficiency's are shown in [Figure 15](#).

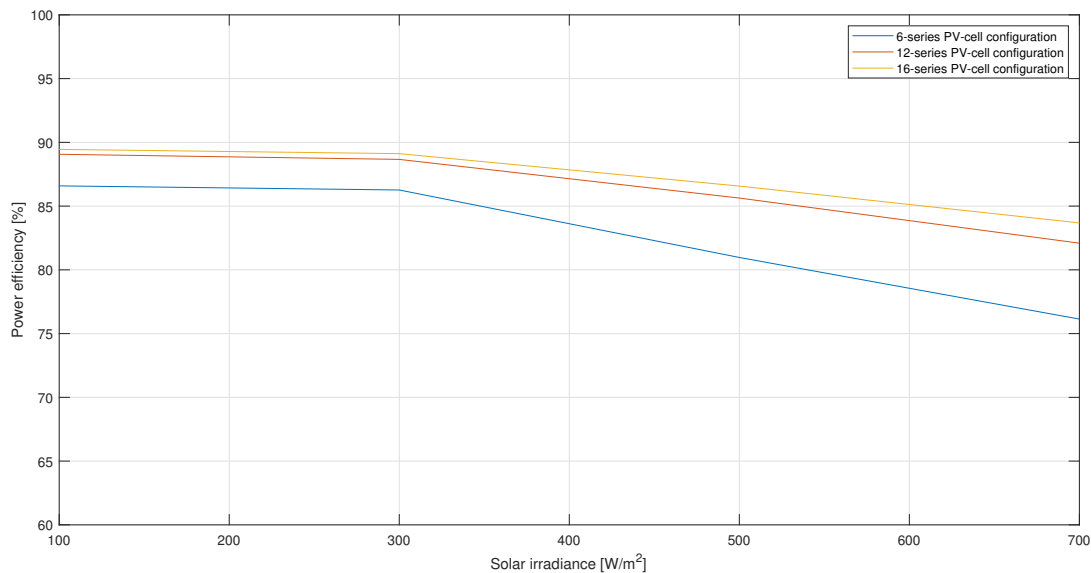


Figure 15: Power efficiency per solar irradiance for different PV-cell configurations under the circumstances of operating on the MPPT.

From this plot it can be concluded that a higher order of PV-cell series configuration increased the efficiency of the SEPIC operating at MPP, but for greater solar irradiances the efficiency for all configurations decreases. This is also reflected in the measurements of the charge rate and current flow of the battery. For increasing solar

irradiance the current flow and charge rate increase but with a decreased slope. This is the case for both current and charge rate because these are coherent. These plots can be found in [subsection C.5](#).

From the current flow measurements it can be seen that for a 12- and 16-series PV-cell configuration the 2A charge rating will get exceeded for solar irradiances greater than 480 and 350 W/m^2 respectively. For higher solar irradiances the duty cycle must be adjusted to keep operating on this 2A and possible energy will be lost. This heavily influences the design decisions of the power management group and results in a trade-off of between harvesting more energy or less mass and efficient use of energy.

The battery's voltage ripple plot in [Appendix C, Figure 29](#) shows that for the 6-series PV-cell configuration the ripple stays below the 2% specified in [section 5](#). For the 12-series this only holds for solar irradiances up to 600 W/m^2 and for 16-series up to 500 W/m^2 . In order to reduce this ripple, multiple capacitors in parallel could be used to increase the capacitance.

To conclude the simulation measurements of the SEPIC with the application of PV-cells and a lithium-ion battery, the average power efficiency of the converter under the circumstances of operating at MPP for different PV-cell configurations and solar irradiances are shown in [Table 6](#). As was already stated the power efficiency is greater for higher order of PV-cell series-configurations and decreases for higher solar irradiances. It can be concluded that the theoretical power efficiency of the designed SEPIC for PV-application is above 85% for a 12 or higher order of series configuration of PV-cells.

Power efficiency [%]	100 [W/m^2]	300 [W/m^2]	500 [W/m^2]	700 [W/m^2]	Average [%]
6-series PV-cell configuration	86.59	86.26	80.97	76.14	82.49
12-series PV-cell configuration	89.06	88.66	85.63	82.09	86.36
16-series PV-cell configuration	89.45	89.11	86.57	83.68	87.20

Table 6: Power efficiency per configuration and solar irradiance of the simulated SEPIC using a lithium-ion battery as load.

7 Practical Application

The first practical SEPIC was build with the use of other components than specified in [Table 4](#). The main difference were different ESR/DCR values than specified. In [Figure 16](#) the first practical design is shown. The ESR values of the capacitors used in this first converter are in the order of $1 - 4\Omega$. The high ESR values resulted in a very high output peak-to-peak voltage, this can be seen in [Appendix D](#), [Figure 30](#). Therefore measurements were cancelled and new capacitors were selected with a lower ESR ([Table 4](#)) in order to lower the ripple voltage. Also new inductors were selected with a lower DCR value to improve the power efficiency of the converter, however this resulted in larger size inductors and an increase in mass.



Figure 16: First SEPIC design (09-05-19).

With the newly selected components two new SEPIC converters are build and shown in [Figure 17](#). The second design (bottom in the figure) has both the new capacitors and inductors. The third design (top in the figure) is the same only using the old inductors from the first design. This is done because a trade-off need to be made between the use of inductors. The big inductors in the second design have a lower ESR value which results in a higher power efficiency, but these are bigger and heavier than the inductors used in the first and third design. Because this converter is used for a drone project, mass is a very important factor as it has a big impact on the energy consumption of the drone.

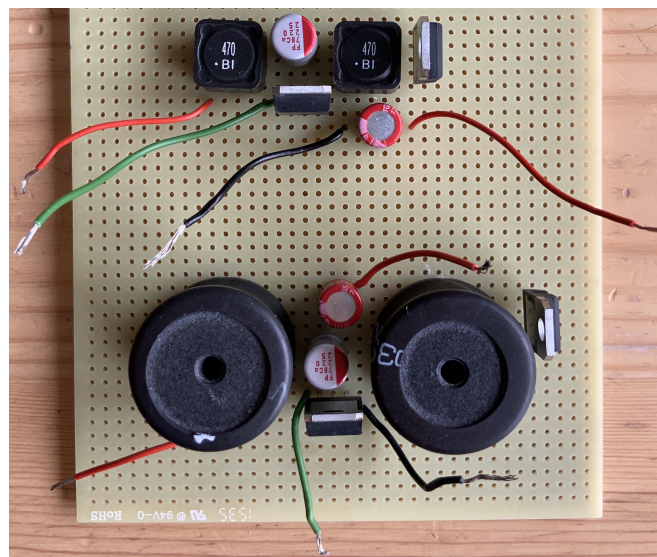


Figure 17: SEPIC design 2(bottom) and 3(top).

7.1 Inductor

When developing the SEPIC converter, different design steps were taken. One of them is the choice of components. As already discussed in [section 5](#), the SEPIC converter consist of many components, active and passive ones. One of the main components of the SEPIC are the 2 inductors. In [Table 4](#) the calculated- and the chosen values noted for the simulation are shown, these values are from their respective data-sheets. Not only the inductance is taking into account, also the direct current resistance (DCR) or ESR. DCR is the winding resistance which appears as a resistance in series with the inductor. It is the amount of resistance during direct current (DC). So both the inductance and the DCR must be taken into account for correct simulations and measurements.

An ideal inductor has a DCR of 0 Ω . In practice inductors do have a DCR value which varies from m Ω s up til a few Ω s (usually no greater than 4 Ω). A DCR close to zero results in a higher efficiency. Thus a DCR value which is close to zero is desirable for the inductors of the SEPIC converter.

Inductors with smaller DCR values do have a disadvantage. They are much heavier than inductors with a larger value. In order to keep the mass of the DC/DC converter as small as possible, however also as efficient as possible, a trade-off has to be made between mass and efficiency.

In [Figure 17](#) are 2 SEPIC designs shown.

	SEPIC top	SEPIC bottom
Inductance [μ H]	45.3	47.8
DCR [m Ω]	146	22
Mass [g]	3.9	37.8
Efficiency [%]	86.5	88.26

Table 7: Specifications Inductors.

As stated in [Table 7](#) the bottom inductor has a much lower DCR value than the bottom one. The following equation approximated the extra power which is needed per gram to keep the mass in the air (This equation is taken from the Power Management & Drone Design subgroup).

$$P_{solar} = 0.129 * m \quad (21)$$

[Table 7](#) shows that the mass of the bottom inductor is approximate 34 grams more than the bottom one. This extra mass has to be compensated in order to actually be more efficient. [Equation 22](#) shows how much every solar cell will approximately produce, (this equation is taken from the Power Management & Drone Design subgroup).

$$P_{solar} = 0.9756 * n \quad (22)$$

The final variable that is missing, is the efficiency per inductor size. Due to the lower DCR value, the top inductance will have a better efficiency and thus will need less solar panels to compensate for the weight. To calculate the efficiency for the small inductors, [Table 18](#) is used. An average of all the efficiency values per V_{in} by a load of 50 Ω is taken. The same is done for the bigger inductors, where [Table 20](#) is used.

Finally [Figure 32](#) in [Appendix G](#) shows that the top design is more efficient. Only after the utilisation of more than 255 panels will the bigger inductors with the lower DCR value be more efficient than the smaller inductors. In this project, a maximal amount of 20 PV-cells will be used, so the upper design is the better choice here for the overall project. Using the bottom design results in a better performance of the converter.

7.1.1 Coupled inductor

As stated in [subsection 5.1.1](#) it is possible to wound both inductors of the SEPIC on the same core. If a coupled inductor would be used, some space could be saved and the SEPIC converter could be made even smaller. The coupled inductor would have a mutual inductance with a value of 2L as stated in [Equation 9](#). Again a trade-off

has to be made and again it comes down between efficiency and mass.

The data-sheets of both inductors are stating that both inductors are ideal for SEPIC configurations. Both inductors have a high efficiency and excellent current handling [16] [17].

The coupled inductor required only for each winding half the value needed for two separate inductors [17]. This allows the choice of a part with a lower DCR. As stated in Table 8 the DCR value of the coupled inductor is less than those of the single inductors. Also there is only one DCR value for the coupled inductor instead of two times the DCR for the single inductors to take care of.

	2 Single inductors	1 coupled inductor
Inductance [μH]	45.3	33.6 or 134.4
DCR [$\text{m}\Omega$]	2*146	54
Mass [g]	7.8 (combined)	10.1

Table 8: Specifications of single inductors and coupled inductor

The amount of space that the inductors occupied, is twice the space as for the coupled inductor. The mass of the circuit-board is negligible, thus it comes down on mass of the coupled inductor and the total mass of the 2 separate inductors. The masses are noted in Table 8.

Both inductor values are sufficient for the operation of the SEPIC, see Table 4. Eventually the two single inductors were chosen. The decisive factor was the mass. The inductors turned out to be very efficient and high efficiency's were obtained during the measurements, see subsection F.1.

However afterwards the coupled inductor was the better choice. To hand in a little extra mass, probably better efficiency results could be obtained and a more compact SEPIC would be the result. Moreover this in the subsection 8.2.

7.2 MOSFET selection

For the first designs the IRF530NS MOSFET [10] was used as this MOSFET was available and has a gate threshold voltage of 2-4V which is lower than the high PWM signal coming from the micro-controller. Therefore the micro-controller is able to control the gate of the MOSFET.

In order to obtain a greater power efficiency of the SEPIC a second MOSFET was used, the CSD18536KCS [18]. This MOSFET was chosen based on lower switching times, lower drain-to-source on-resistance and a lower diode forward voltage. These specification of both components are shown in Table 9.

MOSFET specifications	IRF530NS[10]	CSD18536KCS[18]
Turn-on delay time [ns]	9.2	8
Turn-off delay time [ns]	35	23
Drain-to-source on-resistance [$\text{m}\Omega$]	90	1.7-2.2
Diode forward voltage [V]	1.3	0.9-1.0
Total gate charge [nC]	37	83-108

Table 9: Specifications of the IRF530NS [10] and CSD18536KCS [18] MOSFET.

The second SEPIC design (Figure 17) was measured for power efficiency using both MOSFETs. This was done using a voltage source as input and both 50Ω and 10Ω as resistive load. The gate of the MOSFET was controlled by a pulse generator. These power efficiency measurements for both the IRF530NS and CSD18536KCS can be found in Appendix E, Table 18 and Table 19 respectively.

From these measurements it can actually be concluded that the use of the IRF530NS MOSFET in the SEPIC results in an overall higher efficiency than with the CSD18536KCS MOSFET. This could be because the IRF530NS

MOSFET has a lower total gate charge. According to [19] a lower gate charge enables lower power loss. It also states that MOSFETs with lower drain-to-source on-resistance provides lower conduction losses at the cost of higher gate capacitance. Therefore the total gate charge of the CSD18536KCS MOSFET is greater.

In the case of our converter, the lower power loss outweighs the lower conduction loss, therefore the use of the IRF530NS MOSFET results in an overall higher power efficiency of the SEPIC. This MOSFET will therefore be used. Power efficiency measurements of the SEPIC were done with this MOSFET using a voltage source as input and sweeping the duty cycle of the PWM signal supplied by the function generator.

The measurements give an overall idea of the SEPIC but note the use of a voltage source as input power supply. This is not the same as the output of a PV-cell and therefore these measurements may differ from PV-application. The measurements and power efficiency plot can be found in subsection F.1 in Table 21 and Figure 31 respectively.

7.2.1 Heatsink

All the electrical losses from the MOSFETS and diode are converted into heat. If these electrical components are getting too hot, they will not operate properly and the overall efficiency will decrease. For example the gate threshold voltage of the MOSFET will decrease when the temperature increases. [20]

In order to lose this heat more efficiently, a heatsink can be used. A heatsink is a passive heat exchanger that transfers heat. Moreover a heatsink is designed to maximise its surface area in order to maximise the heat exchange. Typically is a heatsink a metallic part which can be attached to a device, in this case to the MOSFET or diode, releasing energy in the form of heat. Namely to dissipate heat to its surrounding in order to prevent the device overheating and this results in a device which is functioning at optimal levels. [21]

7.2.1.1 Practical use of Heatsink

There are a couple parameters which determine the performance of a heatsink. For example the geometry, material and interface with the device are very important. To satisfy all these parameters, a aluminium 'cap' with a U shape is used for the SEPIC converter. The cap is put over the MOSFET to maximise the interface with the device in order for maximal heat exchange. Because of the U shape, the total area is increased and this results in larger heat exchange.

An alternative for the U shape, is a metal 'plate' that is put on the bottom of the circuit-board. The cap however functioned well enough for the heat amount that the MOSFET produced. The Schottky diode doesn't produce a lot of heat so no heatsink is used on the component. This applies for all the other (passive) components as well.

In order for the solar drone to operate in all different kind of situations, it must be able to operate well for a very high radiant intensity. In this case, a greater current will flow through the SEPIC and more heat will be produced. In this case a more advanced heatsink must be applied.

7.3 Capacitors

Ideal capacitors do not consume energy. It first stores and after that it releases the same amount of energy. Just like the inductors, the capacitors do have a resistance which is the equivalent series resistance (ESR). ESR is a resistive component that causes some energy to be lost in form of heat, [22]. These values are stated in Table 10. Another form of resistance is the equivalent series inductance (ESL). ESL causes a magnetic field to occur in devices. The magnetic field has influences on the current [22]. ESL occurs in high frequencies circuits. The frequency that the micro-controller maintains results in a negligible ESL.

	C_{in}	C_s	C_{out}
Capacitance [μF]	46.4	21.2	46.4
ESR [$\text{m}\Omega$]	96.4	130	96.4

Table 10: Specifications Capacitors, the ESR values are measured and differ from their data sheets.

As already stated in [subsection 5.1.4](#) the input-capacitance is the same as the output capacitance. For the coupling capacitor C_s a different capacitor is used see [Equation 16](#). These capacitors satisfy the restrictions from [Table 4](#) and were also the capacitors with the lowest available ESR values, resulting in the best performance. The output capacitor is used even when the battery is attached. As [subsection 6.3](#) already stated, the use of a capacitor parallel results in a lower voltage ripple at the cost of a slightly loss in power efficiency. However a high voltage ripple results in heating of the battery and a reducing of it's life-time. Due to the small ESR value is the decrease in efficiency very small.

7.4 Measurements & Results

With the third SEPIC design shown in [Figure 17](#) the measurements were execute. As was already mentioned in the simulation chapter, an input capacitor was added to the design in order to stabilise the power extracted from the PV-array and increase the overall extracted power. For the measurements the SEPIC was connected to a 12-series PV-array and a pulse generator.

Measurements were done for three different solar irradiances that are exposed to the PV-array. This was done using a solar box available in the Solar Lab in the Tellegen Hall of TU Delft. In [Appendix H, Figure 33](#) the solar box with PV-array is shown and the solar irradiance meter used in [Figure 34](#). For both a resistive load of 20Ω and a lithium-ion battery as load measurements are done. Results are shown in [subsection H.1](#) and [subsection H.2](#) respectively.

The measurements done with the resistive load, did give an indication of what the maximum output power could be for different solar irradiances. Because, as was already stated in [subsection 6.2.2](#), the maximum charge current of the battery 2A. Greater current could damage the battery severely.

From [Figure 35](#) it can be concluded that the power extracted from the PV-array at a solar irradiance of $535 W/m^2$ is at MPP 7.5W. Therefore a lithium-ion battery with a rated voltage of 7.4V can never receive a charge current greater than 2A from the PV-array at this solar irradiance.

Most interesting for this project are the measurements with the lithium-ion battery as load. In [Figure 38](#) the power efficiency of the converter is shown for different solar irradiances. From the simulation power efficiency plot in [Figure 15](#) it was concluded that for greater solar irradiances, the power efficiency of SEPIC decreased. This is also reflected in the practical measurements.

In [Figure 38](#) the MPP per solar irradiance is indicated with a '+'. These show that for a greater solar irradiance the power efficiency of the SEPIC decreased operating at MPP.

Furthermore it can be concluded that the average power efficiency of the SEPIC operating at MPP for solar irradiance between 280 and $535 W/m^2$ is 82.9%. The MPP power efficiency values of [Table 25](#), [Table 26](#) and [Table 27](#) are shown in [Table 11](#). These values are quite similar to those of the simulations in [Table 6](#).

From the same measurements can concluded that the maximum charge rating of the battery is not exceeded. The maximum current measured flowing into the battery is 0.846A for a solar irradiance of $535 W/m^2$ and the maximum charge rating of the battery is 2A. Thus even for double the solar irradiance the maximum charge rating of the battery will not be exceeded because the efficiency will also decrease for increasing solar irradiance.

Power efficiency [%]	280 [W/m^2]	430 [W/m^2]	535 [W/m^2]	Average [%]
12-series PV-cell configuration	85.641	81.831	81.202	82.9

Table 11: Power efficiency per solar irradiance of the practical SEPIC using a lithium-ion battery as load.

8 Conclusion and Future Work

After eight weeks we succeeded in designing, simulating and build a converter that is capable of charging a battery with a PV-array as input power source operating at MPP. In order to determine if this sub-project was successful the results of this thesis will be evaluated using the requirements set in [section 2](#).

8.1 Conclusion

The first requirement was that the DC/DC converter had to be able to be controlled by the micro-controller. In [subsection 7.2](#) it was stated that in order to control the converter, the gate threshold voltage $V_{GS(th)}$ of the used MOSFET must be lower than the high PWM signal coming from the micro-controller. The IRF530NS MOSFET [10] is used for this project which has a gate threshold voltage of 2-4V which is lower than the high PWM signal coming from the Arduino micro-controller used by the Micro-controller subgroup for the project. Therefore the first requirement is met.

To meet the second requirement of the converter the current flow into the battery cannot exceed the maximum charge rating of the battery thus guarantee safe charging. From the practical measurements described in [subsection 7.4](#) and its results in [subsection H.2](#), it shows that for the greatest solar irradiance of 535 W/m^2 the converter was exposed to the maximum current flow into the battery was 0.846A (These measurement are with twelve PV-cells in series). The maximum charge rating of the battery used is 2A. In order to exceed this rating at least double the solar irradiance is needed. Then again measurements also showed that for greater solar irradiances the efficiency of the converter decreased. Thus for solar irradiances below 1100 W/m^2 safe charging of the battery is guaranteed, therefore satisfying the second requirement.

The third and last requirement of the converter is that it has an overall power efficiency of 85% operating at MPP. From the power efficiency results of the practical measurements shown in [Table 11](#), it was concluded that the overall power efficiency of the converter is 82.9% operating at MPP for solar irradiances between 280 and 535 W/m^2 . It was also concluded that lower solar irradiances resulted in an increase in power efficiency, therefore measurements below 280 W/m^2 would have increased the overall power efficiency but the same can be said about measurements with solar irradiances greater than 535 W/m^2 . Thus eventually the last requirement is not satisfied.

8.2 Future Work

While the results that we obtained do satisfy with two of the three requirements that are stated in [section 2](#), there are some improvements in terms of efficiency, that can be obtained in the future.

- Instead of a Schottky diode, a synchronous MOSFET could be used. These MOSFET's behave as a resistance and the result is a much lower forward voltage drop thus resulting in a larger power efficiency.
- As already stated in [subsection 7.1](#), a coupled inductor can replace the 2 single inductors that are currently used in the SEPIC. A coupled inductor hands in a little extra weight, however the DCR values are much lower. The lower DCR value results in a greater efficiency.
- In the end a 20 cell-configuration is used. If this was specified from the start, a more specific design could have been made in order to obtain a greater power efficiency of the SEPIC operating at MPP. Also with the knowledge gained throughout the project we are able to better specify the design parameters of the SEPIC.
- During the project the amount of mass was always taken into account. If efficiency of the converter was the most important objective, heavier components with a lower DCR value could have been used and a better efficiency could have been achieved.
- Instead of a micro-controller as input for the PWM signal, a boost driver could be used (LM2577). In this case a steadier output voltage could be maintained however this would replace the MPPT algorithm.

References

- [1] Ngo, Tuan & Biricik, Samet. (2017). *Nonlinear Control Methods for Single-Ended Primary-Inductor Power Converters*.
- [2] Babaei, E., & Mahmoodieh, M.E.S., (2014) Analysis and investigation of energy transmission process in different operating modes of Sepic converter. *IET Power Electronics* 1-2. 10.1049/iet-pel.2013.0402
- [3] S. J. Chiang, H. Shieh and M. Chen, *Modeling and Control of PV Charger System With SEPIC Converter*, in IEEE Transactions on Industrial Electronics, vol. 56, no. 11, pp. 4344-4353, Nov. 2009.doi: 10.1109/TIE.2008.2005144
- [4] Texas Instruments (2018). *TPS61500 SEPIC Configuration* (SLVA904). Retrieved from Texas Instruments website: <http://www.ti.com/lit/an/slva904/slva904.pdf>
- [5] Texas Instruments (2019). *Switching regulator fundamentals* (SNVA559C). Retrieved from Texas Instruments website: <http://www.ti.com/lit/an/snva559c/snva559c.pdf>
- [6] Single-ended primary-inductor converter. (n.d.). In *Wikipedia*. Retrieved May 9, 2019, from https://en.wikipedia.org/wiki/Single-ended_primary-inductor_converter
- [7] Texas Instruments (2013). *AN-1484 Designing A SEPIC Converter* (SNVA168E). Retrieved from Texas Instruments website: <http://www.ti.com/lit/an/snva168e/snva168e.pdf>
- [8] Sharp, G. (2014). *Sepic Converter Design and Operation* (n.d.). Retrieved from WPI (Worcester Polytechnic Institute) website: https://web.wpi.edu/Pubs/E-project/Available/E-project-050114-131841/unrestricted/SEPIC_MQP_Final_Report.pdf
- [9] Electronic Design. (2015). IGBTs Or MOSFETs: Which Is Better For Your Design?. Retrieved April 25, 2019, from <https://www.electronicdesign.com/datasheet/igbts-or-mosfets-which-better-your-design-pdf-download>
- [10] International Rectifier, *IRF530NS/IRF530NL*, PD-91352B datasheet, April 2002.
- [11] Graovac, D., Purschel, M., & Kiep, A. (2006). MOSFET power losses calculation using the data-sheet parameters. *Infineon application note, 1*. Retrieved April 29, 2019, from [Researchgate.net](https://www.researchgate.net)
- [12] Z. J. Shen, Y. Xiong, X. Cheng, Y. Fu and P. Kumar. (2006). Power MOSFET Switching Loss Analysis: A New Insight. *Conference Record of the 2006 IEEE Industry Applications Conference Forty-First IAS Annual Meeting, Tampa, FL*, pp. 1438-1442. doi: 10.1109/IAS.2006.256719 <http://ieeexplore.ieee.org/stamp/stamp.jsp?tp=&arnumber=4025406&isnumber=4025345>
- [13] Nichicon, *RNS1E220MDN1 datasheet*. <https://nl.mouser.com/datasheet/2/445/870025574002-540520.pdf>
- [14] Würth Electronics, *WCAP-PTG5 datasheet*, November 2014. <https://nl.mouser.com/datasheet/2/445/870025574002-540520.pdf> <https://nl.mouser.com/datasheet/2/445/870025574002-540520.pdf>
- [15] SunPower Corporation, *C60 SOLAR CELL MONO CRYSTALLINE SILICON*, Document #001-66352, November 2010.
- [16] TT electronics plc, *Magnetics Shielded Surface Mount Inductors*, MODELS HM78D1210XXXMLF datasheet, Rev. 03 8.17
- [17] Coilcraft, *Coupled Inductors*, MSD1514 datasheet, Revised 05/06/16.
- [18] Texas Instruments, *CSD18536KCS 60 V N-Channel NexFET™ Power MOSFET*, SLPS532A datasheet, March 2015, revised December 2017.

-
- [19] Texas Instruments (2016). *MOSFET power losses and how they affect power-supply efficiency* (SLYT664). Retrieved from Texas Instruments website: <http://www.ti.com/lit/an/slyt664/slyt664.pdf>
- [20] Power MOSFET Basics (2015) *Understanding the Turn-On Process* Application Note AN850. Retrieved from VISHAY website: <https://www.vishay.com/docs/68214/turnonprocess.pdf>
- [21] Radian.(n.d.).Radianheatsinks. From <https://www.radianheatsinks.com/heatsink/>
- [22] EPCI European passive components institute. (n.d.). Effects of ESL on the performance of capacitors. Retrieved November 7,2017, from <https://passive-components.eu/effects-of-esl-on-the-performance-of-capacitors/>

9 Appendices

A PV- and IV-Curves of the Simulink PV-Array Block

A.1 6-series configuration

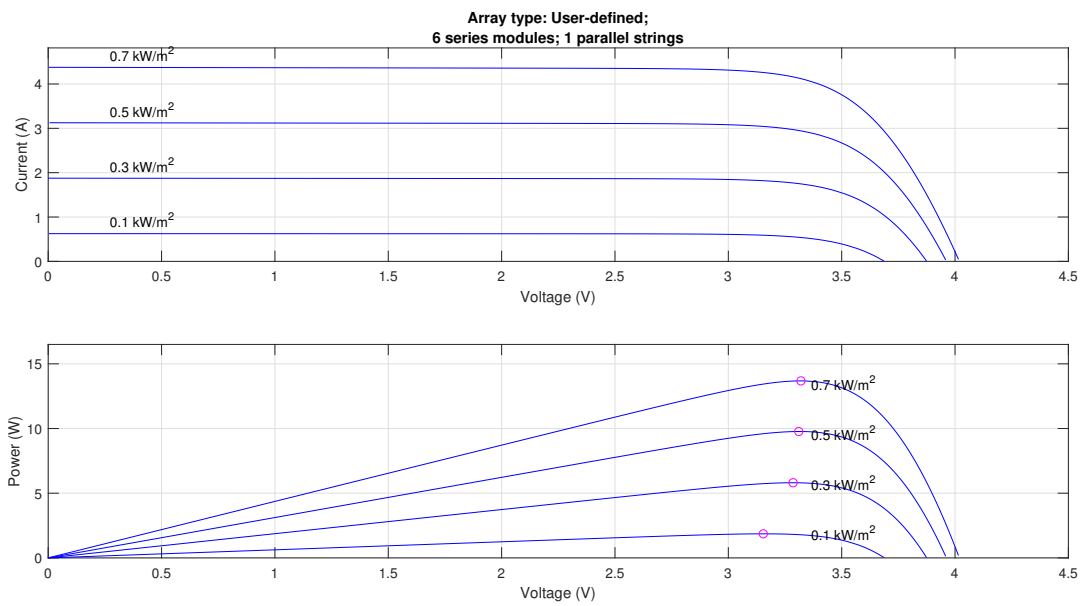


Figure 18: (1) IV curve, (2) PV curve, of a 6-series solar cell configuration per solar irradiance [W/m^2] [15].

A.2 12-series configuration

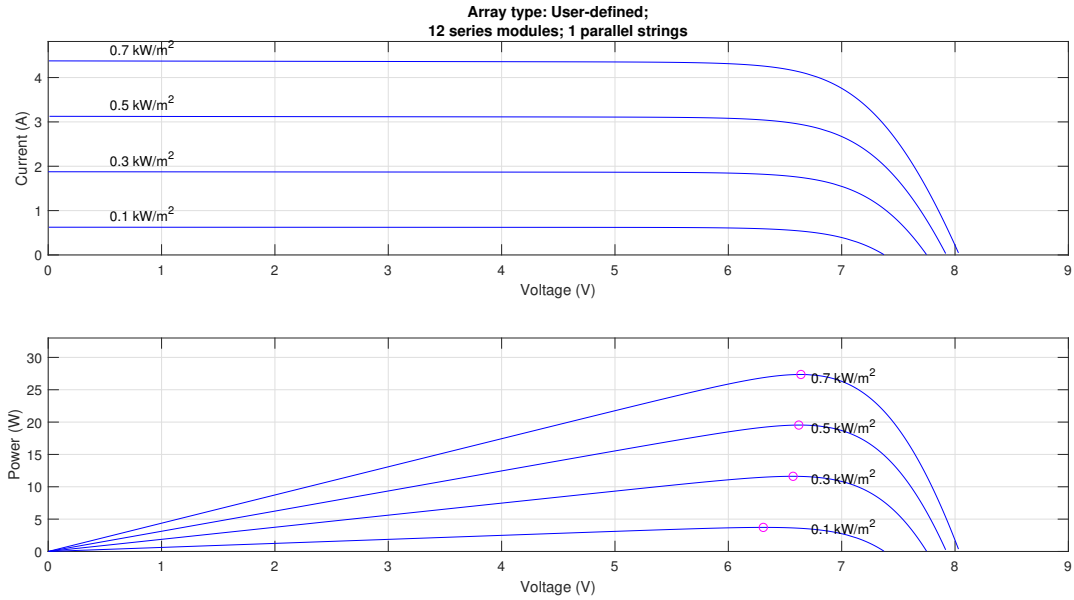


Figure 19: (1) IV curve, (2) PV curve, of a 12-series solar cell configuration per solar irradiance [W/m^2] [15].

A.3 16-series configuration

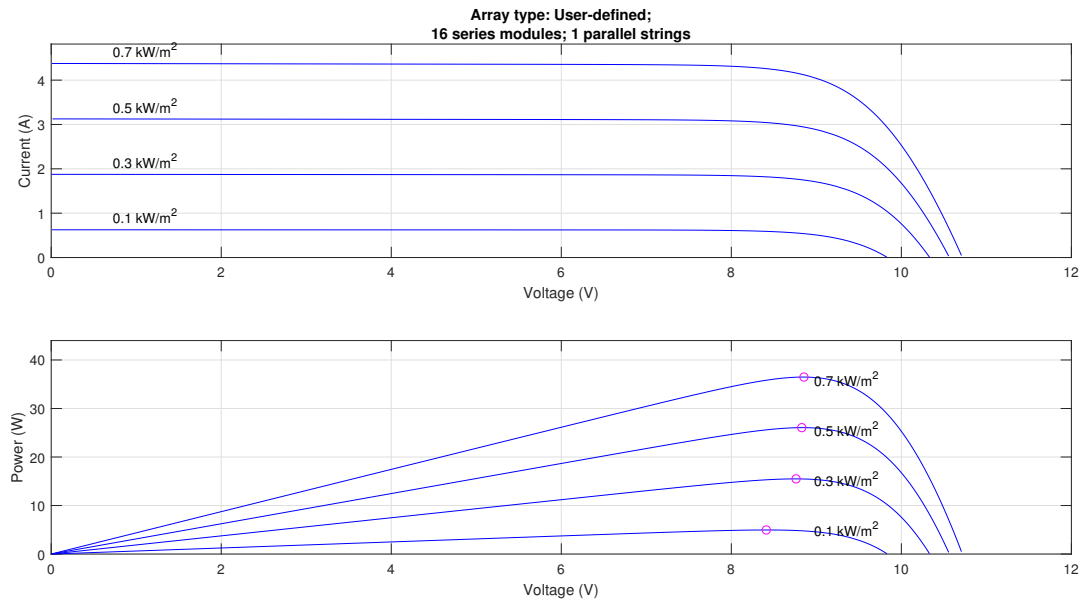


Figure 20: (1) IV curve, (2) PV curve, of a 16-series solar cell configuration per solar irradiance [W/m^2] [15].

B Simulink Simulation Results with PV Cells and MPP

B.1 6-series configuration

6-series configuration				
Irradiance [W/m^2]	100	300	500	700
$V_{in,mpp}$ [V]	3.154	3.286	3.311	3.320
$P_{in,mpp}$ [W]	1.860	5.809	9.770	13.680
$V_{in,result}$ [V]	3.107	3.265	3.273	3.290
$P_{in,result}$ [W]	1.855	5.807	9.756	13.680
$I_{in} = I_{L1}$ [A]	0.597	1.779	2.981	4.158
Duty cycle MPP [%]	67.0	77.7	82.2	84.8
$P_{out,result}$ [W]	1.645	5.071	8.176	10.95
$P_{in,efficiency}$ [%]	99.731	99.966	99.857	100.00
$P_{out,efficiency}$ [%]	88.679	87.326	83.805	80.044
Battery voltage rating [V]	7.4	7.4	7.4	7.4
I_{out} [A]	0.222	0.685	1.105	1.480

Table 12: Simulink measurement of the SEPIC for PV-application of a 6-series configuration.

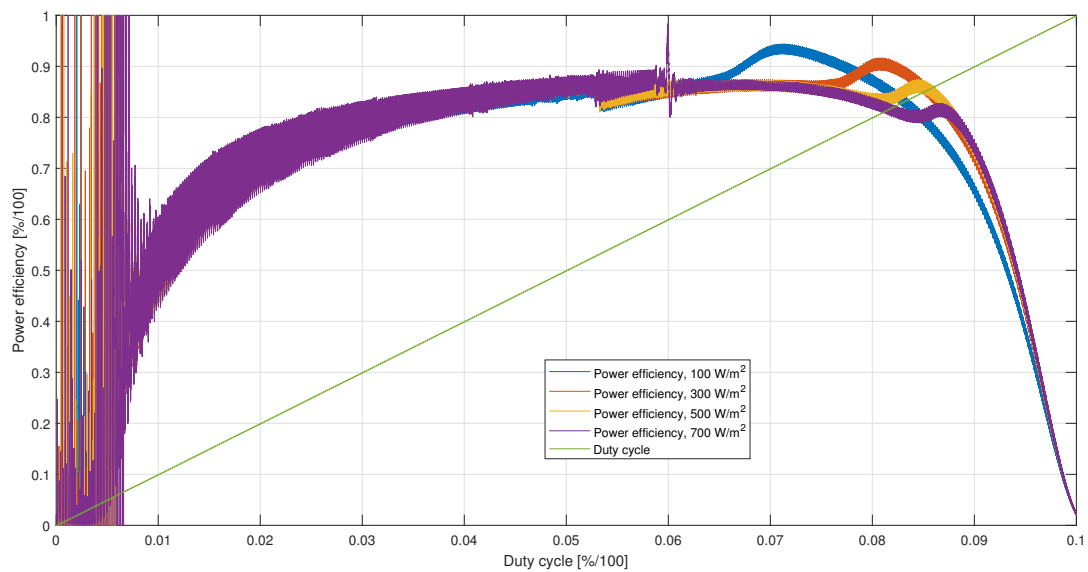


Figure 21: SEPIC power efficiency for a duty cycle sweep per solar irradiance for a 6-series PV cell configuration.

B.2 12-series configuration

12-series configuration Irradiance [W/m^2]	100	300	500	700
$V_{in,mpp}$ [V]	6.308	6.571	6.622	6.640
$P_{in,mpp}$ [W]	3.720	11.620	19.540	27.360
$V_{in,result}$ [V]	6.226	6.512	6.596	6.625
$P_{in,result}$ [W]	3.712	11.600	19.530	27.360
$I_{in} = I_{L_1}$ [A]	0.596	1.781	2.961	4.130
Duty cycle MPP [%]	58.4	70.6	75.7	78.8
$P_{out,result}$ [W]	3.376	10.580	17.530	24.130
$P_{in,efficiency}$ [%]	99.785	99.828	99.949	100.0
$P_{out,efficiency}$ [%]	90.948	91.207	89.759	88.194
Battery voltage rating [V]	7.4	7.4	7.4	7.4
I_{out} [A]	0.456	1.430	2.369	3.261

Table 13: Simulink measurement of the SEPIC for PV-application of a 12-series configuration.

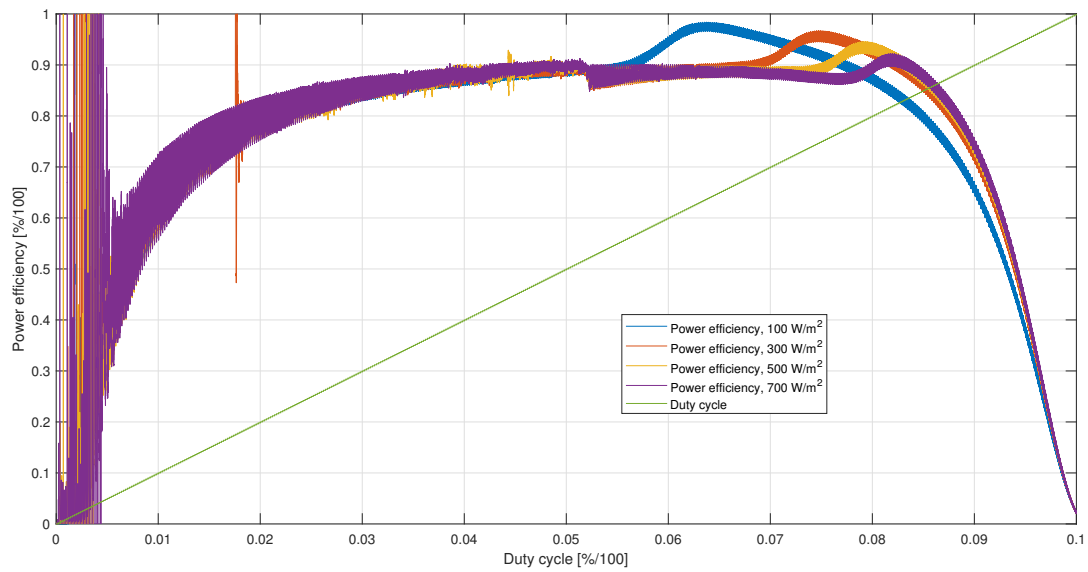


Figure 22: SEPIC power efficiency for a duty cycle sweep per solar irradiance for a 12-series PV cell configuration.

B.3 16-series configuration

16-series configuration Irradiance [W/m^2]	100	300	500	700
$V_{in,mpp}$ [V]	8.411	8.762	8.829	8.854
$P_{in,mpp}$ [W]	4.961	15.490	26.050	36.480
$V_{in,result}$ [V]	8.270	8.657	8.769	8.764
$P_{in,result}$ [W]	4.944	15.460	26.030	36.450
$I_{in} = I_{L_1}$ [A]	0.598	1.786	2.968	4.159
Duty cycle MPP [%]	54.8	67.4	72.8	76.2
$P_{out,result}$ [W]	4.513	14.240	23.740	32.780
$P_{in,efficiency}$ [%]	99.657	99.806	99.923	99.918
$P_{out,efficiency}$ [%]	91.282	92.109	91.202	89.931
Battery voltage rating [V]	7.4	7.4	7.4	7.4
I_{out} [A]	0.610	1.924	3.208	4.430

Table 14: Simulink measurement of the SEPIC for PV-application of a 16-series configuration.

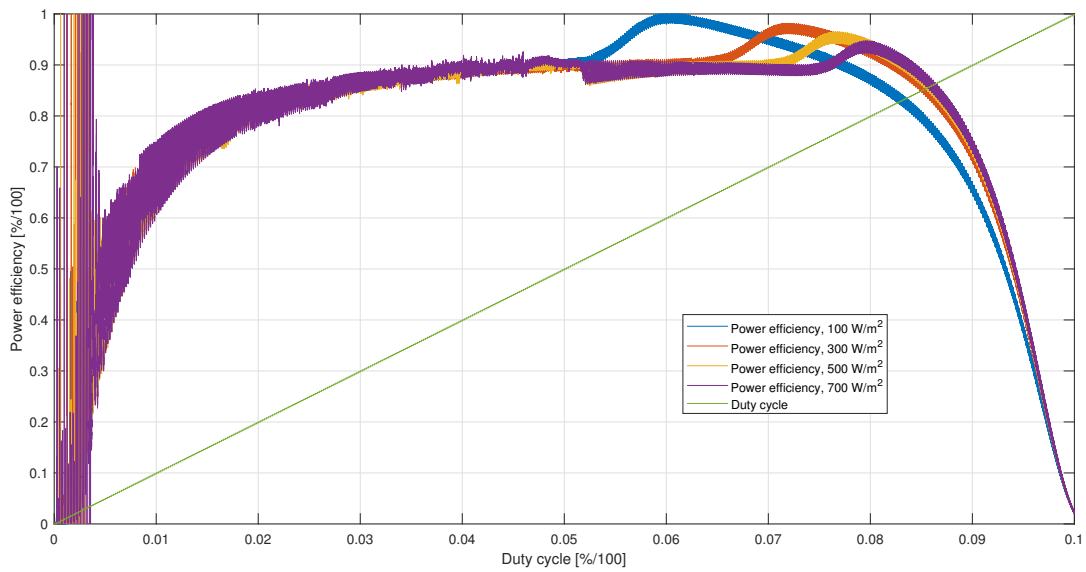


Figure 23: SEPIC power efficiency for a duty cycle sweep per solar irradiance for a 16-series PV cell configuration.

C Simulink Simulation Results with PV Cells, MPP and Lithium-ion Battery

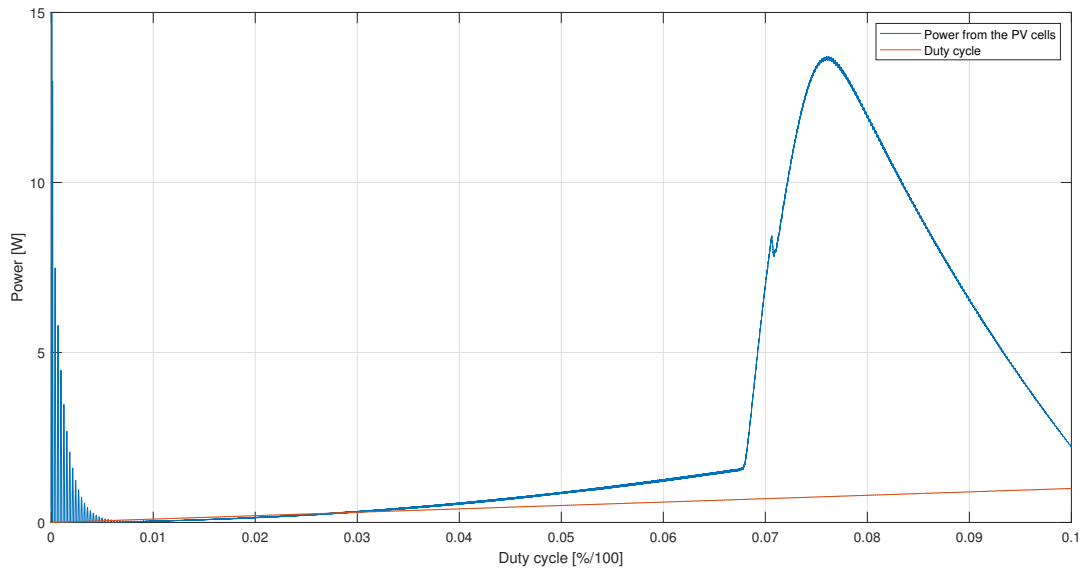


Figure 24: Power output of the PV-array block with corresponding duty cycle and a lithium-ion battery connected as load (conditions: 700 W/m^2 and 6-series configuration).

C.1 Lithium-ion battery in Simulink

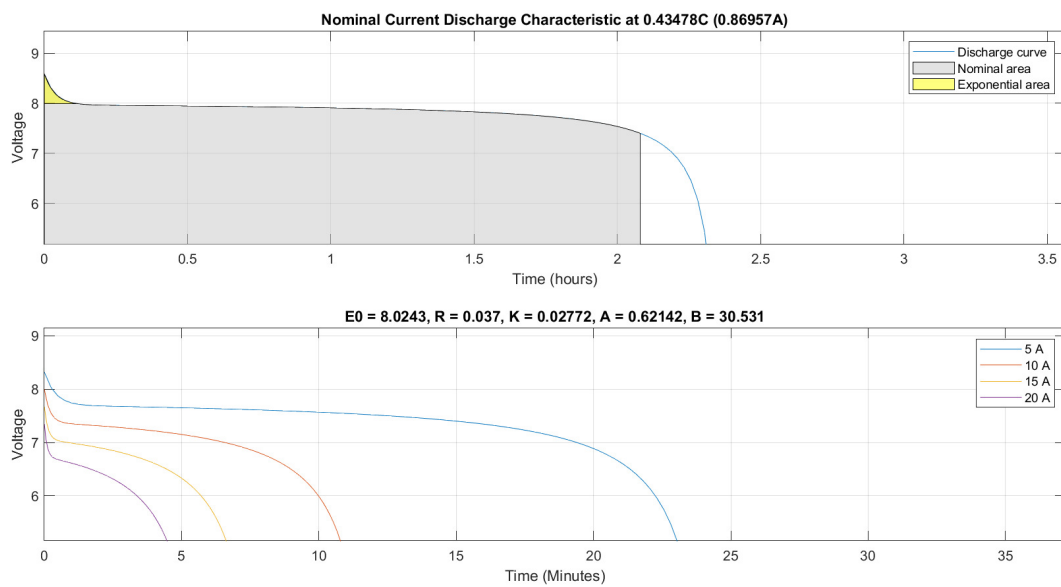


Figure 25: Lithium-ion characteristics of the Simulink model.

C.2 6-series configuration

6-series configuration Irradiance [W/m^2]	100	300	500	700
$V_{in,mpp}$ [V]	3.154	3.286	3.311	3.320
$P_{in,mpp}$ [W]	1.860	5.809	9.770	13.680
$V_{in,result}$ [V]	3.129	3.256	3.296	3.288
$P_{in,result}$ [W]	1.858	5.807	9.770	13.670
$I_{in} = I_{L_1}$ [A]	0.5938	1.783	2.964	4.158
Duty cycle MPP [%]	73.3	73.8	74.8	76.100
$P_{in,efficiency}$ [%]	99.89	99.97	100.00	99.93
$V_{Battery,avg}$ [V]	7.980	7.997	8.020	8.031
$V_{Battery,ripplepk-pk}$ [V]	0.020	0.058	0.100	0.140
$V_{Battery,ripple}$ [%]	0.25	0.73	1.25	1.74
SOC(0) [%]	50	50	50	50
SOC(t)-SOC(0) [%]	0.00028	0.00087	0.00137	0.0018
P_{out} [W]	1.609	5.009	7.911	10.408
I_{out} [A]	0.202	0.626	0.986	1.296
$P_{out,efficiency}$ [%]	86.59	86.26	80.97	76.14
Simulation time t [s]	0.1	0.1	0.1	0.1

Table 15: Simulink measurement of the SEPIC PV-application with lithium-ion battery of a 6-series configuration.

C.3 12-series configuration

12-series configuration Irradiance [W/m^2]	100	300	500	700
$V_{in,mpp}$ [V]	6.308	6.571	6.622	6.640
$P_{in,mpp}$ [W]	3.720	11.620	19.540	27.360
$V_{in,result}$ [V]	6.262	6.512	6.592	6.580
$P_{in,result}$ [W]	3.714	11.610	19.530	27.130
$I_{in} = I_{L_1}$ [A]	0.593	1.783	2.963	4.150
Duty cycle MPP [%]	57.6	57.8	58.6	59.7
$P_{in,efficiency}$ [%]	99.84	99.91	99.95	99.82
$V_{Battery,avg}$ [V]	7.990	8.032	8.065	8.088
$V_{Battery,ripplepk-pk}$ [V]	0.03	0.08	0.14	0.19
$V_{Battery,ripple}$ [%]	0.38	0.99	1.74	2.35
SOC(0) [%]	50	50	50	50
SOC(t)-SOC(0) [%]	0.00058	0.00178	0.00288	0.00385
P_{out} [W]	3.308	10.294	16.723	22.420
I_{out} [A]	0.414	1.128	2.074	2.772
$P_{out,efficiency}$ [%]	89.06	88.66	85.63	82.09
Simulation time t [s]	0.1	0.1	0.1	0.1

Table 16: Simulink measurement of the SEPIC PV-application with lithium-ion battery of a 12-series configuration.

C.4 16-series configuration

16-series configuration Irradiance [W/m^2]	100	300	500	700
$V_{in,mpp}$ [V]	8.411	8.762	8.829	8.854
$P_{in,mpp}$ [W]	4.961	15.490	26.050	36.480
$V_{in,result}$ [V]	8.365	8.697	8.750	8.789
$P_{in,result}$ [W]	4.954	15.470	26.010	36.440
$I_{in} = I_{L1}$ [A]	0.592	1.779	2.973	4.146
Duty cycle MPP [%]	50.4	50.5	51.4	52.3
$P_{in,efficiency}$ [%]	99.86	99.87	99.85	99.89
$V_{Battery,avg}$ [V]	7.993	8.045	8.102	8.129
$V_{Battery,ripplepk-pk}$ [V]	0.04	0.10	0.16	0.25
$V_{Battery,ripple}$ [%]	0.500	1.243	1.975	3.075
SOC(0) [%]	50	50	50	50
SOC(t)-SOC(0) [%]	0.00077	0.00238	0.00386	0.00521
P_{out} [W]	4.431	13.786	22.517	30.494
I_{out} [A]	0.554	1.714	2.779	3.751
$P_{out,efficiency}$ [%]	89.45	89.11	86.57	83.68
Simulation time t [s]	0.1	0.1	0.1	0.1

Table 17: Simulink measurement of the SEPIC PV-application with lithium-ion battery of a 16-series configuration.

C.5 Corresponding plots

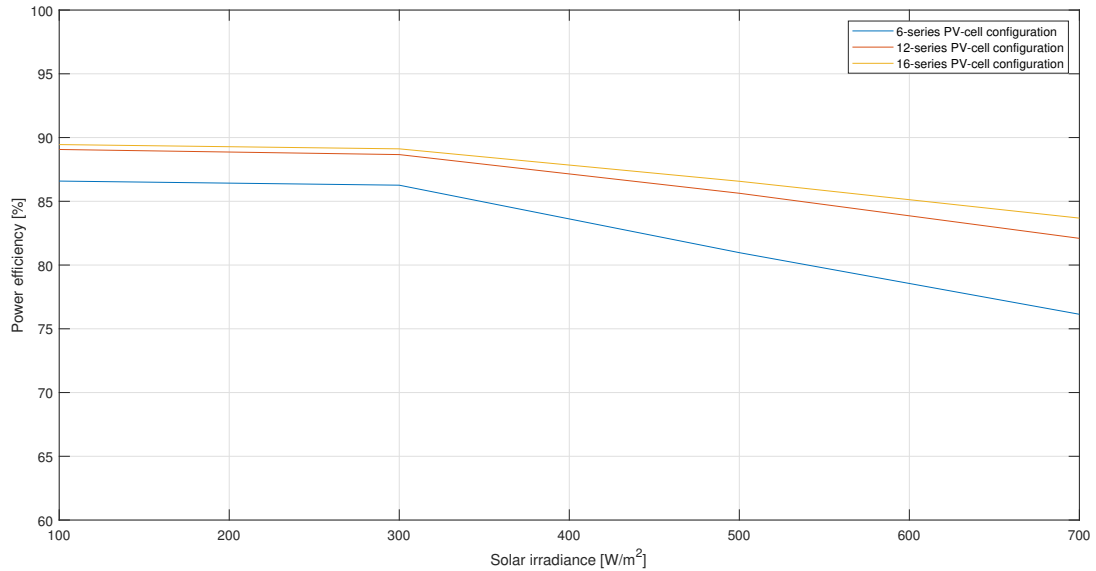


Figure 26: Power efficiency per solar irradiance for different PV-cell configurations under the circumstances of operating on the MPPT.

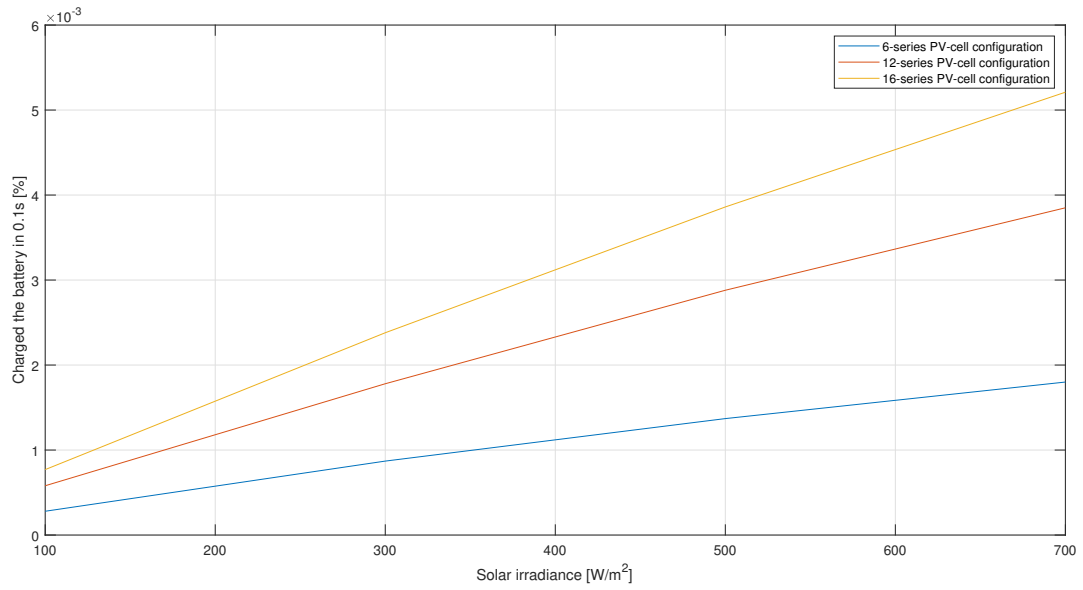


Figure 27: Charged percentage of the lithium-ion battery for charging 0.1s per solar irradiance for different PV-cell configurations under the circumstances of operating on the MPPT.

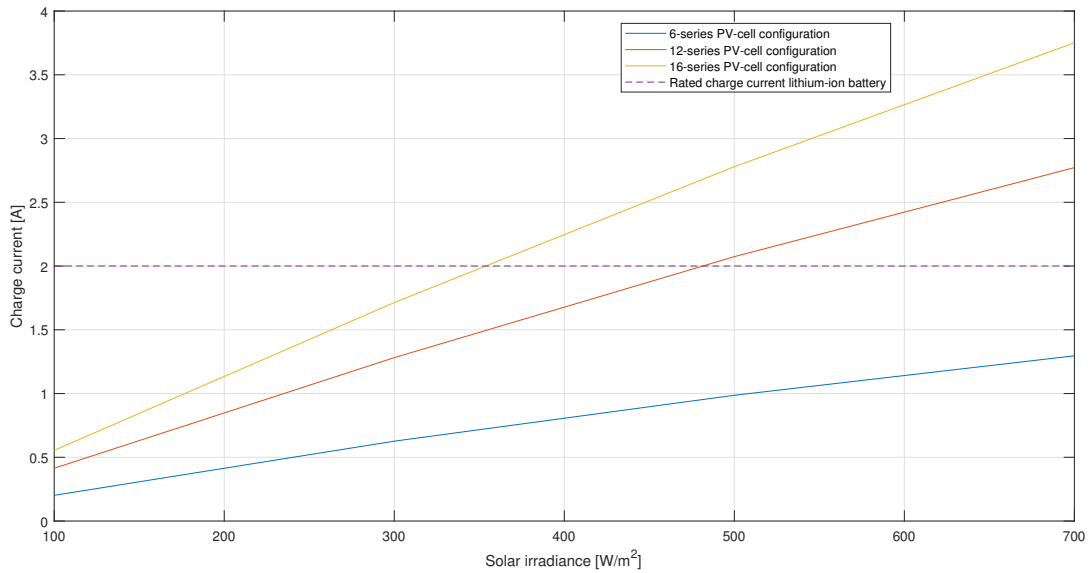


Figure 28: Battery charge current per solar irradiance for different PV-cell configurations under the circumstances of operating on the MPPT.

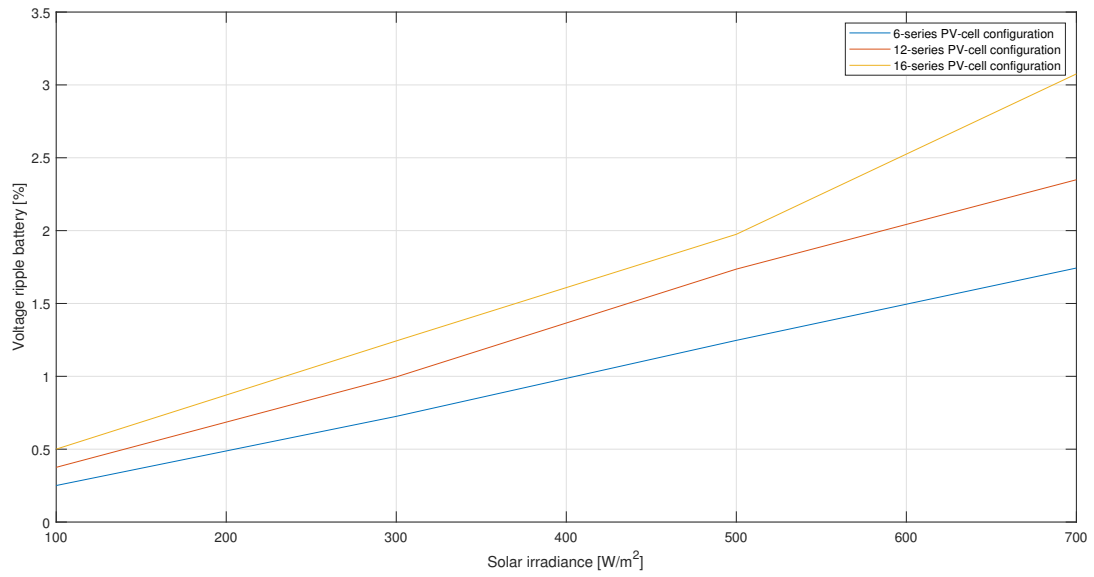


Figure 29: Battery voltage ripple percentage per solar irradiance for different PV-cell configurations under the circumstances of operating on the MPPT.

D Output voltage of first design SEPIC



Figure 30: Output voltage of first SEPIC (Figure 16). Input: 4V, 59% duty cycle.

E Power Efficiency Measurements for MOSFET Decision

E.1 SEPIC design 2, IRF530NS MOSFET [10]

$R_{load} = 50\Omega$				$R_{load} = 10\Omega$		
$V_{in}[V]$	$V_{out}[V]$	$I_{in}[A]$	$P_{efficiency}[\%]$	$V_{out}[V]$	$I_{in}[A]$	$P_{efficiency}[\%]$
1.2	6.32	0.88	75.6	3.58	2.35	45.4
1.8	6.97	0.645	83.7	4.89	2.18	60.9
2.4	7.23	0.50	87.1	5.66	1.90	70.3
3.0	7.35	0.41	87.8	6.17	1.65	76.9
3.6	7.42	0.35	87.4	6.48	1.45	80.4
4.08	7.64	0.32	89.4	6.65	1.31	82.7
4.2	7.97	0.33	91.7	6.77	1.28	85.3
4.8	9.2	0.39	90.4	6.91	1.14	87.3
5.4	10.4	0.44	91.0	7.04	1.03	89.1
6.0	10.7	0.42	90.9	7.10	0.94	89.4
6.6	10.7	0.37	93.8	7.18	0.87	89.8
7.2	11.4	0.4	90.3	7.23	0.80	90.8

Table 18: Practical measurements on the second SEPIC design (Figure 17) with the IRF530NS MOSFET [10], including power efficiency for 50 Ω and 10 Ω loads.

E.2 SEPIC design 2, CSD18536KCS MOSFET [18]

$R_{load} = 50\Omega$				$R_{load} = 10\Omega$		
$V_{in}[V]$	$V_{out}[V]$	$I_{in}[A]$	$P_{efficiency}[\%]$	$V_{out}[V]$	$I_{in}[A]$	$P_{efficiency}[\%]$
1.2	8.07	1.85	58.7	3.92	4.01	32.0
1.8	8.85	1.16	75.0	5.86	3.55	53.7
2.4	8.97	0.83	80.8	6.89	2.99	66.2
3.0	8.97	0.65	82.5	7.42	2.51	73.1
3.6	8.93	0.53	83.6	7.76	2.16	77.4
4.08	8.92	0.47	83.0	7.94	1.93	80.0
4.2	8.92	0.45	84.2	7.98	1.88	80.6
4.8	8.95	0.4	83.4	8.12	1.66	82.7
5.4	9.3	0.37	86.6	8.22	1.49	84.0
6.0	9.99	0.38	87.5	8.3	1.35	85.0
6.6	10.9	0.41	87.8	8.36	1.24	85.4
7.2	12	0.45	88.9	8.42	1.15	85.6

Table 19: Practical measurements on the second SEPIC design (Figure 17) with the CSD18536KCS MOSFET [18], including power efficiency for 50 Ω and 10 Ω loads.

E.3 SEPIC design 3, IRF530NS MOSFET [10]

$R_{load} = 50\Omega$			$R_{load} = 10\Omega$			
V_{in} [V]	V_{out} [V]	I_{in} [A]	$P_{efficiency}$ [%]	V_{out} [V]	I_{in} [A]	$P_{efficiency}$ [%]
1.2	5.8	0.78	71.9	2.68	1.78	33.6
1.8	6.73	0.61	82.5	4.07	1.82	50.6
2.4	7.13	0.49	86.5	5.02	1.69	62.1
3.0	7.3	0.41	86.7	5.65	1.52	70.0
3.6	7.43	0.35	87.6	6.08	1.36	75.5
4.08	7.81	0.34	87.9	6.31	1.25	78.1
4.2	8.14	0.35	90.1	6.53	1.24	81.9
4.8	9.36	0.41	89.0	6.72	1.12	84.0
5.4	10.4	0.45	89.0	6.88	1.02	85.9
6.0	10.4	0.41	87.9	6.99	0.93	87.6
6.6	10.7	0.39	89.0	7.07	0.86	88.1
7.2	11.8	0.43	89.9	7.12	0.80	88.0

Table 20: Practical measurements on the third SEPIC design (Figure 17) with the IRF530NS MOSFET [10], including power efficiency for 50Ω and 10Ω loads.

F Power Efficiency Measurements for Duty Cycle Sweep.

F.1 SEPIC design 3, IRF530NS MOSFET [10]

Power efficiency [%] Duty cycle [%] \ V_{in} [V]	1.2	2.4	3.6	4.8	6.0	7.2
20	68.8	79.67	83.63	84.63	85.57	86.12
25	73.89	80.74	84.32	86.92	87.28	87.24
30	77.14	83.22	84.93	86.80	88.13	89.17
35	77.29	84.60	86.77	87.62	88.06	88.87
40	77.66	84.42	87.02	88.20	89.10	89.63
45	79.75	85.66	86.94	88.07	88.58	89.47
50	80.69	86.22	87.78	89.45	90.21	90.69
55	80.78	85.56	87.12	89.37	89.99	90.10
60	82.2	86.09	87.95	89.32	90.70	90.30
65	82.51	86.31	87.78	89.37	90.05	90.70
70	82.21	85.55	86.96	89.14	89.23	89.63
75	82.10	85.18	86.22	88.04	87.66	88.50
80	79.70	81.86	82.43	84.31	83.92	83.4
85	72.72	73.36	74.60	75.27	73.31	-
90	55.62	52.71	43.36	-	-	-

Table 21: Power efficiency of duty cycle sweep per input voltage from a voltage source.

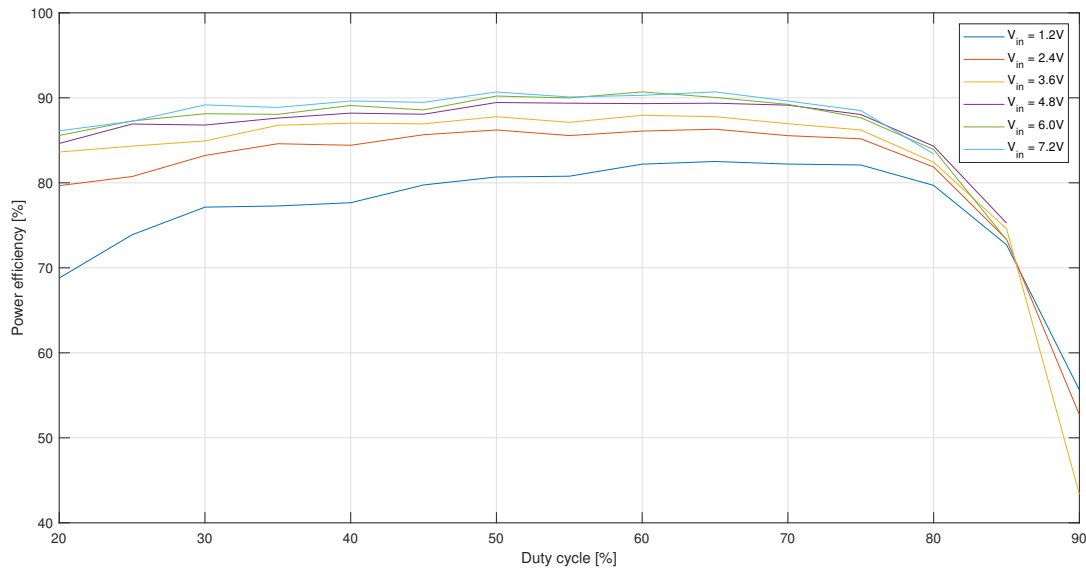


Figure 31: Power efficiency measurements per input voltage sweeping the duty cycle. Measurements are from Table 21.

G Inductor Trade-off

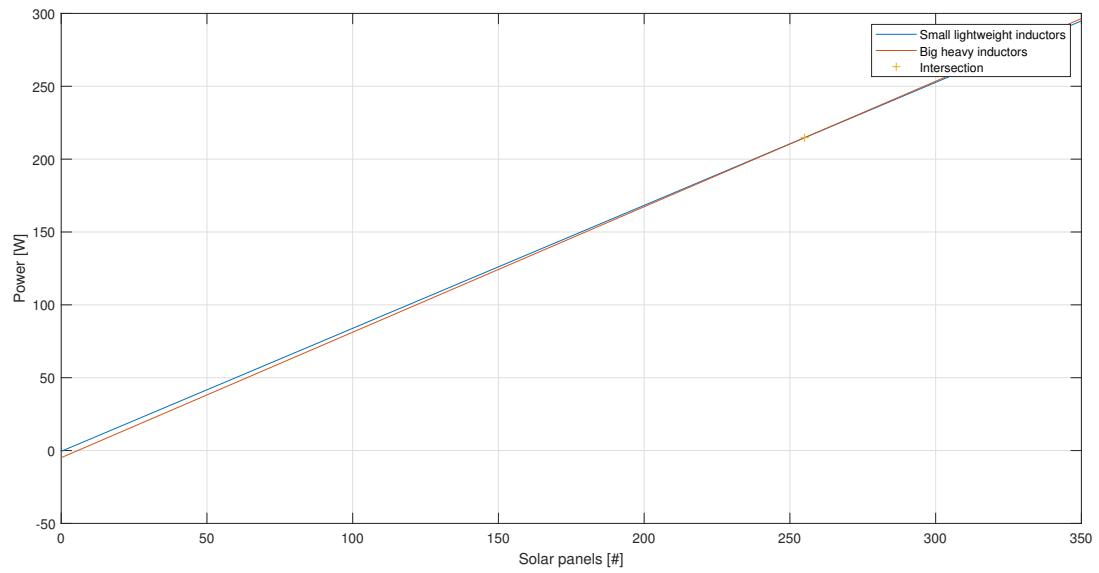


Figure 32: Amount of energy by amount of solar panels for design 2 and 3

H Practical Measurements



Figure 33: Solar box and PV-module for the practical measurements.



Figure 34: Solar irradiance meter used in the solar box of [Figure 33](#).

H.1 Resistive load 20Ω

Duty cycle [%]	V_{in} [V]	I_{in} [A]	V_{out} [V]	I_{out} [A]	P_{in} [W]	P_{out} [W]	$P_{efficiency}$ [%]
20.0	5.320	0.050	1.480	0.140	0.266	0.207	77.895
22.5	5.310	0.064	1.690	0.161	0.340	0.272	80.064
25.0	5.290	0.084	1.990	0.186	0.444	0.370	83.297
27.5	5.250	0.102	2.180	0.206	0.536	0.449	83.862
30.0	5.270	0.113	2.270	0.218	0.596	0.495	83.099
32.5	5.240	0.123	2.390	0.227	0.645	0.543	84.176
35.0	5.250	0.145	2.640	0.247	0.761	0.652	85.659
37.5	5.120	0.178	3.830	0.188	0.911	0.720	79.007
40.0	5.150	0.186	4.160	0.202	0.958	0.840	87.725
42.5	5.100	0.226	4.590	0.222	1.153	1.019	88.407
45.0	5.110	0.260	4.880	0.238	1.329	1.161	87.418
47.5	5.050	0.266	4.950	0.241	1.343	1.193	88.807
50.0	5.080	0.270	4.990	0.242	1.372	1.208	88.042
52.5	5.040	0.310	5.220	0.258	1.562	1.347	86.198
55.0	4.980	0.371	5.730	0.281	1.848	1.610	87.148
57.5	4.900	0.444	6.240	0.304	2.176	1.897	87.192
60.0	4.720	0.529	6.810	0.329	2.497	2.240	89.732
62.5	4.660	0.629	7.270	0.353	2.931	2.566	87.553
65.0	4.400	0.743	7.740	0.375	3.269	2.903	88.783
67.5	4.200	0.865	8.110	0.392	3.633	3.179	87.507
70.0	3.580	0.901	7.470	0.365	3.226	2.727	84.529
72.5	2.780	0.906	6.380	0.324	2.519	2.067	82.072
75.0	2.270	0.909	5.800	0.286	2.063	1.659	80.390
77.5	1.780	0.911	5.320	0.250	1.622	1.330	82.019
80.0	1.480	0.907	4.350	0.216	1.342	0.940	69.996
82.5	1.080	0.910	3.810	0.183	0.983	0.697	70.943
85.0	0.850	0.913	3.110	0.153	0.776	0.476	61.314
87.5	0.640	0.914	2.540	0.125	0.585	0.318	54.277
90.0	0.472	0.915	1.930	0.097	0.432	0.187	43.348

Table 22: Practical measurements of the SEPIC, conditions: 12-series PV-cell configuration, 20Ω resistive load and a solar irradiance of $280 W/m^2$.

Duty cycle [%]	V_{in} [V]	I_{in} [A]	V_{out} [V]	I_{out} [A]	P_{in} [W]	P_{out} [W]	$P_{efficiency}$ [%]
20.0	6.230	0.065	2.660	0.128	0.405	0.340	84.080
22.5	6.190	0.073	2.920	0.138	0.452	0.403	89.176
25.0	6.160	0.087	3.120	0.149	0.536	0.465	86.744
27.5	6.090	0.106	3.420	0.164	0.646	0.561	86.885
30.0	6.130	0.134	3.840	0.184	0.821	0.707	86.017
32.5	6.140	0.164	4.330	0.206	1.007	0.892	88.581
35.0	6.170	0.181	4.500	0.216	1.117	0.972	87.037
37.5	6.070	0.188	4.610	0.220	1.141	1.014	88.874
40.0	6.110	0.215	4.860	0.235	1.314	1.142	86.941
42.5	6.020	0.261	5.350	0.258	1.571	1.380	87.849
45.0	6.050	0.303	5.800	0.279	1.833	1.618	88.274
47.5	5.990	0.311	5.810	0.282	1.863	1.638	87.950
50.0	5.970	0.316	5.930	0.285	1.887	1.690	89.586
52.5	5.960	0.365	6.360	0.305	2.175	1.940	89.170
55.0	5.810	0.439	6.920	0.332	2.551	2.297	90.075
57.5	5.810	0.526	7.500	0.361	3.056	2.708	88.594
60.0	5.670	0.630	8.100	0.392	3.572	3.175	88.889
62.5	5.580	0.754	8.660	0.423	4.207	3.663	87.067
65.0	5.410	0.900	9.340	0.454	4.869	4.240	87.089
67.5	4.860	1.010	9.400	0.457	4.909	4.296	87.516
70.0	4.670	1.183	9.830	0.477	5.525	4.689	84.873
72.5	4.220	1.374	9.990	0.491	5.798	4.905	84.596
75.0	3.820	1.566	10.000	0.492	5.982	4.920	82.245
77.5	3.310	1.674	9.730	0.459	5.541	4.466	80.601
80.0	2.570	1.677	7.840	0.395	4.310	3.097	71.853
82.5	2.010	1.678	6.990	0.335	3.373	2.342	69.428
85.0	1.480	1.678	5.840	0.279	2.483	1.629	65.609
87.5	1.180	1.682	4.600	0.226	1.985	1.040	52.379
90.0	0.885	1.685	3.690	0.177	1.491	0.653	43.798

Table 23: Practical measurements of the SEPIC, conditions: 12-series PV-cell configuration, 20Ω resistive load and a solar irradiance of $430 W/m^2$.

Duty cycle [%]	V_{in} [V]	I_{in} [A]	V_{out} [V]	I_{out} [A]	P_{in} [W]	P_{out} [W]	$P_{efficiency}$ [%]
20.0	6.380	0.068	2.690	0.132	0.434	0.355	81.846
22.5	6.360	0.079	2.900	0.143	0.502	0.415	82.537
25.0	6.330	0.090	3.110	0.153	0.570	0.476	83.523
27.5	6.290	0.110	3.460	0.169	0.692	0.585	84.512
30.0	6.320	0.138	3.870	0.191	0.872	0.739	84.752
32.5	6.290	0.170	4.400	0.213	1.069	0.937	87.646
35.0	6.280	0.188	4.630	0.224	1.181	1.037	87.844
37.5	6.360	0.194	4.700	0.228	1.234	1.072	86.851
40.0	6.270	0.222	5.040	0.243	1.392	1.225	87.987
42.5	6.240	0.268	5.540	0.266	1.672	1.474	88.119
45.0	6.160	0.311	5.860	0.286	1.916	1.676	87.483
47.5	6.050	0.461	5.000	0.485	2.789	2.425	86.947
50.0	5.950	0.559	5.530	0.527	3.326	2.914	87.621
52.5	5.840	0.666	5.960	0.568	3.889	3.385	87.038
55.0	5.550	0.788	6.270	0.604	4.373	3.787	86.593
57.5	5.380	0.926	6.850	0.648	4.982	4.439	89.099
60.0	5.280	1.080	7.040	0.684	5.702	4.815	84.444
62.5	5.030	1.255	7.530	0.716	6.313	5.391	85.408
65.0	4.680	1.447	7.810	0.742	6.772	5.795	85.574
67.5	4.450	1.654	7.910	0.759	7.360	6.004	81.569
70.0	4.050	1.865	7.810	0.763	7.553	5.959	78.894
72.5	3.680	2.041	7.850	0.738	7.511	5.793	77.132
75.0	2.980	2.058	6.980	0.655	6.133	4.572	74.548
77.5	2.500	2.062	5.840	0.572	5.155	3.340	64.801
80.0	1.970	2.066	5.280	0.493	4.070	2.603	63.956
82.5	1.680	2.065	4.500	0.418	3.469	1.881	54.220
85.0	1.370	2.066	3.490	0.349	2.830	1.218	43.033
87.5	1.110	2.070	2.870	0.284	2.298	0.815	35.474
90.0	0.906	2.078	2.300	0.222	1.883	0.511	27.121

Table 24: Practical measurements of the SEPIC, conditions: 12-series PV-cell configuration, 20Ω resistive load and a solar irradiance of $535 W/m^2$.

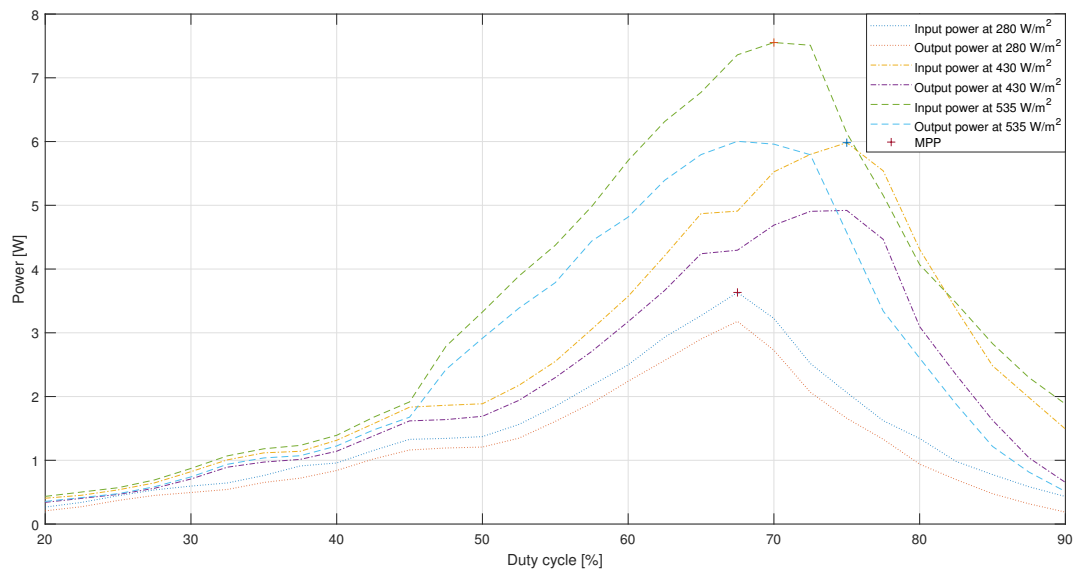


Figure 35: Input and output power of the SEPIC with 20 Ω resistive load for different solar-irradiances and a 12-series PV-cell configuration.

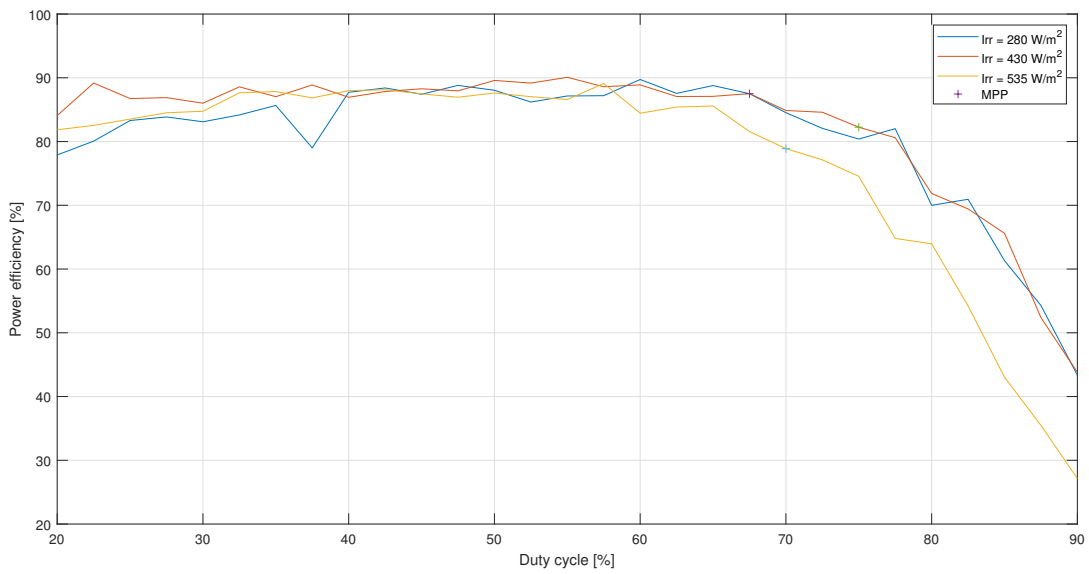


Figure 36: Power efficiency of the SEPIC with 20 Ω resistive load for different solar-irradiances and a 12-series PV-cell configuration.

H.2 Lithium-ion battery as load

Duty cycle [%]	V_{in} [V]	I_{in} [A]	V_{out} [V]	I_{out} [A]	P_{in} [W]	P_{out} [W]	$P_{efficiency}$ [%]
20.0	5.640	0.057	7.810	0.035	0.321	0.273	85.029
22.5	5.640	0.072	7.820	0.045	0.406	0.352	86.658
25.0	5.640	0.077	7.830	0.048	0.434	0.376	86.543
27.5	5.550	0.110	7.840	0.069	0.611	0.541	88.609
30.0	5.550	0.115	7.840	0.072	0.638	0.564	88.442
32.5	5.520	0.134	7.840	0.083	0.740	0.651	87.973
35.0	5.420	0.166	7.850	0.103	0.900	0.809	89.867
37.5	5.510	0.167	7.840	0.104	0.920	0.815	88.610
40.0	5.350	0.218	7.860	0.133	1.166	1.045	89.632
42.5	5.360	0.228	7.860	0.139	1.222	1.093	89.400
45.0	5.450	0.231	7.860	0.140	1.259	1.100	87.406
47.5	5.320	0.299	7.870	0.179	1.591	1.409	88.561
50.0	5.340	0.301	7.880	0.180	1.607	1.418	88.245
52.5	5.330	0.304	7.880	0.182	1.620	1.434	88.511
55.0	5.190	0.389	7.900	0.226	2.019	1.785	88.434
57.5	5.220	0.390	7.900	0.226	2.036	1.785	87.700
60.0	5.220	0.387	7.890	0.225	2.020	1.775	87.878
62.5	4.990	0.523	7.920	0.290	2.610	2.297	88.008
65.0	4.620	0.765	7.940	0.386	3.534	3.065	86.717
67.5	4.230	0.934	7.980	0.424	3.951	3.384	85.641
70.0	3.780	0.950	7.960	0.383	3.591	3.049	84.898
72.5	3.370	0.952	7.940	0.338	3.208	2.684	83.651
75.0	2.950	0.950	7.940	0.297	2.803	2.358	84.146
77.5	2.610	0.951	7.920	0.258	2.482	2.043	82.324
80.0	2.260	0.956	7.900	0.223	2.161	1.762	81.539
82.5	1.950	0.955	7.890	0.188	1.862	1.483	79.652
85.0	1.660	0.957	7.880	0.156	1.589	1.229	77.380
87.5	1.360	0.959	7.880	0.125	1.304	0.985	75.523
90.0	1.110	0.958	7.870	0.096	1.063	0.756	71.049

Table 25: Practical measurements of the SEPIC, conditions: 12-series PV-cell configuration, Lithium-ion battery as load and a solar irradiance of 280 W/m^2 .

Duty cycle [%]	V_{in} [V]	I_{in} [A]	V_{out} [V]	I_{out} [A]	P_{in} [W]	P_{out} [W]	$P_{efficiency}$ [%]
20.0	6.310	0.068	7.760	0.048	0.429	0.372	86.809
22.5	6.350	0.077	7.760	0.055	0.489	0.427	87.289
25.0	6.260	0.091	7.770	0.064	0.570	0.497	87.294
27.5	6.230	0.119	7.780	0.084	0.741	0.654	88.150
30.0	6.220	0.123	7.780	0.087	0.765	0.677	88.471
32.5	6.160	0.168	7.790	0.119	1.035	0.927	89.577
35.0	6.170	0.173	7.790	0.122	1.067	0.950	89.036
37.5	6.170	0.198	7.800	0.138	1.222	1.076	88.110
40.0	6.080	0.236	7.810	0.165	1.435	1.289	89.809
42.5	6.100	0.237	7.800	0.166	1.446	1.295	89.562
45.0	6.090	0.307	7.830	0.211	1.870	1.652	88.367
47.5	5.990	0.311	7.820	0.215	1.863	1.681	90.252
50.0	6.050	0.318	7.820	0.219	1.924	1.713	89.016
52.5	5.960	0.401	7.850	0.270	2.390	2.120	88.683
55.0	5.990	0.400	7.840	0.274	2.396	2.148	89.656
57.5	5.970	0.431	7.850	0.292	2.573	2.292	89.084
60.0	5.650	0.790	7.930	0.494	4.464	3.917	87.766
62.5	5.270	1.127	8.000	0.640	5.939	5.120	86.206
65.0	4.860	1.408	8.010	0.720	6.843	5.767	84.280
67.5	4.480	1.595	8.010	0.730	7.146	5.847	81.831
70.0	4.060	1.602	7.970	0.656	6.504	5.228	80.385
72.5	3.620	1.717	7.970	0.619	6.216	4.933	79.373
75.0	3.270	1.615	7.960	0.512	5.281	4.076	77.173
77.5	2.840	1.740	7.930	0.479	4.942	3.798	76.867
80.0	2.570	1.740	7.930	0.410	4.472	3.251	72.707
82.5	2.200	1.743	7.910	0.346	3.835	2.737	71.373
85.0	1.950	1.747	7.880	0.287	3.407	2.262	66.387
87.5	1.630	1.740	7.860	0.230	2.836	1.808	63.740
90.0	1.350	1.746	7.850	0.177	2.357	1.389	58.947

Table 26: Practical measurements of the SEPIC, conditions: 12-series PV-cell configuration, Lithium-ion battery as load and a solar irradiance of 430 W/m^2 .

Duty cycle [%]	V_{in} [V]	I_{in} [A]	V_{out} [V]	I_{out} [A]	P_{in} [W]	P_{out} [W]	$P_{efficiency}$ [%]
20.0	6.420	0.069	7.700	0.050	0.443	0.385	86.911
22.5	6.450	0.078	7.700	0.056	0.503	0.431	85.709
25.0	6.380	0.092	7.690	0.066	0.587	0.508	86.469
27.5	6.460	0.120	7.710	0.088	0.775	0.678	87.523
30.0	6.490	0.126	7.700	0.092	0.818	0.708	86.629
32.5	6.480	0.173	7.720	0.126	1.121	0.973	86.769
35.0	6.490	0.176	7.720	0.129	1.142	0.996	87.187
37.5	6.420	0.226	7.740	0.165	1.451	1.277	88.020
40.0	6.430	0.240	7.730	0.175	1.543	1.353	87.659
42.5	6.440	0.246	7.750	0.181	1.584	1.403	88.544
45.0	6.420	0.315	7.770	0.229	2.022	1.779	87.985
47.5	6.400	0.315	7.770	0.229	2.016	1.779	88.260
50.0	6.380	0.387	7.790	0.278	2.469	2.166	87.710
52.5	6.340	0.406	7.700	0.290	2.574	2.233	86.751
55.0	6.360	0.404	7.780	0.289	2.569	2.248	87.506
57.5	6.180	0.605	7.820	0.419	3.739	3.277	87.635
60.0	5.780	0.986	7.920	0.634	5.699	5.021	88.107
62.5	5.430	1.281	7.920	0.788	6.956	6.241	89.723
65.0	5.010	1.647	7.920	0.846	8.251	6.700	81.202
67.5	4.530	1.666	7.920	0.765	7.547	6.059	80.281
70.0	4.150	1.843	7.930	0.754	7.648	5.979	78.176
72.5	3.740	1.909	7.910	0.689	7.140	5.450	76.334
75.0	3.330	1.910	7.880	0.605	6.360	4.767	74.956
77.5	2.960	1.915	7.910	0.525	5.668	4.153	73.261
80.0	2.640	1.912	7.850	0.451	5.048	3.540	70.138
82.5	2.310	1.917	7.820	0.381	4.428	2.979	67.282
85.0	1.990	1.919	7.850	0.317	3.819	2.488	65.163
87.5	1.720	1.918	7.810	0.254	3.299	1.984	60.132
90.0	1.460	1.922	7.800	0.196	2.806	1.529	54.481

Table 27: Practical measurements of the SEPIC, conditions: 12-series PV-cell configuration, Lithium-ion battery as load and a solar irradiance of 535 W/m^2 .

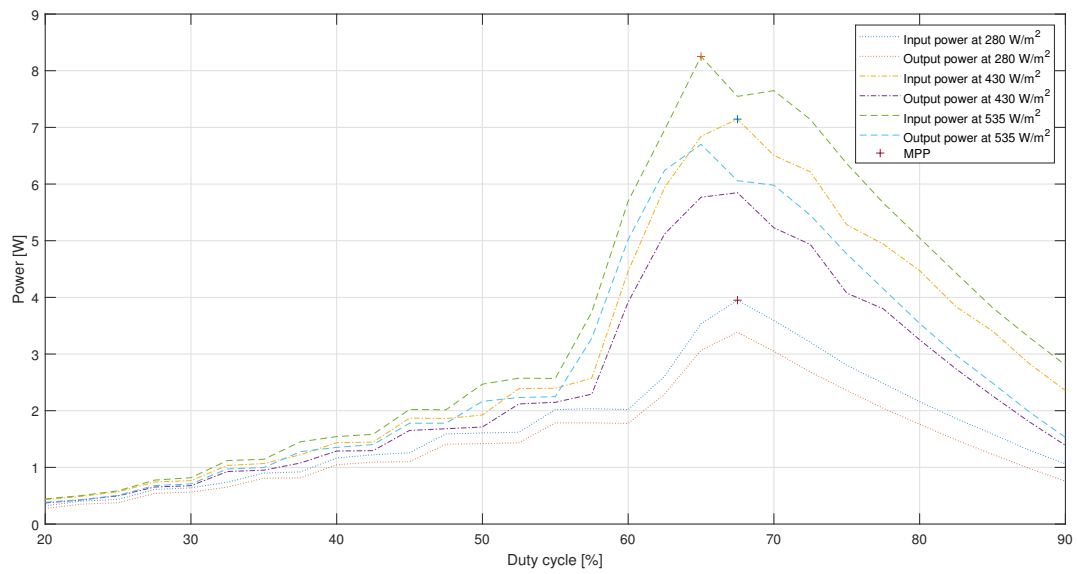


Figure 37: Input and output power of the SEPIC with Lithium-ion battery as load for different solar-irradiance and a 12-series PV-cell configuration.

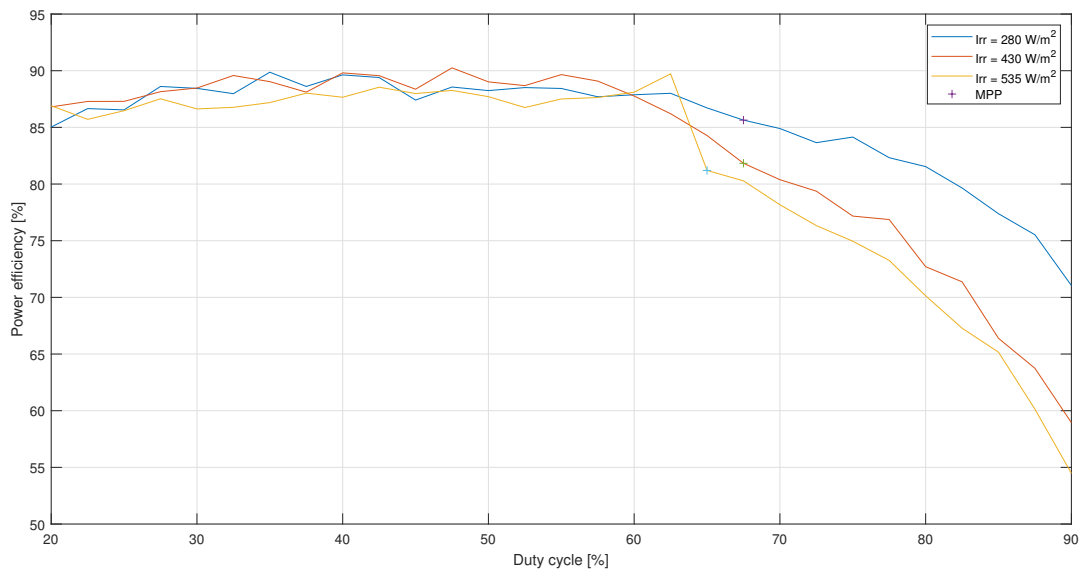


Figure 38: Power efficiency of the SEPIC with Lithium-ion battery as load for different solar-irradiance and a 12-series PV-cell configuration.

Bibliography

Asia's first fully solar-powered quadcopter (n.d.). <https://www.eng.nus.edu.sg/news/asias-first-fully-solar-powered-quadcopter/>. Accessed: 2019-06-12.